ACTIVE AND PASSIVE THERMOGRAPHY FOR THE DETECTION OF DEFECTS IN GREEN-STATE POWDERMETALLIC COMPACTS

by

Souheil Benzerrouk

A Dissertation
Submitted to the Faculty
of the
WORCESTER POLYTECHNIC INSTITUTE
in partial fulfillment of the requirements for the
Degree of Doctor of Philosophy
in
Electrical and Computer Engineering

August 2011

APPROVED:

Prof. Reinhold Ludwig, Research Advisor, ______________________
Electrical and Computer Engineering Department

Prof. Diran Apelian, Committee Member, ______________________
Mechanical Engineering Department

Prof. Sergey Makarov, Committee Member, ______________________
Electrical and Computer Engineering Department

Prof. Fred J. Loof, Committee member and Head of Department, ______________________
Electrical and Computer Engineering Department

Abstract

Despite its maturity, the powder metallurgy (PM) fabrication process continues to rely heavily on indirect methods to determine and predict the quality of its compacts early in the manufacturing line. Currently, the most comprehensive testing is performed on sintered parts, resulting in higher cost and increased waste.

This dissertation addresses the need of early inspection by developing a novel approach whereby PM compacts are tested in the green-state without intrusion and with minimal cost per compact tested. The method is based on an infrared detection scheme with two fundamental embodiments. For high resolution applications, or offline testing, an active thermography approach is adopted; electric energy is deposited into the compact in a contact-less fashion to evaluate all parts for cracks, inclusions, or delaminations. As an alternative, for lower resolution high-yield applications, a system based on a passive thermography approach is developed. This system relies on residual heating emanating from the process. Thermal data is then collected and analyzed in an effort to yield part integrity and process stability information.

In this dissertation we will discuss our design approach, theoretical modeling aspects, and a proof-of-concept instrument with associated data processing software. We will first describe the underlying physical principles, followed by predictions from the modeling formulation, including a solution of the heat equation. As part of our experimental data processing, we will present results that are collected both in a laboratory setting and in an industrial manufacturing line. The integrity of the compacts is carried out with the aid of a specialized software package.

Acknowledgement

I cannot express the gratitude I have to my dissertation advisor, Prof. Reinhold Ludwig. Without his guidance, patience and encouragements I would not have been able to complete this work. It has been a privilege to work with Prof. Ludwig and it has been an honor to be his friend. His commitment, enthusiasm and talent have certainly made a lasting impression on me.

I would like to express my gratitude to Prof. Diran Apelian for providing valuable insights during the course of this work and more importantly for being a mentor throughout my graduate career.

Very special thanks to Prof. Sergey Makarov for consenting to be part of my dissertation committee and for his help with the development of the electrostatic solutions.

I would also like to thank Prof. Fred Looft for consenting to be part of my dissertation committee and for providing valuable suggestions and for making the ECE department at WPI a second home to its students, staff and faculty.

Additional thanks go to Richard Scott (Nichols Portland), Hannes Traxler (PLANSEE Aktiengesellschaft), and Chaman Lall (Metal Power Products) for providing the needed PM samples to complete this research and for providing the facilities for the on-line testing.

Lastly, I extend my utmost gratitude to my wife Nadjet for her unlimited kindness and endless support.

Dedications

This humble work is dedicated to:

My wonderful parents, my father Mohamed who inspires me to be the best and my mother Hassiba with her kindness, generosity and true love. Their struggles are the source of pride and strength for their children and their patience and character are our model .

My sisters Abla and Ismahane who supported me with unlimited kindness and warmth.

My brothers M'hamed and Youcef who grew to become my best friends.

My extended family whose bond gave me the strength and desire to succeed. Especially, my brother-in-law Djamel Yousfi, my niece Hajar, my nephew Yunus and of course my in-laws Fatima and Mohamed Chibane.

The friends I am blessed with, especially, M'hamed Bouziane and his family, Amine Laredj and his family, and many others with whom I shared memorable moments.

Last, my wife Nadjet who makes every day a better one and my son Tarek who fills my life with hope.

Souheil Benzerrouk

Contents

List of Figures

List of Tables

Chapter 1

Problem Statement

1.1 Goals and Objectives

To gain a competitive edge and meet today's market requirements metal parts manufacturers are constantly investigating and applying advanced technologies, new processes and new materials. Among these processes is powder metallurgy (P/M) where high quality complex metal parts are manufactured with high volumes and low cost. This fabrication method proved to be a viable alternative to other metal working techniques such as forging and casting partly due to its versatility and flexibility.

Making metal parts through compacting powders allows manufacturers to choose the constituents hence resulting in the development of new alloys and the achievement of great mechanical properties such as; strength, toughness or ductility.

This efficient process brought along with its benefits new challenges due largely to the unique attributes of P/M. These challenges include porosity, the pore structure and the possibility of introducing undesired elements (particles) into the powder resulting in major degradation in the quality of the final product. Furthermore, the unique fabrication steps require finer control of process parameters. A careful review of all available non-destructive testing (NDT) techniques show that there is no viable method capable of evaluating parts early in the manufacturing process. Early testing brings cost savings and provides a better product overall. For powedermetallic compacts, the first stage is compaction which results in fragile parts both structurally as parts can easily break and chemically where any element such as gels for ultrasonic testing can cause the part to oxidize. Moreover, the porous nature of the compacts limit the usable NDT techniques to the methods where energy is transmitted through the part without major attenuation. For example, ultrasonic testing as presented in the Chapter 2 is unusable to the limited penetration of the sound waves. In addition to testing parts early in the process, no method exists that is capable of characterizing one-hundred percent of the parts without significantly reducing the throughput.

Past research resulted in high fidelity electrostatic method that was capable of detecting minute (as small as $20\mu m$ in length) surface and sub-surface defects in green-state compacts. This method uses a custom array sensor to inject current into the part and record the resulting voltage. The recorded voltage profile includes signatures from cracks or inclusions. Although this method detects defect in a reliable fashion it is slow as the part has to be stopped and a physical contact has to be initiated before any measurement. Moreover, this technique requires a special sensor for every part type; an undesirable artifact for the P/M industry.

In extending this approach it was reasoned that larger currents in the parts under test result in a Joule heating in the compact. Similar to the electrostatic method a void or an inclusion has a significantly different electric and thermal conductivities when compared to the bulk of the material. This difference in the conductivities causes a non-uniform temperature increase that can easily be recorded through an infrared (IR) camera. To avoid contacting the part which can cause damage due to the fragile and brittle nature of green-state compacts, current is injected into the part remotely using electromagnetic coupling (induction heating). this last approach is fully contact-less. Through modeling and experimentation the idea of imaging the infrared radiation to infer part integrity was applied passively, where no-external heat source is applied and temperature rise is a result of frictional forces present during compaction. Therefore, the dynamic thermal imaging of parts as they exist in the compaction press has the potential to test all parts on-line with no disruption to the manufacturing cycle.

The goal of this research project is to develop a non-destructive method that allows the detection of surface and subsurface defects in green-state P/M compacts. The idea is to use active and passive thermography to infer the integrity of the compacts. Since the method is required to provide one-hundred percent assessment, automatic image processing and evaluation techniques are applied and a custom software is developed.

Two major applications are considered; first, a simple go/no-go approach that can be deployed in manufacturing. Here two methods are envisioned; active and passive thermography where the latter relies on residual heat in the compact and natural convection as the cooling mechanism. Active thermography utilizes gated alternative current (AC) to cause a step change in the thermal profile over the surface of the part. The second application of this method is engineering evaluation where the requirement is to provide comprehensive and complete raw and processed thermal data. Here direct current (DC) or AC is used to generate heating in a controlled manner. Dynamic and high resolution thermal imaging provides detailed feedback on part part quality.

1.2 Approach

After reviewing the literature, an approach was devised whereby the necessary theoretical modeling was developed. The study focuses on the forward solution which includes the study of the energy transfer mechanisms between the electrical and thermal models. This study extends to include defect/material interactions. This is encoded as:

- Current flow and potential differences in the part (electrostatics).
- Electromagnetic current deposition.
- Heat transfer.
- IR radiation and detection which includes image processing.

The analytical foundation is used to calibrate the subsequent numerical model which in turn is used to evaluate the detection limits and to establish hardware requirements. The complexity of the thermo-electric phenomena coupled with the shape and the inhomogeneities inherent in P/M compacts demand a numerical model to study thermal responses from parts subjected to electric current. The first phase of the investigation focuses on the steady state approach followed by a more elaborate transient analysis. Furthermore, the study considers the expected energy deposition schemes; namely, conduction and induction. It is expected that this step results in detailed performance prediction where the minimum detectable defect and camera requirements are known. Finally, experimental testing is performed for almost all system embodiments to affirm the expected success of the methodology. The generic test approaches and the four embodiments of our test systems are summarized in Figure 1.1. It also includes the specific parameters for each procedure.

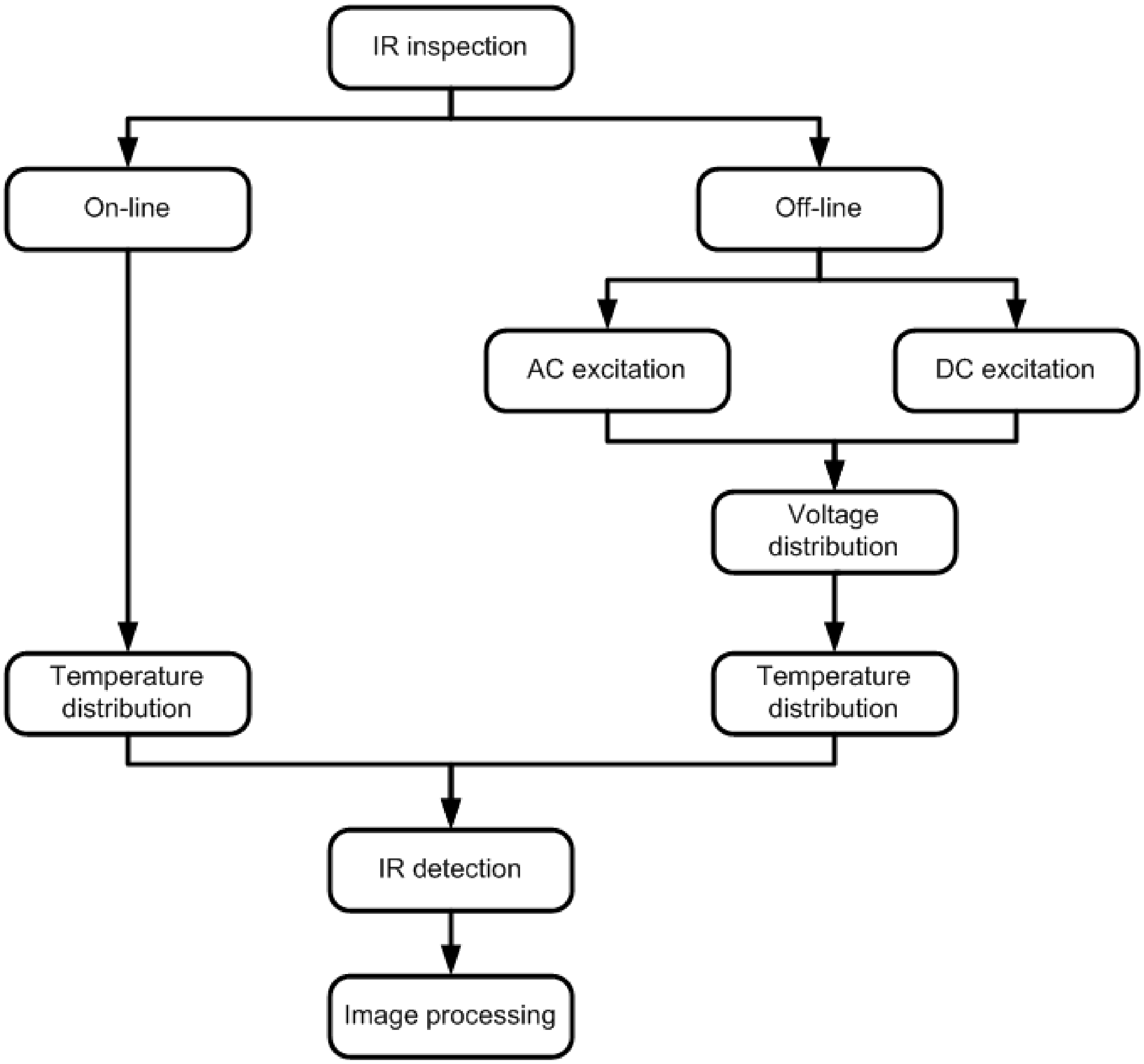

Figure 1.1: Block diagram of overall testing approach.

On-line testing involves parts pre-heated by compaction and only heat transfer parameters such as the thermal diffusivity and the convection heat transfer coefficient govern the thermal behavior of the part. Off-line testing includes external heat sources. First, a DC source is applied which causes a voltage distribution throughout the volume due the limited conductivity. The voltage distribution in turn cause a power density in the part which is lost as heat. This heat is represented in the temperature distribution on the surface of the part which is imaged using the camera. Similarly, for the AC source, addition parameters are included. Specifically, electromagnetic coupling where the conductivity and frequency play a role on the depth of penetration of the current into the part. Finally, all systems share the detection elements which include IR detection and signal processing.

1.3 Organization

This first chapter defines the problem statement, sets the goals of the project and itemizes the steps of the approach taken. It also describes our system with its multiple embodiments and applications.

Chapter 2 introduces the basic principles of powder metallurgy and the major steps in the P/M manufacturing process. The chapter describes the quality challenges within the industry and lists the candidate NDE techniques to address them with a comparative analysis.

Chapter 3 focuses on infrared imaging, starting with a discussion on radiation parameters, detector technology and image construction.

Chapter 4 establishes the theoretical foundation of the system including all the energy transfer mechanisms and all parameters such as: current flow, voltage distribution, temperature rise, and defect characteristics. Substantial derivation is shown and explained starting with Laplace's equation, then the heat equation and the Green function solution for defective parts.

Chapter 5 contains a discussion on the fundamentals of FEM modeling. This is used to construct a model that assimilates electrostatics and heat transfer and another where an electromagnetic model feeds a heat transfer simulation to predict the temperature rise and distribution over the surface to be inspected.

In chapter 6 experimental results are shown with a focus on image processing. Parts are evaluated off-line and under DC excitation initially, then by an inductive energy coupling. Later, results from on-line testing where parts are inspected at the exit of the press system in a P/M manufacturing setting. Chapter 6 dedicates a section to the discussion on the software development and the preliminary validation testing at a manufacturing site.

Last, in chapter 7 a conclusion is formulated to review the problem statement and the success criteria then list the accomplishments and suggestions of future work in an effort to extend the scope of the project and the possibility of new applications of the technology.

Chapter 2

The Powder Metallurgy Process

2.1 Introduction

Powder metallurgy is a manufacturing approach where parts are fabricated through the compaction of mixtures of metal powders, lubricants and binders into the desired shape with near net-shape precision. After compaction, parts are sintered in a furnace to give the compact its structural strength. This method has revolutionized the metal forming industry and opened new markets as new alloys are now possible and complex shapes such as the compact depicted in Figure 2.1 are easily manufactured at high rates, low cost, tight tolerances, high material usage (efficiently) and in a green and environmentally friendly fashion.

Figure 2.1: Various P/M parts: complex multi-level gear and uniform density cylinders.

As a process powder metallurgy results in complexly shaped parts that can meet tight tolerances with minimal to no post processing such as machining, grinding or milling. Hence, it can be classified as one of the most versatile metal working techniques. Furthermore, there is no melting of metals in this process which usually requires high energy, can be extremely dangerous during handling, and can generate a large amount of wasted material. Also, the P/M process provides for rapid prototyping with minimal set-up cost. This benefit is among the many attributes that appeals to major industries such as the automotive sector where parts are manufactured at high rate and new models which may require new parts are introduced frequently.

The P/M manufacturing scheme is fundamentally different from competing methods such as forging or casting. The diagram illustrated in Figure 2.2 represents a typical P/M manufacturing line with all possible post-processing steps. It is clear that in addition to the fact that near-net shape parts rarely require off-line operations and if required such steps are simple and fast.

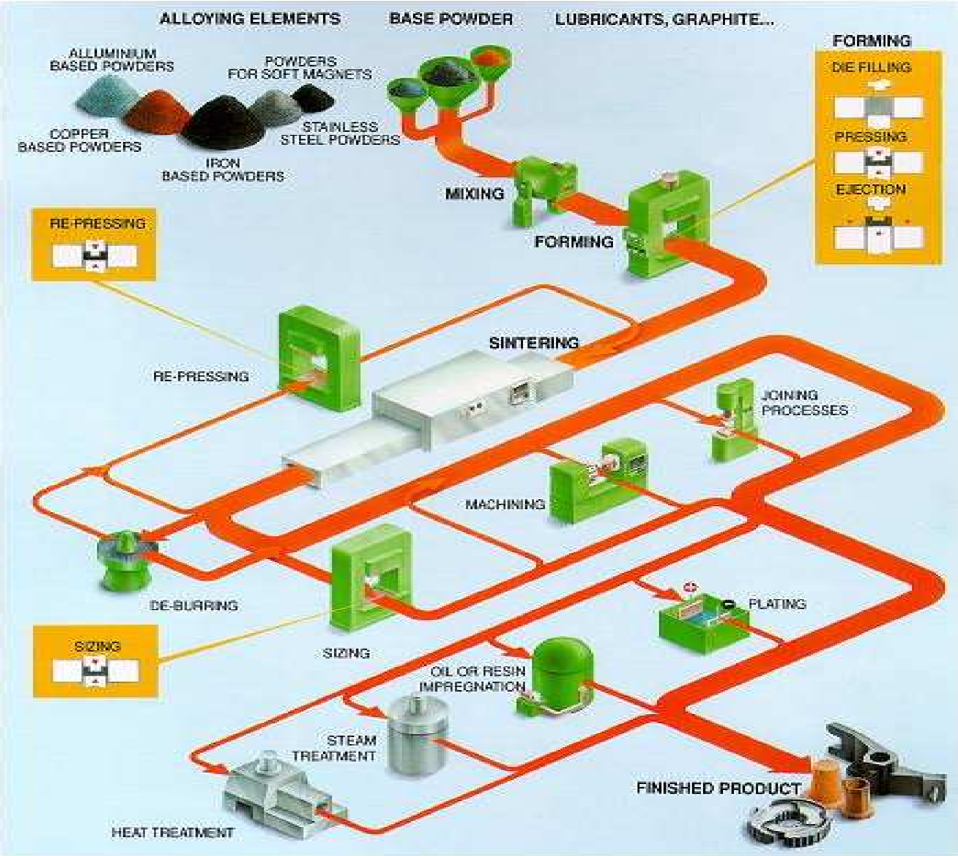

Figure 2.2: Generic manufacturing steps in the production of P/M samples (courtesy of GKN Sinter Metals).

The fabrication of a powder-metallic compact such as the gear shown in Figure 2.3 typically involves three fundamental areas: powder production, part fabrication, and the development of part properties [1]. The work flow starts with the fabrication of powders which are then classified based on material, size, shape and production technique. Subsequently, the basic steps of compaction and sintering take place to make the semi-finished product which will undergo additional secondary operations such as heat treating or plating to meet mechanical and material requirements [2].

The following sections describe in detail these basic steps in the powder metallurgy process.

Powders

The basic constituent in a powder metallic compact is the powder. Particles of various materials are pressed together to form the part, hence, powder characteristics determine the performance of the final product. Powder characteristics include:

- Material
- Shape
- Size distribution
- Surface area
- Microstructure

Furthermore, powder fabrication method is equally important in the prediction of the pressed compact. Figure 2.3 depicts a typical iron particle where one can easily observe the high degree of surface irregularity that exists in the size and shape. Therefore, it becomes very important to characterize powders with a size distribution rather than the size and with shape variations[1].

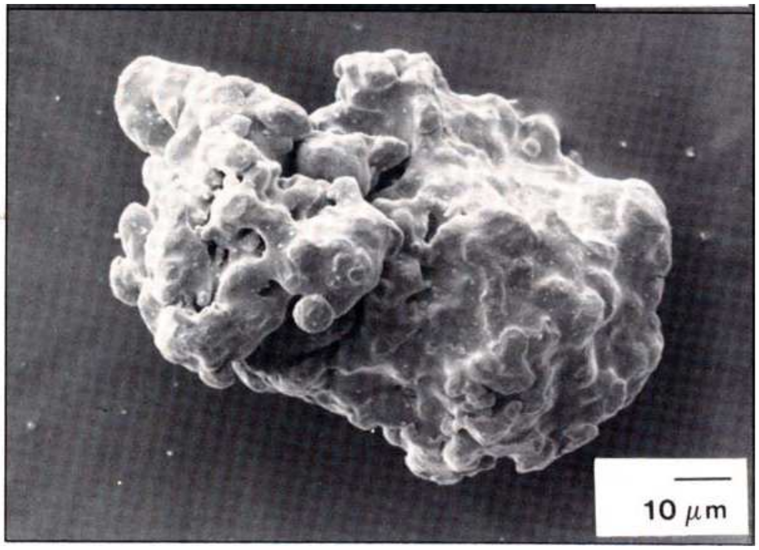

Figure 2.3: Typical Shape of an iron particle [1]

Knowledge of the size distribution allows for a better process control to achieve parts of the highest quality in an efficient manner. For example, fine particles do not flow easily and are hard to press as they require higher pressures while coarse powders are easily compacted but sinter poorly as they result in a high degree of porosity [3]. Therefore, fine powders are mixed with coarse powders to provide for better quality.

Similarly, the shape of the particle is an important parameter because it influences the total surface area and hence the surface energy released during packing. Moreover, the interparticle friction and packing factor are both related to the size and shape of the particle. Therefore, to classify powders of irregular shapes such as the particle shown in Figure 2.4-c an equivalent spherical diameter is estimated from the projected area [1]. Such that

$$A = \frac{\pi D_A^2}{4} \tag{2.1}$$

where A is the projected area and D_A is the equivalent spherical diameter. Therefore

$$D_A = \sqrt{\frac{4A}{\pi}} \tag{2.2}$$

For example, for the typical values of $H = 1\mu m$, $W = 0.72\mu m$, and $M = 1.03\mu m$ will result in $D_A = 0.76\mu m$. Figure 2.4 shows the most common particle shapes.

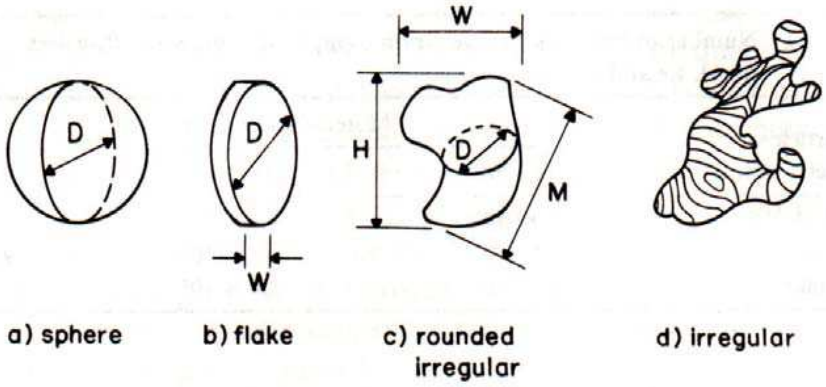

Figure 2.4: Common particle shapes [1]

To achieve a specific particle size and shape distributions innovative atomization techniques were devised. These powder fabrication techniques are subdivided into four categories: 1) mechanical such as machining and milling, 2) chemical in the form of gas or thermal decomposition, 3) electrolytic by precipitation at the cathode of an electrolytic cell, and 4) atomization through gas (illustrated in figure 2.5), water or using centrifugal forces. Knowledge of the fabrication method allows manufacturers to predict powder characteristics which in-turn helps achieve better green-compact properties [1].

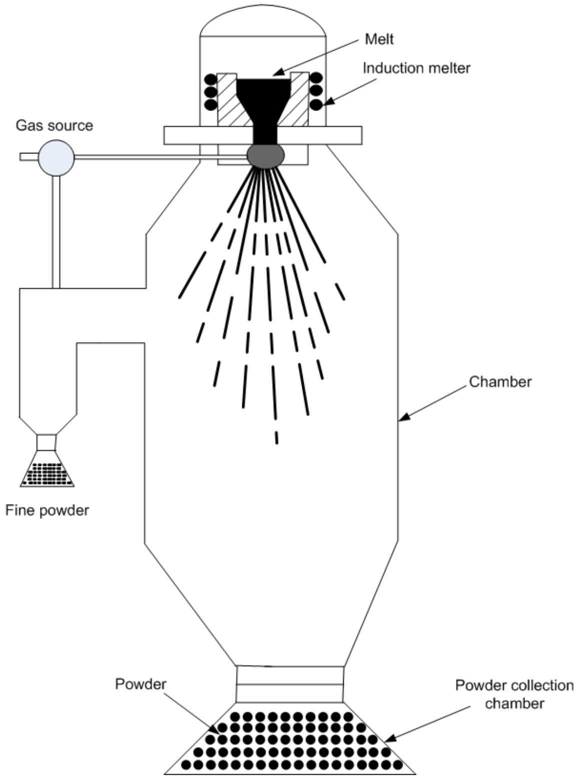

Figure 2.5: Vertical gas atomizer

As mentioned, powders are classified based on size and shape. Then, powders with different sizes (of the same chemistry) are mixed in a cylindrical, cubic, or double cone blender. The purpose of blending is to achieve a size distribution easier to compact and sinter. Moreover, blending aids in alloying when powders of different chemistries are mixed to form a new composition. Figure 2.6 shows a double cone blender used by many manufacturers today [2].

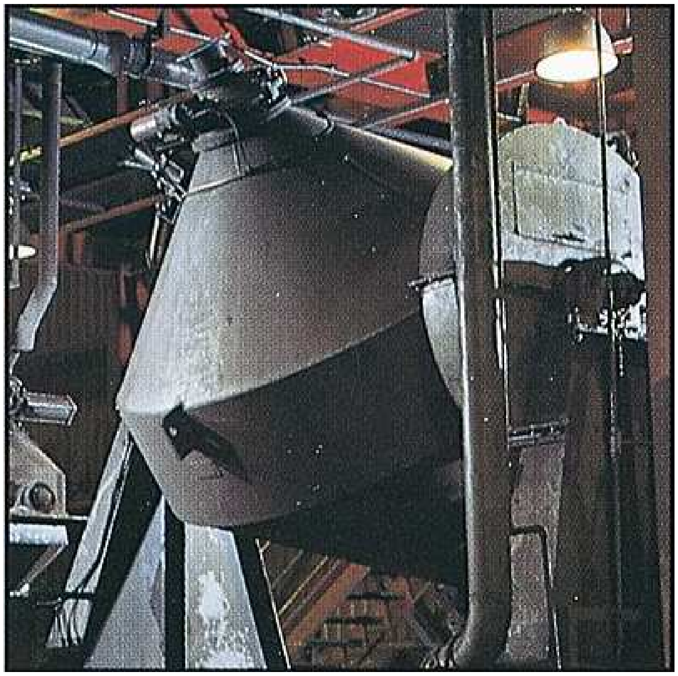

Figure 2.6: Mixing operation: double cone blender (Courtesy of GKN Sinter Metals).

Mixing occurs through one of the following basic mechanisms: diffusion, convection or shear to accomplish the necessary homogenization in new compositions. Furthermore, due to size variations and shape irregularities, lubricants are introduced at this stage of the process to reduce frictional forces between powder particles allowing higher compaction pressures which results in parts with greater green-strength [3]. In addition to the the improvement in green strength, the presence of lubricants has the added benefits of reducing the risk of damage during part ejection and of minimizing the die wear, both failure mechanisms are due to the friction between the compact and the die wall.

Compaction

Mixing results in loose powders homogenized to uniformly distribute lubricants, binders and powders with various material constituents. The subsequent step of compaction forms the parts into the desired shape and allows the development of interparticle bonds. Press systems with high compression strength up to $1\,GPa$ are utilized to shape the compact and achieve densities approaching the theoretical (full) densities. Modern presses typically employ three part sets that include:

- An upper punch to pressurize,
- a lower punch to position, and
- a die to shape the part.

Compaction can be accomplished by using either a single punch or a double punch action [2]. Figure 2.7 illustrates the forming operation in a single-level part with double punch. An external feed shoe is employed to introduce the powder into the die (step 1). This operation is aided by the lower punch which makes a downward motion to insure that the powder is uniformly distributed. Thereafter, in step 2 the feed shoe is removed and in step 3 very high pressure is applied through the motion of both punches towards the center of the die. Step 4 is when the desired pressure is reached, the part is formed and the upper punch is removed while the lower one moves upwards pushing the green-state sample out of the die and away from the press by means of the feed shoe in step 5.

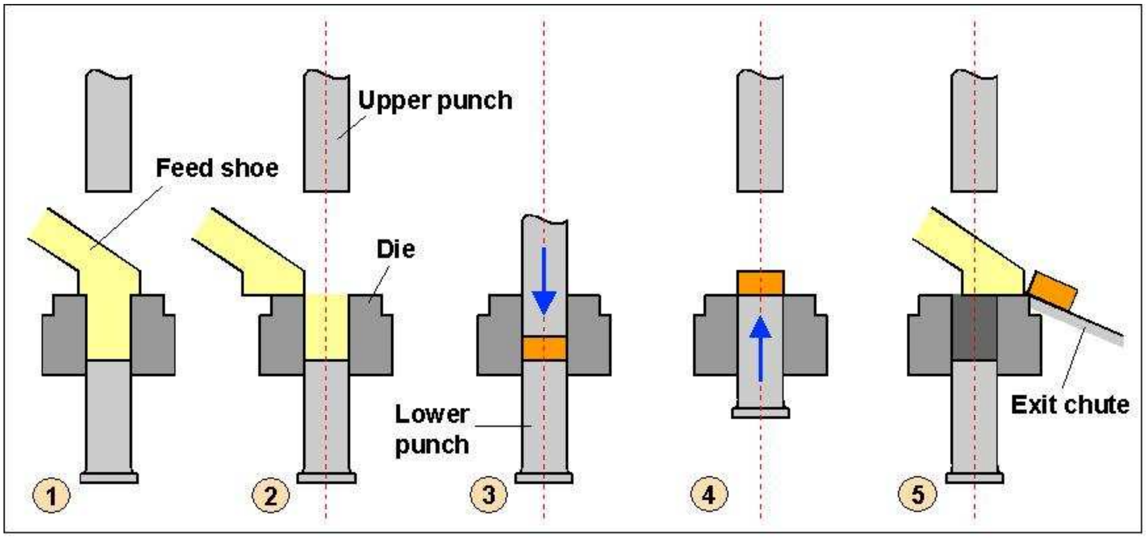

Figure 2.7: Compaction steps in a double punch press (Courtesy of GKN Sinter Metals).

The green-state sample at this stage is extremely fragile as there is no bonding agent between the powder particles other than the weak bonds created by the compaction. The manufacturing of complex, multilevel parts such as gears requires a high degree of sophistication and control during this step. Here punches are made of multiple moving parts to allow powder transfer between levels, this process helps accomplish uniform densities and prevents cracks, especially in corners. The problem of cracking in P/M is the major quality issue the industry faces and great efforts are exerted to thoroughly investigate its causes and devise prevention methods. Many of these limitations are caused by the friction between the die wall and the powder [1, 2].

To formulate the influence of the friction forces on limiting the applied pressure a simple model that utilizes a canonical shape such as the cylindrical part shown in Figure 2.8 is considered [3].

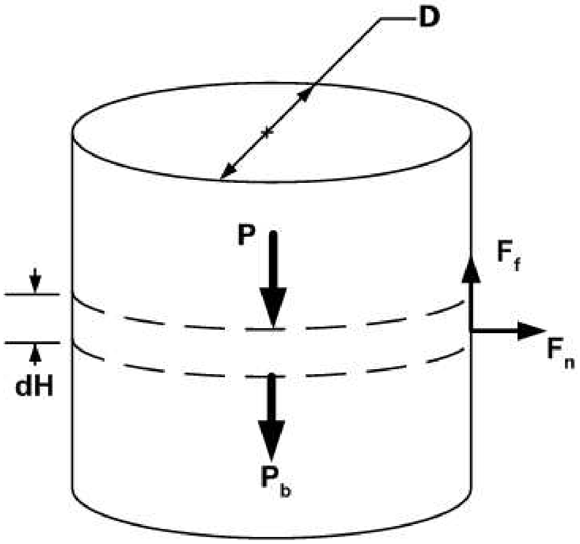

Figure 2.8: Transmitted pressure through an element of a cylindrical part and the balance of forces.

For simplicity we consider a press with a single punch action such that pressure is applied from the top and is transmitted to the bottom. The balance of forces on this compact is written as follows:

$$\sum_{i=1}^{2} F_i = 0 \tag{2.3}$$

$$A\left(P - P_b\right) + F_f = 0 \tag{2.4}$$

$$dP = P - P_b = -\frac{F_f}{A} \tag{2.5}$$

where A is the area of the compact where pressure is applied, P is the pressure applied on the part, P_b is the pressure transmitted through the part and F_f is the frictional force.

If a small element dH in the part the friction force is calculated as a function of the normal force where:

$$F_n = \pi z P D dH \tag{2.6}$$

where z is a proportionality constant to represent the ratio of the radial stress to the axial. The friction force is therefore:

$$\begin{aligned} F_f &= uF_n \\ &= u\pi zPDdH \end{aligned} \tag{2.7}$$

where u is the coefficient of friction between the powder and die wall.

combining (2.5) and (2.7) results in

$$\frac{dP}{P} = -\pi uz\frac{dH}{D} \tag{2.8}$$

The integration of (2.8) with respect to height gives the pressure P_x at a position x below the punch

$$\frac{P_x}{P} = e^{-\pi uzx/D} \tag{2.9}$$

Equation (2.9) shows that pressure decreases exponentially with depth or precisely with the height to diameter ratio.

In addition to cracking during pressing, ejection stress could exceed the strength of the green compact which will eventually break or incur a delamination damage during ejection. Thompson has formulated the ejection stress as

$$\xi = G\left(\frac{zuH}{D}\right)\left(\frac{1.27\,zuH}{D} + 1\right) \tag{2.10}$$

where G is the a shape factor. In practice for most shapes the ratio ${}^{uH}\!/_{D}$ is kept below 0.1 to minimize any damage during ejection.

Complex parts where the shape factor is high and part with relatively high height to diameter ratio are hard to manufacture with the standard compaction method, thus alternative approaches have been developed such as Cold Isostatic Pressing (CIP) where compaction is performed by pressurizing the part isostatically in a fluid bed (water or oil) through a rubber mold [2]. Further methods include warm compaction and injection molding.

Compaction is a critical step in the process and is the first step in the shape formation, hence its value in guaranteeing a quality product. Therefore, it is desirable to administer a quality check before proceeding to the sintering step. Sintering is the most critical and the most time and resource consuming step in the P/M process and it is the step that allow the part to reach acceptable mechanical properties.

Sintering

Subsequent to compaction is the sintering step where parts undergo well controlled heating to temperatures slightly below the melting point of the material. This heating results in the formation of bonds in the shape of welds that grow at the point of particle contact. The joining of particles results in parts that meet the requirements and the prescribed mechanical properties.

During this process great control of temperature is required to avoid undesired residues in the compact and to minimize the risk of thermal shock. Such control typically requires three individual steps. Therefore, three zones in the sintering furnace are needed to perform three separate tasks as illustrated in Figure 2.9. First, lubricants and other additives are removed through evaporation: it is accomplished by pre-heating the parts slowly. Thereafter, the compacts are heat treated for several hours to the highest possible temperature to form inter-particle bonds. This step is considered the main stage in sintering. The temperature is then slowly reduced in a controlled manner to prevent thermal shock [1], which may result in distortions or cracking: it is called the cooling stage.

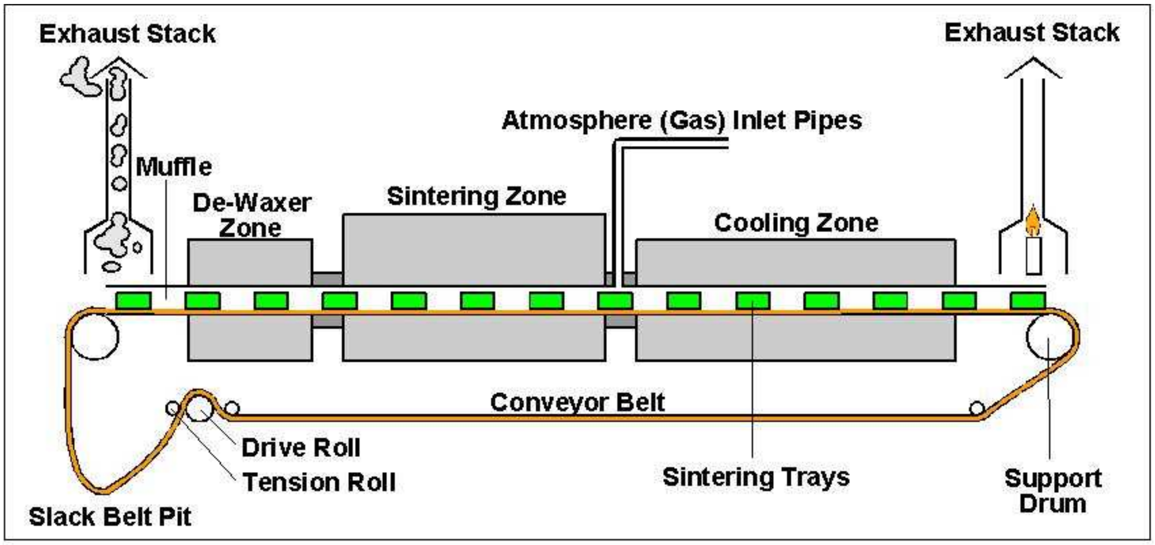

Figure 2.9: Generic sintering furnace (Courtesy of GKN Sinter Metals).

In the main sintering zone the process goes through three separate stages. In the initial stage described in Figure 2.10 a point contact between two particles grows to form a neck through a mass transport mechanism.

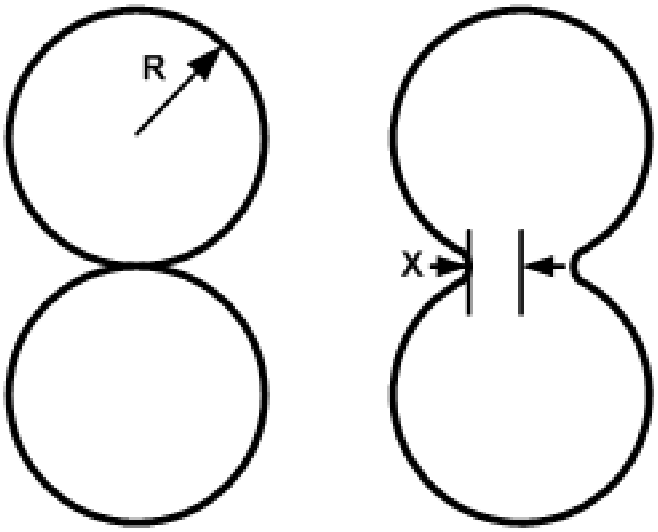

Figure 2.10: Neck formation between two powder particles.

This neck then grows slowly through a phenomenon represented by

$$\left({}^{X}\!/_{R}\right)^{n} = {}^{Bt}\!/_{R^{m}} \tag{2.11}$$

where X is the neck radius, R is the particle radius, t is the isothermal sintering time and B is a constant that depends on geometry and material parameters. The main observation in 2.11 is that the neck growth process or the first stage of sintering is highly dependent on the particle size; the finer the powder particle the higher is the rate of sintering. Furthermore, there is a dependency on the base material (encoded in B) as the favored mass transport mechanism varies with the material. Some materials favor surface diffusion while others favor lattice diffusion [1].

As neck grows shrinkage occurs as particles are closer. This property is in some cases beneficial when high densities are sought as shrinkage means the elimination of porosity. In other cases where geometric properties are more important shrinkage is avoided by forcing a specific mass-transport mechanism. Surface diffusion and evaporation-densification cause no shrinkage while lattice diffusion and grain boundary diffusion can result in shrinkage. This change in the overall dimension is estimated through

$$^{\triangle L}/_{L_0} = \left(^{X}/_{2R}\right)^2 \tag{2.12}$$

where L_0 is the initial length.

After the initial stage where neck growth takes place, the second or intermediate stage is representative of the process where densification starts such that grain growth occurs while pore are still interconnected. At the sintering temperatures grains grow at a high rate causing pores to break away, therefore, limiting the final density. Efficient sintering limits the growth of the grain through a precise temperature control a well selected particle size-distribution. In theory a law that governs grain growth for porous solids was established by Nichols as:

$$G^c = G_0^c + kte^{-Q_g/kT} \tag{2.13}$$

G_0 is the initial grain size, G is the grain size at time t , and Q_g is the activation energy.

At low temperatures grain growth is slow while high temperatures cause lead to breakaways in the grain boundary as grain mobility is increased. This stage of sintering is the most important as the pore structure is initiated here such that careful temperature control results in smooth interconnected pores attached to the grain boundary which then can be eliminated easily and densification occurs in a more uniform rate fashion. Isolated pores on the other hand are harder to eliminate and require higher temperatures which may affect the microstructure and cause high degree of shrinkage.

In the final stage of sintering isolated pores are eliminated. A bulk diffusion process shrinks the pores and causes grain boundary breakaways which in turn causes re-pinning such that larger pores absorb smaller ones [1].

Sintering is by far the most costly and time consuming step in the P/M process. A combination of temperature and sintering determine the quality of the final product (density). Due to quantity and quality requirements manufacturers focused substantial resources to devise methods to reduce the total time to sinter and lower the required temperature to sinter. In addition to these two parameters, these new methods aid in the elimination of pores therefore, achieving higher densities. These methods include activated sintering where additives are introduced with the metal powder. These additives are metals with lower melting temperatures and high solubility for the base metal. Such properties allows the added material (activator) to stay segregated at the interfaces to provide a high diffusivity path hence rapid sintering. Another related technique is liquid phase sintering, this method is specific to parts made with powders of mixed chemistries. In this case sintering is completed at a temperature where one of the elements liquidizes and forms a layer around the solid particles of the primary metal to allow rapid mass-transport. Example of such materials include Cu-Sn and Fe-Cu, which are very common in the industry [3].

At the end of the sintering step a finished part is produced with mechanical properties similar to a part manufactured with other metal working techniques. Several secondary operations might be necessary to meet a specific set of requirements such as hardness, corrosion resistance or to add geometric features unattainable with the basic process. These operations include sizing, machining, tumbling, oil impregnation, steam treatment, and heat treatment.

2.2 NDE Methods Applied to Process Control

Non-destructive Evaluation (NDE) is the examination of an object with technology that does not affect its future usefulness. NDE methods in manufacturing are applied to the process such that data from evaluation is used to adjust process variables including pressure, temperature, or time to ensure that parts fall within the prescribed quality limits. Testing could also be performed in an accept/reject mode where it deals with the finished product only. Non-destructive testing involves a physical phenomenon such as sound or light to act as the interrogating parameter. This parameter interacts with, or is influenced by, the test specimen and the interrogated parameter. Thereafter, data can be collected and displayed. It is clear, then, that the application or nature of the specimen to be tested impose requirements on the method and the test procedure. To choose the appropriate method for a specific application, it is important to understand the following:

- Properties of the bulk material,
- Underlying physical process that governs the method,
- Interaction between the probing field and the test material,
- Potentials and limitations of available technologies, and

- Sensitivity of the method.

As a special metal working method, P/M shares basic quality requirements with other techniques such as casting or forging. These requirements include dimensions, weight, strength, structural integrity, and purity. In addition to these basic requirements, P/M compacts require the verification of their densities. This is not limited to average density, but, perhaps more importantly, to the density distribution throughout the compact [4]. Furthermore, the fragile, brittle and porous nature of these parts in the green-state limit the choice of applicable methods.

The following paragraphs briefly introduce the most widely used NDE methods to enable us to conduct a comparative study and identify the pros and cons of each methodology.

Eddy Current

In standard eddy current testing, a circular coil excited by an alternating current (AC) source is placed in close proximity to an electrically conductive, non-ferromagnetic specimen as illustrated in Figure 2.11. The AC current in the coil generates a time-varying magnetic field, which interacts with the sample and induces circulating currents called eddy currents in accordance with Faraday's induction law. The eddy currents induced in the material create a magnetic field which opposes the primary field (Lenz's law) causing a reduction in the flux linkage associated with the coil. Variations in the electrical conductivity, or the presence of flaws or inclusions, will cause a change in the eddy current flow. This in turn will cause a decrease in the apparent resistance and reactance of the coil.

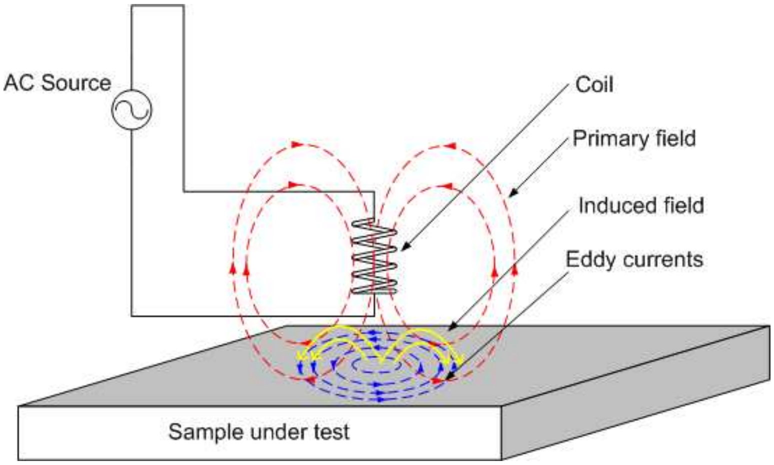

Figure 2.11: Eddy current testing.

Eddy current inspection is a widely used technique in surface and near-surface inspection of conductive materials. Among its benefits, it is contact-less and it is effective in a wide range of applications such as defect detection, thickness evaluation, and conductivity measurement. The major disadvantages include the dependence on surface roughness, the limited depth of penetration, flaws that lie parallel to the probe may go undetected and the fact that it requires skilled operators.

Ultrasonic Testing

Ultrasonic Testing (UT) uses elastic waves to conduct examinations and make measurements. Ultrasonic inspection can be used for flaw detection, dimensional measurements, material characterization, and a multitude of other applications.

Figure 2.12 illustrates a typical pulse/echo UT inspection system: it consists of three main functional units, including a pulser/receiver, transducer, and display devices. The pulser/receiver produces a high-voltage electrical pulse to drive the piezoelectric ultrasonic transducer. Driven by the pulser, the transducer generates high frequency ultrasonic energy (typically in the range from 1-50MHz). The sound wave is introduced into the sample under test and propagates through its bulk until a discontinuity (such as a crack) is encountered in the wave path. At the discontinuity portion of the energy will be reflected back to the transducer. The reflected wave signal is transformed into an electrical signal by the transducer. The signal travel time can be directly related to the distance that the signal propagated. From the signal, information about the reflector location, size, orientation and other features can be inferred.

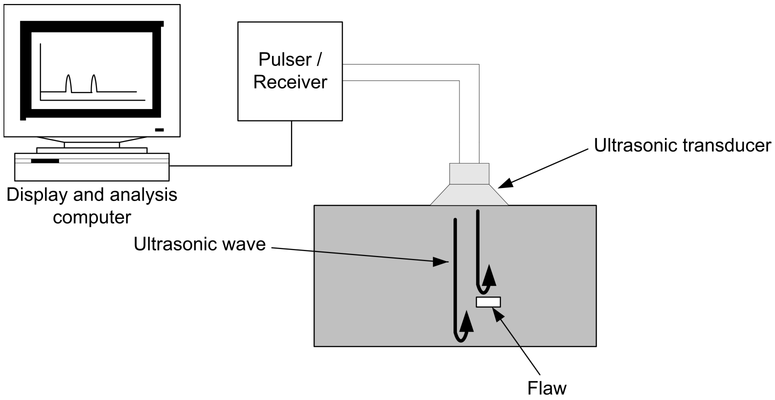

Figure 2.12: Ultrasonic pitch/catch test arrangement.

Ultrasonic testing is one of the most versatile NDT methods with a very wide range of applications. This is due to the number of possible wave models that can be used to detect specific types of defects and defect orientations located at various depths. To apply the technique, however, the specimen under test is contacted, and a coupling agent is required. In many applications such as testing green-state compacts contacting the sample and using the couplant can be damaging.

X-Ray Imaging

X-ray inspection or radioscopy is a well known and understood method due to its use in medical imaging. It is based on the absorption of X-rays by the sample under test. Specifically, it uses an X-ray tube to emit a beam of ionizing radiation. The radiation passes through the part being inspected and impinges on the imaging device as shown in Figure 2.13.

As the beam travels through the sample, the X-ray energy is attenuated in proportion to the material thickness. The presence of flaws, inclusions or pores will cause a reduction in attenuation. The imaging device includes an image intensifier that produces a high resolution image that displays the attenuation profile.

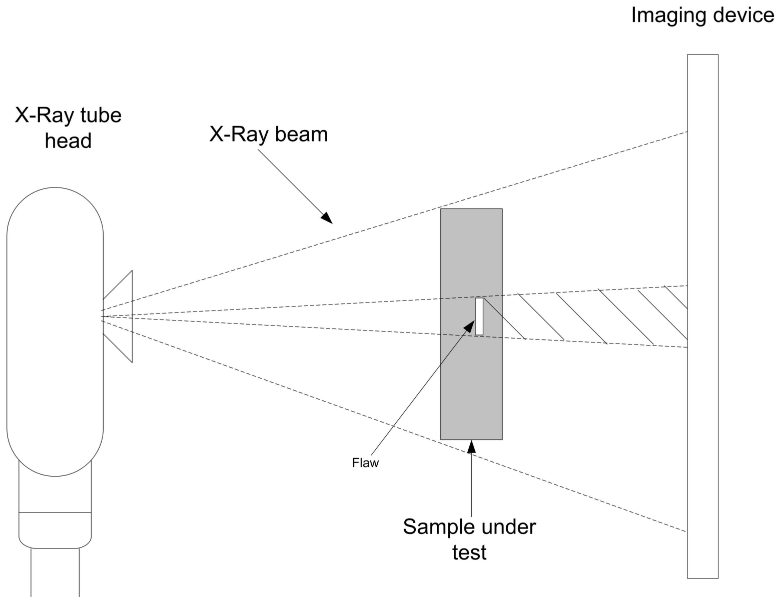

Figure 2.13: X-ray testing with a radiation source.

Although this method has the potential to detect the widest number of possible defects and is the most effective in detecting deeply embedded cracks, it is also the most expensive to operate and the most hazardous. It is therefore rarely used in manufacturing. However, a variant of the technique is shown in Figure 2.14. This approach to X-ray imaging is used in comprehensive analysis by forming the images a florescent device instead of the traditional film. This will allow for a computerized data processing and a more effective storage of the images. Furthermore, advances in computing resulted in the ability to produce three-dimensional cross-sectional images of an object from X-ray images; this is known as computerized tomography (CT) [4].

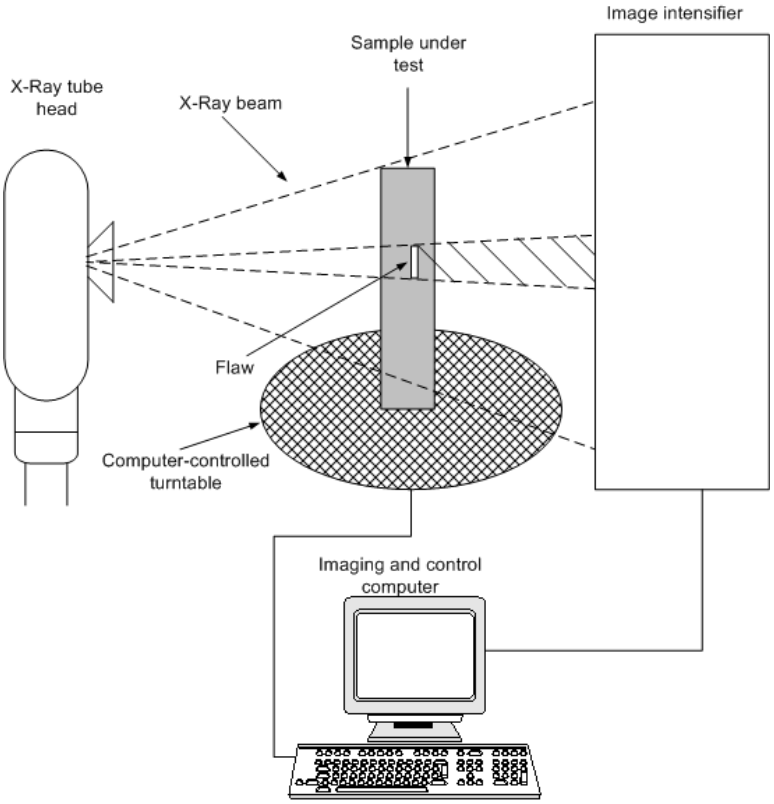

Figure 2.14: Computed tomography (CT).

Resonance Testing

Resonant inspection evaluates the vibrational behavior of the samples under test. First, the part is excited either with low frequency harmonic elastic waves over a certain bandwidth, or through impacting the sample. Then, the resonance frequency responses are measured with separate transducers such as piezo-receivers operating as receivers as shown in Figure 2.15. Abnormalities encountered in a defective part will result in shifts of the resonance spectra. Therefore, the resonance technique compares the spectral response of an unflawed part with the shifted spectral response of a flawed part. This is completed typically with a Fourier analysis which has the disadvantage of slow response and high sensitivity to noise.

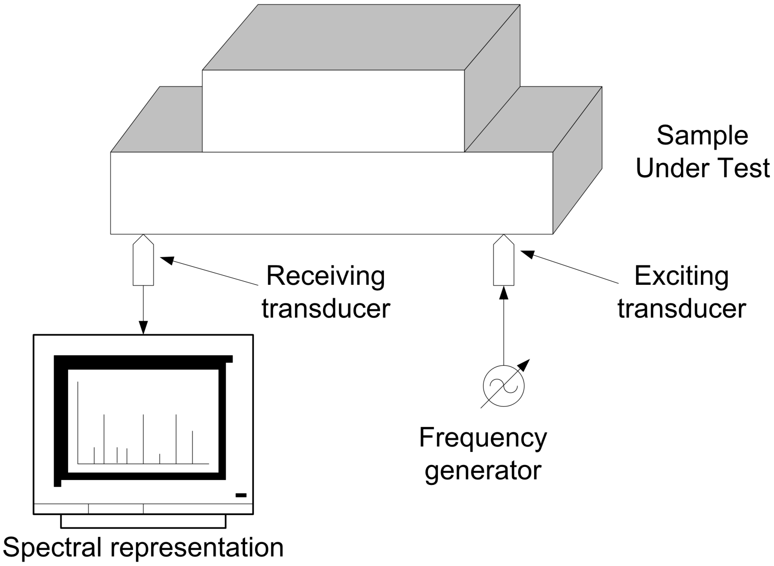

Figure 2.15: Basic resonance test arrangement. A wide-band transducer generates a spectrum of resonances that is recorded by a second receiving transducer.

Although this technique is becoming more and more prevalent due to its cost effectiveness, it still suffers from many drawbacks such as the need for an exhaustive database of resonant frequencies, especially in the case of complex parts. Moreover, due to its noise sensitivity it is only useful in detecting relatively large cracks.

Electrical Resistivity

The traditional electrical resistivity inspection method illustrated in Figure 2.16 utilizes four in-line probes to measure the resistance of the material in the area of interest. The outer probes are used to feed current into the sample under test and the inner probes measure the voltage drop across them. The benefit of this method over a simple two wire method is that the voltage is measured next to the current carrying leads. This eliminates the lead resistance effect [5] . The accuracy of this method depends mainly on the ability to precisely record the voltage drop for a given current.

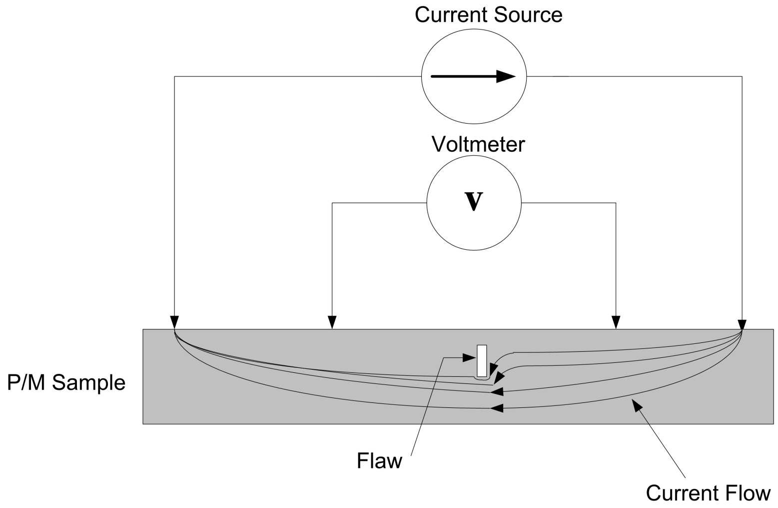

Figure 2.16: Four-probe resistivity measurement setup.

In P/M compacts, material properties can be inferred from the conductivity of the material [4, 5, 6]. The technique has been successful in the detection of surface and near-surface defects. However, it suffers from two main drawbacks. First, the coverage of the sensor is very limited. Therefore, a complete test requires indexing the probe across the entire surface of the sample. Second, conflicting requirements might arise between resolution and the ability to detect deep subsurface flaws, where the spacing between the probes is the determining factor. Typically, the resolution is increased by reducing the spacing between the probes and the depth of detection is improved by increasing the spacing [4].

To overcome these limitations an apparatus for crack detection in green-state P/M compacts was developed and patented at Worcester Polytechnic Institute. This apparatus uses a technique that is an extension of the basic resistivity measurement principles where a multi-probe sensor, shown in Figure 2.17, is used.

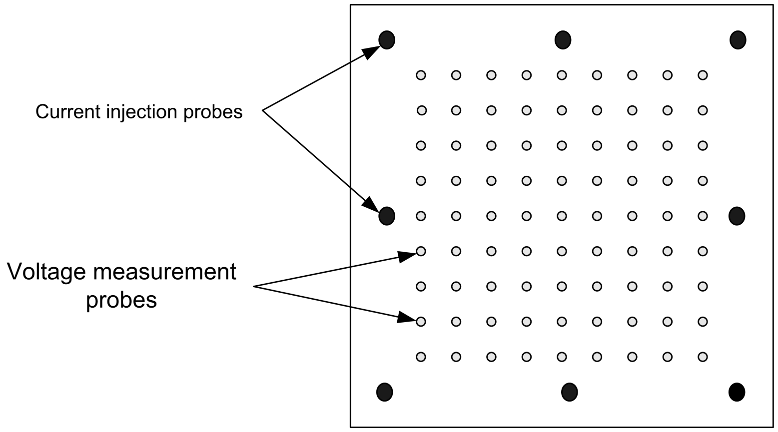

Figure 2.17: Multi-pin planar sensor.

Here a multiple current injection pattern based on a plurality of current probes is utilized in conjunction with a large number of voltage probes covering the entire area of the sample under test. The system enables the measurement of the voltage distribution over a large surface area. It enhances the ability of the apparatus to detect both small surface cracks and deep subsurface defects.

Chapter 3

Thermography

3.1 Introduction

Thermography or thermal imaging is a rapidly growing remote sensing NDT technique; its basic premise tests on combining a sensor that detects radiation in the infrared spectrum, see Figure 3.1, with a computer system (or processor) to display a two-dimensional image that represents the surface temperature of an object. In contrast with imaging in other electromagnetic (EM) wave spectra where either reflection or absorption is measured, in infrared imaging it is the emission from the specimen that is directly detected. Thereafter, the signal representing the intensity of the infrared radiation is processed through the computer subsystem to display thermal maps or thermograms. In fact, the computer system performs complex processing beyond the simple intensity-temperature transformation. It applies the necessary corrections to the measurement and calibrates the sensor to the absolute temperature values. Some examples of computer processing include the elimination of the components due to radiation from the surroundings, the reflection from the part under test and the compensation for atmospheric absorption.

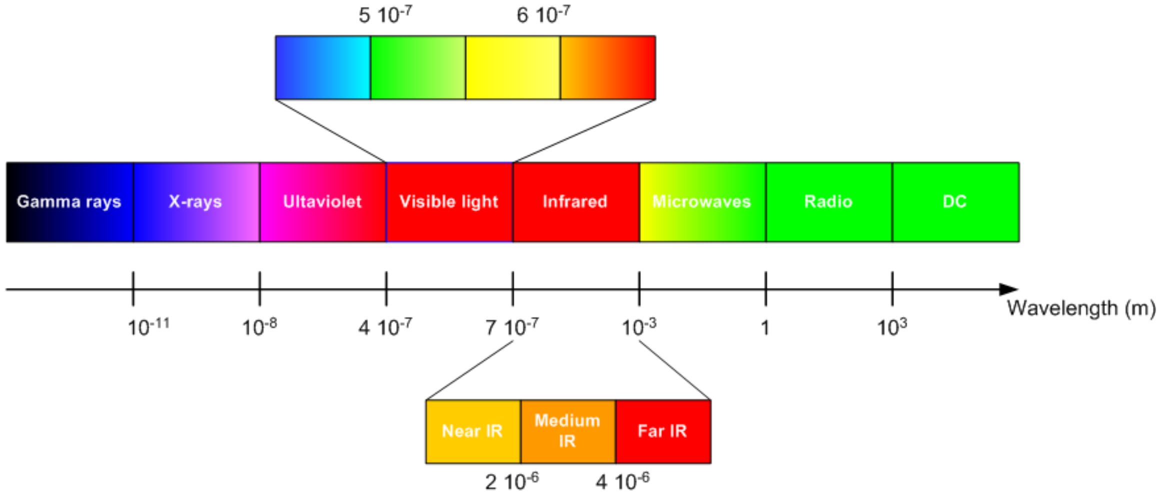

Figure 3.1: Electromagnetic spectrum as a function of wavelength.

The following paragraphs list the advantages and limitations of thermography, highlight major applications where the technique is applied, and describe the basic infrared formulation along with detection parameters.

3.2 Merits and drawbacks of thermography

Because all objects radiate in the infrared spectral range, remote temperature sensing is possible. The surface temperature can then be utilized as an indicator to infer quality of the specimen under test. From a practical perspective, thermography is a technique with numerous benefits such as:

- Easy to deploy: generically no sample preparation or learning cycles for the imager are required to initiate testing. From a hardware perspective, a thermography setup only requires an imager and an optional heat source.
- Contactless: passive testing approach is fully contactless and active testing largely depend on the heat deposition mechanism which can be chosen to meet the non-contacting requirement (alternative current, flash lamps or lasers).

- Versatile: this method is not subjective or part-specific, a setup can be used for different samples with minimal changes and with no impact on process yield.
- Fast: infrared imaging provides a real time temperature map of a surface. Hence, it provides a fast quality feedback which can be used in on-line applications for one hundred percent testing.
- High resolution: modern imagers possess spatial resolutions of less than $100 \mu m$ and thermal sensitivity better than $0.08^o K$.

The known drawbacks of the infrared imaging technique include:

- Direct measurement of the surface only: infrared imaging is a surface measurement method and 3-D reconstruction is only inferred through projections, perspectives or from a transient analysis of a sequence of 2-D images. This limitation becomes significant in the detection of minute deeply embedded defects.
- Classical imaging impossible to apply: the technique exploits diffusion, rather than wave phenomena. This makes classical imaging that relies on reflection/transmission impossible to employ.
- Straight viewing angle: a direct viewing corridor is required which limits the applicability of the technique [7, 8].
- Uniform heating (when required): generally it is challenging to obtain and maintain uniform heating throughout a specimen.
- Cost of the thermal camera: historically the cost of an infrared imaging system for the inspection of high-volume, low cost samples is prohibitive largely due to the expensive detectors and the cooling system (usually a cryogenic engine). However, modern instruments employ very stable solid state uncooled photovoltaic cells that are easily manufacturable.

3.3 Applications of infrared imaging

Infrared imaging has long been used in defense, surveillance and border control applications. Currently it is gaining wide-spread popularity in many other fields due to the benefits listed above. Recently, thermography has been used in such diversified areas as:

1. Medical: to detect tumors, allergen reactions, soft tissue injuries and blood flow.
2. Military: to find enemy soldiers and hidden equipment in low visibility situations.
3. Social services: fire detection and prevention and localization of victims and firefighters in smoke filled areas.
4. Building maintenance: checks for leaks and degradations in walls or roofs.
5. Electronics and power plants: to find defects, dissipating components, miswiring in circuit boards and to assess solder quality.
6. Materials: for the detection of defects, corrosion, disbonding, impact damage lap-joints in spot welding and fatigue. It is also employed in thickness measurement and to determine various material properties.

3.4 Active thermography methods

This basic approach is termed passive as it does not require an active heat source. In many applications, however, the required sensitivity is not reachable unless an external energy source is utilized to create the necessary thermal contrast between the material and the defect. In such a case, the method is said to be active and energy is deposited based on several procedures and where the overall system takes different embodiments. Furthermore, the inversion algorithm and signal processing depend on the heating method and the detector type.

In the following discussion we list the most common embodiments of the technique and the differences thereof.

3.4.1 Pulsed-heating

Active pulsed thermography is the imaging of a specimen that has been heated for a very brief period of time. Detection can focus on either the temperature rise or decay depending on the application. The ability to rapidly deposit energy brings a number of benefits, including: elimination of the risk of damage to the sample under test, fast response, and most notably the ability to detect subsurface defects. This multidimensional characteristic space-time allows this approach to be used in applications requiring defect localization and characterization. The contour of a subsurface defect in test piece is highlighted by hot spots and depth information is encoded in the delay time between energy deposition and temperature increase as described by the empirical relationship shown in (3.1) [8, 9]

$$t \sim \frac{z^2}{\alpha} \tag{3.1}$$

where α is the thermal diffusivity of the material and z is the defect location away from the surface.

In addition to the time delay, another important parameter is utilized to determine the depth of the defect; the loss of contrast c is related to the depth as described by (3.2) [8, 9]

$$c \sim \frac{1}{z^3} \tag{3.2}$$

3.4.2 Step-heating

Step heating or time-resolved infrared radiometry (TRIR) utilizes a long pulse of heat and temperature is monitored as time evolves[10]. It is widely used for thickness measurement, determination of coating parameters and similar applications. An empirical relationship, see (3.3), has successfully been in use to determine the thickness of a coating layer. The characteristic time t_c is related to the thickness of the coating l and the thermal diffusivity of the material α according to

$$t_c \sim 0.36\,\frac{l^2}{\alpha} \tag{3.3}$$

3.4.3 Lock-in thermography

Lock-in thermography utilizes an oscillating heat source to generate a harmonic temperature profile on the surface of the sample under test. Figure 3.2 describes a lock-in thermography system where a heat source deposits power onto a sample while a camera is synchronized to the heat source to extract amplitude and phase information.

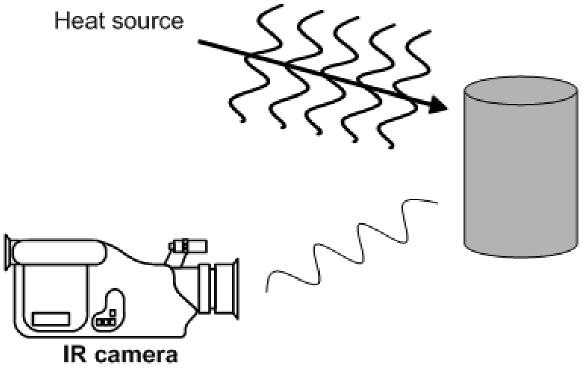

Figure 3.2: Lock-in thermography

Heat conduction is a diffusion process governed by a parabolic partial differential equation (PDE). Therefore it lacks the second order temporal derivative which characterizes the wave equation. However, a wave-like behavior can be ascribed when classical diffusion is coupled with an oscillatory force function emanating from a modulated external heat source. The result are thermal "waves" that are highly attenuated and dispersive inside the material [11].

A common approach to generate these waves is to use a light beam that deposits energy onto the specimen with the optical waves modulated at constant frequency[10]. The light incident on the part upon absorption causes an optical-thermal energy conversion and a surface localized oscillating temperature field is generated.

As we know, the homogeneous heat equation can be cast in the form

$$\nabla^2 T - \frac{1}{\alpha}\frac{\partial T}{\partial t} = 0 \tag{3.4}$$

where α is the thermal diffusivity, which is related to the thermal conductivity k through the equation $\alpha = \frac{k}{\varrho c}$ with ϱ being the density and c the specific heat.

The temperature close to the surface of the material is a combination of the ambient temperature, a time independent temperature rise and a periodic temperature oscillation due to the incident light beam (modulated at $f = \frac{w}{2\pi}$), the resulting temperature is written as:

$$T\left(x,t\right) = T_{amb}\left(x\right) + T_{rise}\left(x\right) + T_{osc}\left(x,t\right) \tag{3.5}$$

where

$$T_{osc}\left(x,t\right) = Re\left[\theta\left(x\right)e^{jwt}\right] \tag{3.6}$$

with θ is the time independent temperature. It is similar to the voltage or current phasor in electromagnetics.

Substituting (3.5) in (3.4) results in the time-independent component that obeys the Helmholtz equation

$$\left(\nabla^2 + q^2\left(x\right)\right)\theta\left(x\right) = 0 \tag{3.7}$$

with the complex wavenumber being defined as

$$q(x) = (1 + j)\sqrt{\frac{w}{2\alpha(x)}} \tag{3.8}$$

For the homogeneous case and if a semi-infinite specimen is heated by a uniform source. By using as a boundary condition the heat flux continuity on the surface of the specimen

$$-k\,\frac{d\theta(x)}{dx}|_{x=0} = \frac{I_0}{2} \tag{3.9}$$

the solution becomes

$$T_{osc}(x,t) = \frac{I_0}{2\,\text{eff}\,\sqrt{w}} e^{-x/\mu} cos\left(wt - \frac{2\pi x}{\lambda}\right) \tag{3.10}$$

Here, μ is the thermal diffusion length, I_0 is the intensity of the light beam, eff is the thermal effusivity, and λ is the thermal wavelength with: $\lambda = 2\pi\mu$

$$\mu = \sqrt{\frac{2k}{w\rho C}} = \sqrt{\frac{2\alpha}{w}} \tag{3.11}$$

The propagation speed $v = \lambda\frac{w}{2\pi} = \sqrt{2w\alpha}$ and the phase term $\varphi = \frac{2\pi x}{\lambda} = \frac{x}{\mu}$

We note that μ (diffusion length) and w (modulation frequency) are inversely proportional. Hence, slower heating will result in deeper penetration. Similar to electromagnetic wave propagation when this wave meets an interface inside the material it is reflected and the reflection coefficient is written as

$$R = \frac{b-1}{b+1} \tag{3.12}$$

With $b = \frac{eff_2}{eff_1}$ and $eff_i = \sqrt{k_i \rho_i C_i}$ with $i = 1$, 2...., N the thermal effusivity.

This behavior is captured by the imager in the form of a sinusoidal electrical signal proportional to the temperature with an in-phase signal $S_0(x,y)$ and an out-of-phase signal $S_1(x,y)$ such that two images are formed; the phase independent amplitude image $A(x,y)$ and the phase image $\phi(x,y)$ where:

$$A(x,y) = \sqrt{S_0^2(x,y) + S_1^2(x,y)} \tag{3.13}$$

and,

$$\phi(x,y) = \arctan\left(\frac{-S_1(x,y)}{S_0(x,y)}\right) \tag{3.14}$$

Phase information is also used in the inversion process through a new parameter, the phase contrast defined by

$$\triangle\phi = \phi_d - \phi_s \tag{3.15}$$

where ϕ_d is the phase for a defective area, and ϕ_s is the phase of a sound area of the sample.

3.4.4 Vibrothermography

Vibrothermography is an infrared based non-destructive evaluation method where heating is induced through vibrations caused by a contact sonic transducer, as depicted in Figure 3.3. The elastic waves interact with defects such as voids, cracks or delaminations to cause frictions, stresses and strains at the tip of a crack which results in a distinct thermal signatures [12].

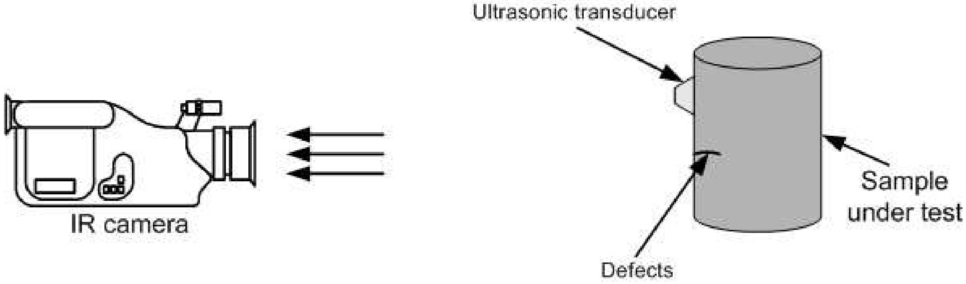

Figure 3.3: Vibrothermography setup

Stresses and strains are obtained from the equation of motion and the resulting modes of vibrations are represented by the fourth order wave equation for a circular plate:

$$\nabla^4 u + \frac{3\rho\left(1-\sigma_p^2\right)}{Eh^2}\frac{\partial^2 u}{\partial t^2} = 0 \tag{3.16}$$

with u is the out of plane displacement, σ_p is Poisson's ratio, E is the modulus of elasticity, and h is the half thickness.

The characteristic function is

$$v\left(r,\theta\right) = cos\left(m\theta\right)\left[J_m\left(\frac{\pi\beta_m r}{R}\right) - \frac{J_m\left(\pi\beta_{mn}\right)}{I_m\left(\pi\beta_{mn}\right)} I_m\left(\frac{\pi\beta_{mn} r}{R}\right)\right] \tag{3.17}$$

m and n are integers that define the vibration mode, J_m is the Bessel function of the first kind, I_m is the modified Bessel function of the first kind, R is the radius of the plate and $\beta_{mn}$is the mode factor. The roots of (3.17) are related to the frequencies of vibration such that

$$f_{nm} = \frac{\pi h}{2R^2}\sqrt{\frac{E}{3\rho\left(1-\sigma^2\right)}}\beta_{nm}^2 \tag{3.18}$$

This method is relatively successful in the detection of most defects including cracks that are normal to the surface being imaged. It suffers however from a major drawback due to the requirements for a mechanical contact with the part and a large amplitude of the acoustic signal. These two parameters may cause damage to the sample under test at the interface [13, 14].

3.5 Radiation parameters

The mechanism of heat emission is related to the thermal energy released as a result of oscillations or transitions of the electron energy states that constitute the medium. These oscillations, are in turn, sustained by the internal energy which is determined by the temperature of the medium.

Thermal radiation is a surface effect because the radiation emitted by interior molecules is strongly absorbed by adjoining ones. Thus, the thermal radiation is limited to the molecular layers that are either on the surface or at approximately $1\mu m$ below the surface.

This thermal transfer mechanism can be viewed as propagation of electromagnetic waves of a range of wavelengths. Similar to an antenna system, the directionality of the radiation becomes very important, as depicted in Figure 3.4. For this reason, it is necessary to study both the spectral distribution and the directional distribution of the radiation in order to accurately determine the energy and the temperature of a heated specimen.

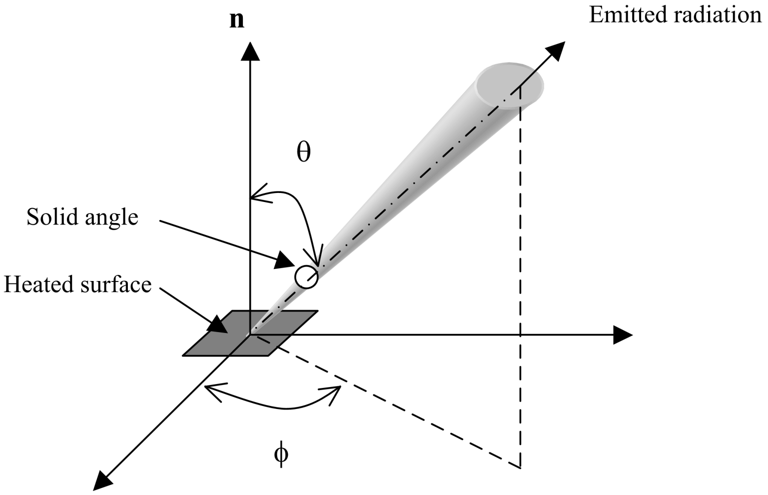

Figure 3.4: Directional nature of infrared radiation emanating from a heated surface element.

The rate at which radiated energy is emitted at a particular wavelength in a specific direction is a function of the area of the emitting surface normal to the direction, the solid angle typically identified by $d\Omega$, and the spectral interval [15]. It is referred to as the *spectral intensity*

$$L_{\lambda,e}\left(\lambda,\theta,\phi\right)=\frac{d^3\boldsymbol{\phi}}{dA\,\cos\theta\,d\Omega\,d\lambda} \tag{3.19}$$

By integrating this entity (the spectral radiance) over a finite surface and a finite wavelength we find the radiant power, also called the *spectral exitance* $M\left(\lambda\right)$. For a so-called Lambertian surface (isotropically diffuse), the exitance $M\left(\lambda\right)$ is:

$$M\left(\lambda\right) = \pi L\left(\lambda\right) \tag{3.20}$$

A spatial integration on the other hand, will result in the *spectral hemispherical emissive power* $E_\lambda\left(W/m^2\right)$, which quantifies the rate at which radiation is emitted in all directions from a surface per unit wavelength and per unit area. This quantity is regarded as a flux emanating from the area of the compact and is expressed as follow

$$E_\lambda\left(\lambda\right) = \int_0^{2\pi}\int_0^{\frac{\pi}{2}} L_{\lambda,e}\left(\lambda,\theta,\phi\right)\cos\theta\,\sin\theta\,d\theta\,d\phi \tag{3.21}$$

To quantify the total emissive power E_e one has to consider all possible wavelengths. This is accomplished by integrating over λ :

$$E_e = \int_0^{\infty} E_\lambda\left(\lambda\right)d\lambda \tag{3.22}$$

A qualitative analysis of radiation effects often uses a baseline. Namely, a gold standard to reference all radiation parameters, and to be used as a reference for subsequent measurements. This object has the property of being the perfect emitter and the perfect absorber at the same time [15, 16]. Emissions emanating from this object are independent of direction and wavelength. This object is called a *blackbody* and its spectral radiance is given by Planck's law

$$L_{\lambda,b}\left(\lambda,T\right) = \frac{c_1}{\pi\lambda^5\left[\exp\left(\frac{c_2}{\lambda T}\right)-1\right]} \tag{3.23}$$

Here T is the temperature of the target in Kelvin, and c_1 and c_2 are constants. This equation yields a set of graphs known as the blackbody emissivity power. We find for P/M samples at the temperature of interest that the peak radiation occurs between $7\mu m$ to $15\mu m$, as shown in Figure 3.5.

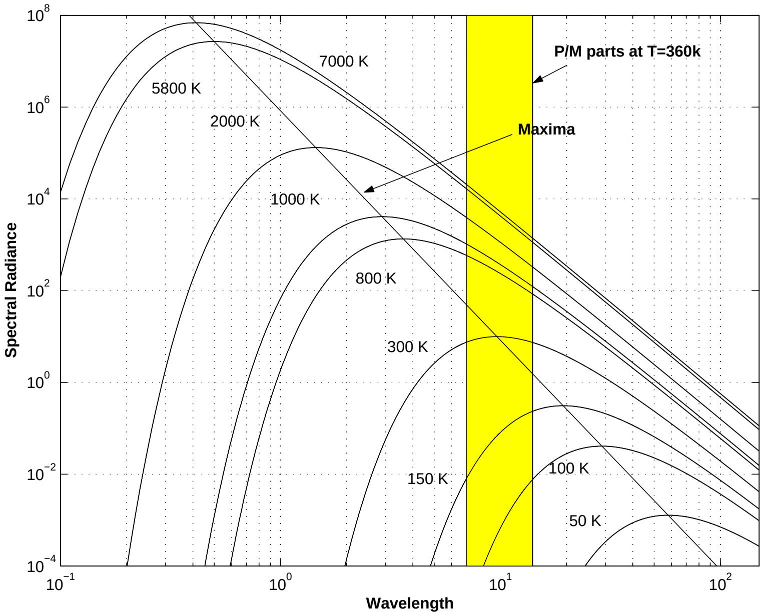

Figure 3.5: Black body radiation spectrum.

The Wien displacement law determines the locus of the maximum spectral radiance for a given temperature by taking the derivative of Planck's law with respect to the wavelength. Wien displacement law is depicted in the following expression

$$\lambda_{max} = \frac{c_3}{T} = \frac{2897.7}{T} \tag{3.24}$$

where c_3 is the third radiation constant.

A simpler approach to calculate the amount of radiation in all directions and across all wavelengths is based on Stefan-Boltzmann's law. Here temperature is the only parameter needed as given in the following expression

$$E_b = \sigma_{SB} T^4 \tag{3.25}$$

σ_{SB} is the Stefan-Boltzmann constant. It has the numerical value of $\sigma_{SB} = 5.670 \times 10^{-8} W/m^2\,{}^\circ K^4$.

Unfortunately, a real surface is neither a perfect emitter nor a perfect absorber. We therefore define an additional surface property to express the ability of a body to emit energy. This property is used as a correction factor and is called emissivity e. It is a unitless factor that spans from 0 for a total reflector to 1 for a blackbody. The emissivity depend on several spectral, spatial and material parameters. Emissivity is of major concern in IR imaging due to the fact that the radiance and hence temperature is directly proportional to the emissivity as illustrated in (3.26). For example, for a surface having a spectral emissivity $e\left(\lambda\right)$, the radiance is expressed as:

$$L_{\lambda,e(\lambda)}\left(\lambda,T\right) = e\left(\lambda\right) L_{\lambda,b}\left(\lambda,T\right) \tag{3.26}$$

Metals in general, and P/M samples in particular, posses low emissivity. This makes accurate IR radiometry very challenging and in some cases impossible. Furthermore, the thermal dependency of the emissivity greatly limits the applicability of IR thermography. However, all these shortcomings can be overcome with a judicious choice of the temperature at which the measurement is conducted.

3.6 Infrared Detection

Our thermal system does not measure temperature directly, but rather it records the radiant flux received by the imager from an area of interest subtending the solid angle at the camera, weighted by the imager's spectral response.

In general, the radiation stems from three sources: the radiation coming directly from the sample, the radiation incident and reflected from the sample, and the radiation emitted by the atmosphere. Therefore, we write the radiation with its three components (see Figure 3.6) as a sum

$$S = S_s + S_r + S_{at} \tag{3.27}$$

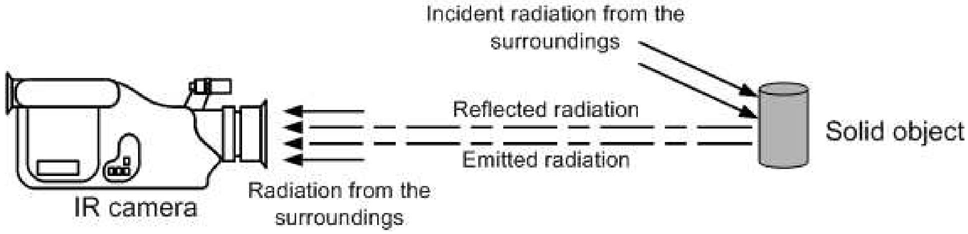

Figure 3.6: Radiation and reflection from a point on the surface of a P/M part.

Specifically, the component arising from the radiation emitted by the sample is given by

$$S_s = K \int_0^\infty L(\lambda) A_{at} R(\lambda) d\lambda \tag{3.28}$$

Here A_{at} is the spectral transmission of the atmosphere, and $R(\lambda)$ is the effective spectral responsivity of the imager's detector (transmission of the lens and any additional elements in the optical path).

Similarly, we can derive the radiation reflected from the sample and the radiation emitted by the atmosphere between the camera and the sample.

$$S_r = K \int_0^\infty \rho(\lambda) E(\lambda) A_{at} R(\lambda) d\lambda \tag{3.29}$$

Here, $\rho(\lambda)$is the spectral reflectance and $E(\lambda)$is the spectral irradiance from external sources. We define the relationship between the emissivity and the reflectance

$$\rho(\lambda) = 1 - e(\lambda) \tag{3.30}$$

In the limit, and for a surface with an emissivity of 1, (3.30) shows that there is no reflected radiation from the sample.

Finally, the atmospheric radiance can be described as

$$S_{at} = K \int_0^\infty L_{at}(\lambda)\, R(\lambda)\, d\lambda \tag{3.31}$$

where $L_{at}(\lambda)$is the spectral radiance of the atmosphere.

Commercial imagers measure changes in the optical detector's signal levels caused by changes in the incident radiation. This signal is usually clamped to a fixed level by a signal level arising from an internal radiation source. Therefore, the detector measures the resulting differential, given by

$$\Delta S = S - S_0 \tag{3.32}$$

with S being the incident radiance that includes all the sources, and S_0 is the internal reference (a blackbody source $L_{\lambda,b}$) described by:

$$S_0 = K \int_0^\infty L_{\lambda,b}(T_0, \lambda)\, R(\lambda)\, d\lambda \tag{3.33}$$

where T_0 is the equivalent blackbody temperature of the internal source.

We can then predict what is actually recorded by the detector; this signal is then processed to separate various effects, and calibrated with a well known set of parameters that ensure accuracy and repeatability. The recorded signal by the detector is

$$\begin{aligned} \Delta S &= K \int_0^\infty A_{at}(\lambda)\, R(\lambda) \left[e(\lambda)\, L_{\lambda,b}(\lambda, T) + (1 - e(\lambda))\, L_{\lambda,b}(\lambda, T_{sr})\right] d\lambda \\ &+ K \int_0^\infty R(\lambda) \left[(1 - A_{at}(\lambda))\, L_{\lambda,b}(\lambda, T_{at}) - L_{\lambda,b}(\lambda, T_0)\right] d\lambda \end{aligned} \tag{3.34}$$

This equation represents a signal that is considered an accurate representation of temperature. The drawback, however, is related to the fact that (3.34) is rather complex to numerically evaluate and display in real time. A compromise is needed in this case where we trade-off accuracy for simplicity. To do so, we first consider the target to be a "gray-body" eliminating the spectral dependency on its emissivity. Secondly, we consider the transmission of the atmosphere to be independent of wavelength; this assumption is relatively realistic due to the limited spectral band of the imager [17]. These considerations simplify (3.34) to

$$\begin{aligned} \Delta S &= KA_{at}\left[e\int_0^\infty L_{\lambda,b}\left(\lambda,T\right)R\left(\lambda\right)d\lambda+\left(1-e\right)\int_0^\infty L_{\lambda,b}\left(\lambda,T_{sr}\right)R\left(\lambda\right)d\lambda\right] \\ &+ K\left[\left(1-A_{at}\right)\int_0^\infty L_{\lambda,b}\left(\lambda,T_{at}\right)R\left(\lambda\right)d\lambda-\int_0^\infty L_{\lambda,b}\left(\lambda,T_0\right)R\left(\lambda\right)d\lambda\right] \end{aligned} \tag{3.35}$$

As can be seen, the above equation involves integrals that have the same form, making further simplification possible through the use of the following identity

$$C\left(T\right)=\int_0^\infty L_{\lambda,b}\left(T,\lambda\right)R\left(\lambda\right)d\lambda \tag{3.36}$$

Hence, (3.35) becomes

$$\Delta S=K\left\{A_{at}\left[eC\left(T\right)+\left(1-e\right)C\left(T_{sr}\right)\right]+\left(1-A_{at}\right)C\left(T_{at}\right)-C\left(T_0\right)\right\} \tag{3.37}$$

This differential signal is a relatively accurate and simple representation of the target's temperature referenced to an internal source. Its simplicity is owed to the calibration step that typically takes place prior to making temperature measurements of a sample. This step requires the user to enter the ambient temperature to compute $C\left(T_{at}\right)$ and $C\left(T_{sr}\right)$. Once this step is complete the measurement sequence is as follow:

- Enter emissivity of the target
- Measure ΔS

- Compute $C\left(T\right)$, a linear function of ΔS such that

  $$C\left(T\right)=\frac{\Delta S}{KeA_{at}}+\vartheta \tag{3.38}$$

  with ϑ is a constant offset calculated in the calibration step.

- Create a thermogram by inverting the function $C\left(T\right)$ with $T=C^{-1}\left(T\right)$ for each pixel

A typical digital imager is capable of completing this procedure at a rate greater than 30 $frames/second$ while high end systems are rated at more than 1000 $frames/second$. The following section gives an overview of the various infrared detectors and their principles of operation.

3.6.1 Infrared detectors

Infrared detectors are sensors capable of detecting heat radiation. They are classified into two major categories; thermal detectors and quantum detectors. Thermal type of detectors sense the heat generated by the incident radiation on its surface, hence they are independent of wavelength. Typically, thermal detectors are slow and do not require any cooling. Quantum detectors are photo sensors that can capture radiation in the infrared range, they are wavelength dependent, but have a considerably faster response [8].

The commonly used figures of merit for infrared detectors include their sensitivity or responsivity which is expressed in volts per watt (V/W) of incident radiation in photo-conductive detectors or amperes per watt (A/W) in photo-voltaic type of detectors, the detectability D^* defined as a measure of the signal to noise ratio (SNR) when the infrared radiation is equal to $1\,W$, and the noise equivalent power which measures the quantity of incident radiation in which its SNR is unity, the frequency response and the size/geometry of the active area which determines if the detector can be used as a single sensor, a linear array or a 2-D array.

Thermal detectors

Thermal detectors absorb the incident radiation which causes their temperature to increase affecting the basic properties of the material such as its electrical conductivity.

The sensitivity limit of thermal type of detectors is described by the effective conductivity

$$G_R = 4\sigma T^3 A \tag{3.39}$$

where $\sigma$is the Stefan-Boltzmann constant and A is the area of the detector. This measure leads to the second parameter, the detectivity limit

$$D = \sqrt{\frac{A}{4kT^2G}} \tag{3.40}$$

G is the limit of G_R, in general for most detectors $D \sim 10^7$to $10^9 cm\sqrt{Hz}/W$

The most commonly used thermal detectors are the bolometer, the pyroelectric detector and the thermopile.

Thermopiles Thermopiles are a series combination of thermocouples. Thermocouples are devices constructed with two junctions that connect two different metals. One of the junctions is maintained at constant temperature (usually cold), used as a reference, while the second acts as a measuring junction. In these devices, temperature changes result in a relatively small but measurable (in the milli-volt range) voltage difference between the terminals of the junctions. The series combination of multiple thermocouples causes a larger voltage difference which simplifies the measurement and improves the noise immunity. Thermopiles are not suited for the measurement of fast changing temperatures, their response time is limited by their own thermal mass. A typical thermopile can detect temperature modulated to $5\,Hz$[8].

Thermopiles output a voltage proportional to temperature which can be measured through a simple pre-amplifier similar to the one shown in Figure 3.7. Here the voltage output of the pre-amplifier is related to the voltage at the detector as follows:

$$V_{out} = \frac{R_1 + R_2}{R_1} \frac{R_3 + R_4}{R_3} V_{detector} \tag{3.41}$$

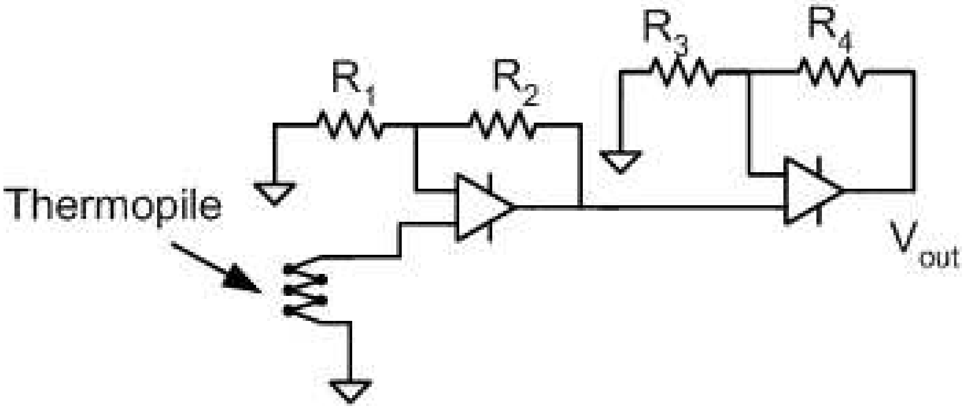

Figure 3.7: Dual stage pre-amplifier for thermopile detectors

Pyroelectric detectors Pyroelectric detectors are devices that possess the property of pyroelectricity of crystals where the electric polarity changes with temperature. The detector's crystal is fabricated as a thin wafer that is thermally insulated. When the face of the crystal is exposed to radiation its electric dipole moment configuration changes resulting in a voltage change which is subsequently measured utilizing a simple amplifier similar to the thermopiles, shown in Figure 3.7 or as used currently in the industry where it is integrated with a field effect transistor FET and a load resistor to provide pre-amplification and an additional shunt resistor to provide stability to the circuit as shown in Figure 3.8.

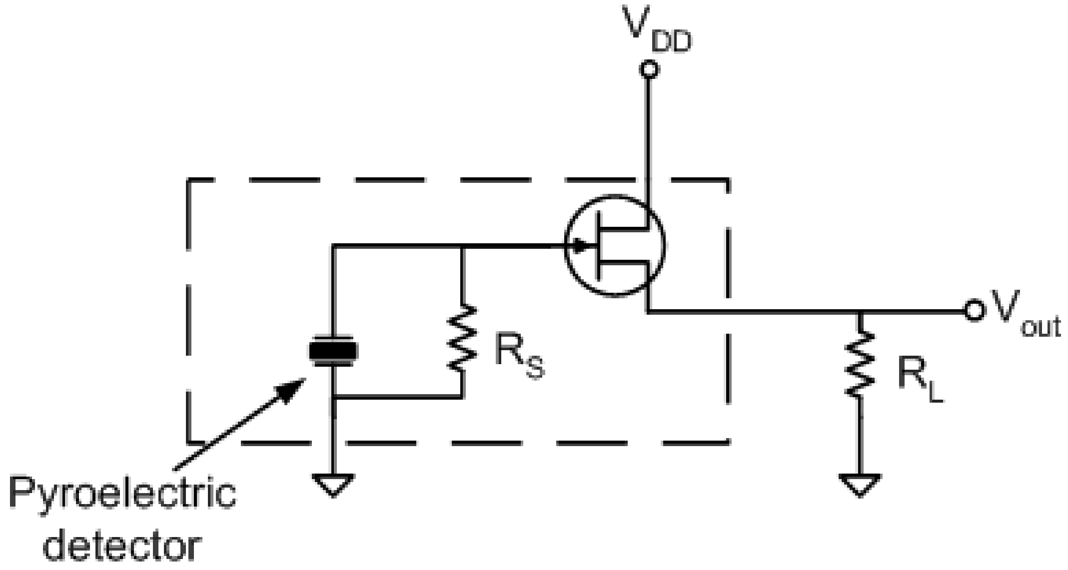

Figure 3.8: Pre-amplifier for a pyroelectric detector

Similar to thermopiles, pyroelectric detectors have a narrow frequency range limited to the band $0.01\ -0.1\,Hz$.

Bolometers The bolometer is a device that measures radiation over a wide range of wavelengths. It includes an absorber to capture the incident radiation connected to a heat sink held at a constant temperature through an insulating link. The relative temperature of the absorber is then measured through a thermometer to display the amount of radiation absorbed. Bolometers are very sensitive devices to all forms of energy. Therefore, it is required to add filter elements to allow transmission of only the wavelengths of interest.

There are several types of bolometers used in science and engineering such as the Cold-Electron bolometer used in particle physics. This device consists of a normal metal connected to a planar antenna through a superconductor-insulator-normal metal (SIN) tunnel junctions to become a very sensitive thermometer that can be used as X-ray or phonon detectors. Microbolometers are another type of these detectors and are used specifically to manufacture thermal cameras. They consist of a grid of

Vanadium Oxide heat sensor cells on a layer of Silicon substrate as shown in Figure 3.9.

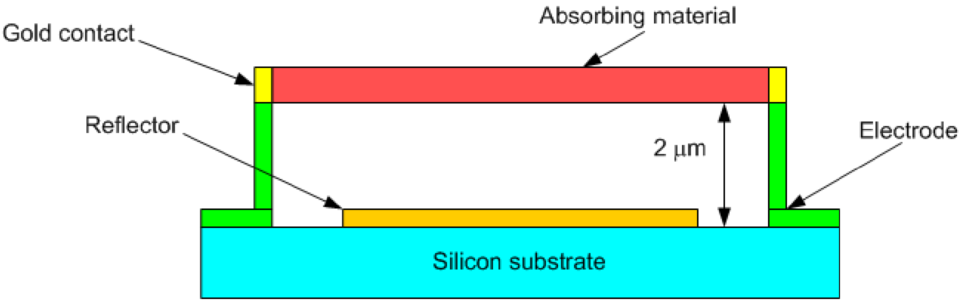

Figure 3.9: Cross-sectional view of a microbolometer

Uncooled microbolometers are opening new frontiers to infrared imaging as cameras constructed with such sensors do not require cooling, hence are more cost effective and highly portable. Such cameras share the advantages of the systems constructed using the photonic cooled detectors (which will be discussed in the subsequent section) with the added benefits of low cost and portability and extended field of view and resolution, cameras with grid sizes as high as 1024 X 768 pixels are commercially available.

Quantum detectors

A quantum detector is made of a semiconductor and the incident radiation excites electrons from the valence band to the conduction band. The band gap between the valance and conduction bands of a semiconductor has a well defined energy. Therefore, for a photon to be absorbed it must posses higher energy than that of the band gap. This translates into the requirement that only photons with wavelengths shorter than a critical value can be detected. This wavelength is defined in (3.42)

$$\lambda_c = \frac{hc}{E_g} = \frac{1.24}{E_g} \tag{3.42}$$

where $h = 6.626 \times 10^{-23}$ $[J\,s]$ is Planck's constant, $c = 3 \times 10^{10}$ $[cm.s]$ is the speed of light, and E_g is the band gap energy in $[eV]$.

In the medium wave infrared range (MWIR) and the long wave range (LWIR) the critical wavelength is relatively high $> 3\mu m$, the band gap energy is reduced which causes high sensitivity to noise and thermal agitation. These effects can cause the electrons to move to the conduction band. This major problem is overcome through adequate cooling which is accomplished using thermo-electric coolers (TECs) to $\sim 233\,^{\circ}K$ for MWIR detectors and using cryogenic cooling to $\sim 78\,^{\circ}K$ (liquid nitrogen) for LWIR.

Quantum detectors are classified into two categories; photo-conductors and photo-diodes.

Photoconductors

Photoconductors are made of semiconductors doped to have a finite conductivity. When exposed to incident light (in the infrared range), additional charges are generated in their conduction band. To establish conduction it is necessary to bias the detector to a fixed voltage such that the resistance of the detector and the bias voltage are related through Ohm's law

$$I = \frac{V_{bias}}{R_{detector}} \tag{3.43}$$

such that I is the current that flows through the detector, V_{bias} is the bias voltage, and $R_{detector}$ is the resistance of the detector.

The current that flows through the detector is measured using a simple voltage pre-amplifier (shown in Figure 3.10) or a transimpedance pre-amplifier.

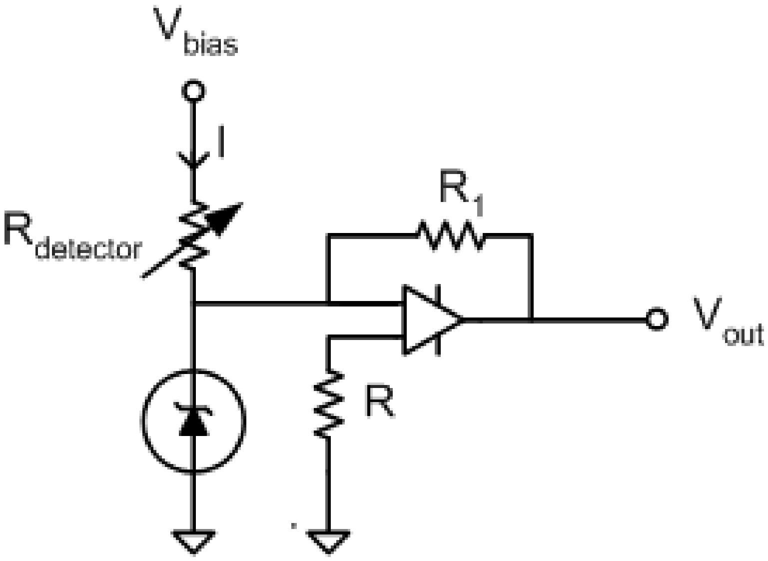

Figure 3.10: Pre-amplifier for photoconductor amplifiers

The main difficulty in this detection approach is the fact that the current that flows without the presence of any incident light, termed the dark current, is orders of magnitude larger than the current flow caused by the incident photons, therefore, more elaborate schemes have to be used in applications requiring high sensitivity.

Photodiodes Photodiodes are single crystal semiconductor detectors. They are very similar in behavior to regular diodes such that the voltage across them, and the current that flows through them, obeys the well known I-V curve. When the detector is exposed to radiation with wavelengths shorter than the critical wavelength, a potential is generated across the p-n junction thereby shifting the curve downward as shown in Figure 3.11.

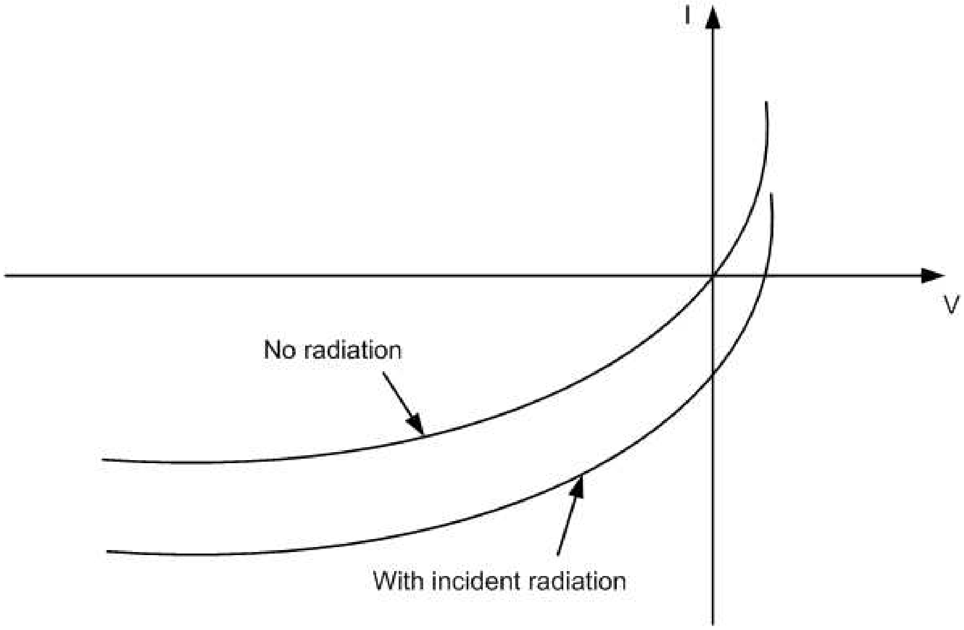

Figure 3.11: I-V curves for a photodiode with and without incident radiation

Photodiodes can be operated in short-circuit mode where a transimpedance preamplifier (shown in Figure 3.12) holds the bias close to zero. The resulting short circuit current becomes directly proportional to the irradiance or the amount of radiation incident on its active area as depicted in (3.44).

$$I = RA_{det}H \tag{3.44}$$

such that R is the detector responsivity, H is the irradiance and A_{det} is the active area of the detector.

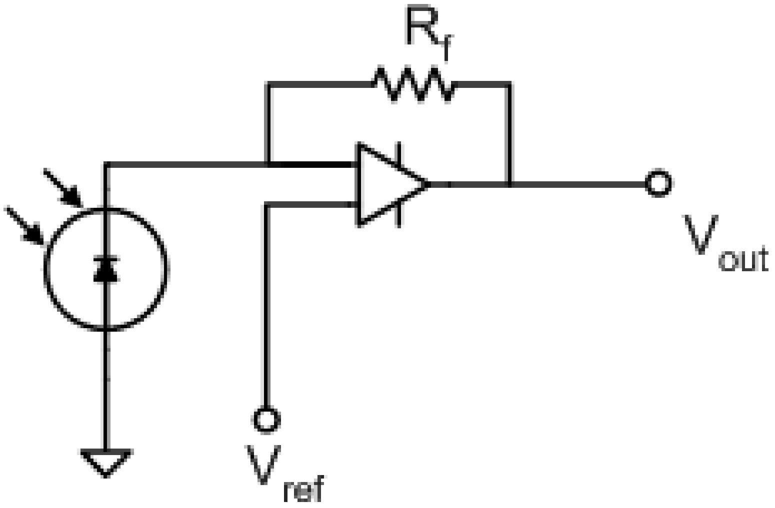

Figure 3.12: Transimpedance pre-amplifier for photodiodes

Similar to photoconductors, the main limitation in using photodiode detectors is noise in the MWIR range and LWIR where cooling is required to guarantee that thermal agitation does not result in electrons moving to the conduction band.

Cameras using photonic cooled detectors (quantum detectors) are very popular in non-destructive applications that require high sensitivity. This is due to the numerous advantages they have such as:

- High frequency response
- High spatial resolution (up to 640 X 512 pixels)
- Robust construction (solid state detectors)
- High frame rate (more than 250 frames per second)
- Low noise
- Digital interface (ease of implementation)

Despite all of these advantages the use of these cameras is still limited due to the high initial cost and the high ownership cost due to the cooling requirements.

Chapter 4

Analytical Formulation

4.1 Introduction

Thermal imaging involves the recording of the heat emanating from a part. These images are then interpreted to evaluate the integrity of the compacts and the presence/absence of flaws and defects. The interpretation of these images is based on a process of comparison between recordings taken from sound samples and others taken from the samples under test. Furthermore, a predictive model is used to establish the thermal profiles of the parts. Such model is numerical and evaluates qualitatively heat flow throughout the compact and through alien elements in it. The numerical model is constructed using a system of equations which are first solved analytically for canonical shapes and simple defect geometries. Such a model is used as a baseline to validate the numerical solutions and to establish the correct boundary conditions and initial values.

It is clear that due to the multi-physics nature of the problem, it is important to first establish the coupling parameters in the electro-thermal model, then, to simplify it so the focus will be the relevant elements such as the evolution of the surface temperature over time instead of voltage.

4.2 Voltage distribution

Electric energy is coupled into the P/M sample through surface contacts. This energy is in the form of direct current (DC), which will establish a voltage distribution throughout the part. The potential difference across the length of the part is equal to the work per unit electric charge required to move the charge through the length [18]. The relation illustrated in (4.1) is the basic idea underlying Joule's law :

$$\frac{Work}{Charge} * \frac{Charge}{Time} = \frac{Work}{Time} = Power \tag{4.1}$$

Equation (4.1) shows the power dissipated in the length of the conducting part.

Ohm's law, however, suggests that a constant of proportionality exists between the current injected I and the potential difference V across the length d of the sample. This constant is what is called resistance R, and it can be expressed as:

$$R = \frac{V}{I} = \frac{-\int \mathbf{E} \cdot d\mathbf{l}}{\int\int \mathbf{E} \cdot d\mathbf{S}} \tag{4.2}$$

or as commonly known:

$$V = I\mathrm{R} \tag{4.3}$$

Equations (4.1) and (4.2) imply that the power dissipated in the conductor can be written as:

$$P = VI = I^2\mathrm{R} \tag{4.4}$$

Applying a constant voltage to a P/M compact can be accomplished through inserting the latter between two large contacts as shown in Figure 4.1. The purpose of these large contacts is to reduce boundary effects due to charge build up and to ensure uniform current flow into the part.

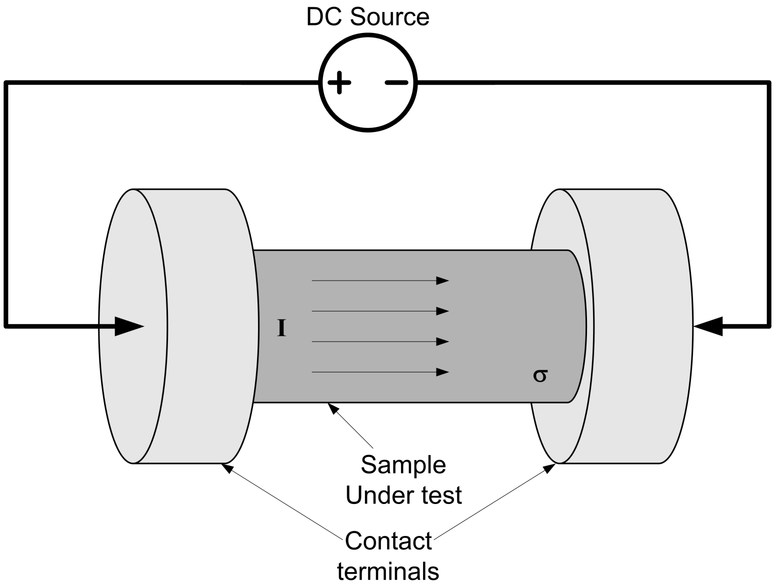

Figure 4.1: Cylindrical P/M part placed between end blocks.

Ohm's law in its current form represents a simplified view where it assumes uniform conductivity and a constant resistance. This simplified view can no longer hold when applied to parts such as green-state P/M compacts due to their amorphous nature and non-uniform density distribution. Also when detecting defects on the order of 20 μm, small voltage drops associated with the contact resistance can no longer be neglected.

The more generalized view takes into account the spatial dependency of the conductivity of the part and the voltage along its length. This approach uses Laplace's equation in the form:

$$\nabla \cdot (\sigma \nabla V) = 0 \tag{4.5}$$

Here $\sigma(x, y, z)$ is the electric conductivity of the medium and $V(x, y, z)$ is the voltage distribution in the sample.

This equation is a second order partial differential equation (PDE) that can be solved analytically for canonical geometries. A number of different solution methods have been developed, most notably the separation of variables, Fourier series, or Laplace transformation [19]. For simplicity, we chose the method of separation of variables in cylindrical coordinates.

In this system, where ρ, ϕ, and z are the independent variables, (4.5) can be cast as

$$\frac{\partial^2 V}{\partial \rho^2} + \frac{1}{\rho}\frac{\partial V}{\partial \rho} + \frac{1}{\rho^2}\frac{\partial V^2}{\partial \phi^2} + \frac{\partial^2 V}{\partial z^2} = 0 \tag{4.6}$$

The separation of variables technique suggests a solution of the form:

$$V(\rho, \phi, z) = \mathcal{R}(\rho)\, \Phi(\phi)\, Z(z) \tag{4.7}$$

When V is substituted in (4.6) , we obtain

$$\frac{Z\Phi}{\rho}\frac{d}{d\rho}\left(\rho\frac{d\mathcal{R}}{d\rho}\right) + \frac{\mathcal{R}Z}{\rho^2}\frac{d^2\Phi}{d\phi^2} + \mathcal{R}\Phi\frac{d^2 Z}{dz^2} = 0 \tag{4.8}$$

Dividing by $V = \mathcal{R}\Theta Z$ yields

$$\frac{1}{\mathcal{R}\rho}\frac{d}{d\rho}\left(r\frac{d\mathcal{R}}{dr}\right) + \frac{1}{\rho^2\Phi}\frac{d^2\Phi}{d\phi^2} + \frac{1}{Z}\frac{d^2 Z}{dz^2} = 0 \tag{4.9}$$

Equation (4.9) can be separated into two ordinary differential equations (ODEs):

$$\begin{cases} \dfrac{1}{Z}\dfrac{d^2 Z}{dz^2} = \gamma^2 \\ \\ \dfrac{1}{\mathcal{R}\rho}\dfrac{d}{d\rho}\left(\rho\dfrac{d\mathcal{R}}{d\rho}\right) + \dfrac{1}{\rho^2\Phi}\dfrac{d^2\Phi}{d\phi^2} = -\gamma^2 \end{cases} \tag{4.10}$$

The second term in (4.10) can also be separated into two separate ODEs , resulting in the following equations:

$$\frac{d^2 Z}{dz^2} + \gamma^2 Z = 0 \tag{4.11}$$

$$\frac{d^2\Phi}{d\phi^2} + \beta^2\Phi = 0 \tag{4.12}$$

$$\frac{d^2\mathcal{R}}{d\rho^2} + \frac{1}{\rho}\frac{d\mathcal{R}}{d\rho} + (\frac{\beta^2}{\rho^2} - \gamma^2)\mathcal{R} = 0 \tag{4.13}$$

Here γ and β are arbitrary separation constants.

The solution to (4.11) takes the form:

$$Z\left(z\right) = C_1 \cosh\left(\gamma z\right) + C_2 \sinh\left(\gamma z\right) \tag{4.14}$$

and similarly the solution to (4.12) is:

$$\Phi\left(\phi\right) = B_1 \cos\left(\beta\phi\right) + B_2 \sin\left(\beta\phi\right) \tag{4.15}$$

We observe that by introducing another variable α such that

$$\alpha^2 + \gamma^2 = 0 \tag{4.16}$$

equation (4.13) takes the form of a Bessel's equation. Its general solution is:

$$\mathcal{R}\left(\rho\right) = A_1 J_n\left(\alpha\rho\right) + A_2 Y_n\left(\alpha\rho\right) \tag{4.17}$$

where J_n is the Bessel function of the first kind of order n and Y_n is the nth-order Bessel function of the second kind .

In equations (4.14) - (4.17) A_1, A_2, B_1, B_2, C_1 and C_2 are integration constants.

The finale solution of Laplace's equation in cylindrical coordinates is therefore:

$$\begin{aligned} V\left(\rho,\phi,z\right) &= \left[C_1 \cosh\left(\gamma z\right) + C_2 \sinh\left(\gamma z\right)\right]\left[B_1 \cos\left(\beta\phi\right) + B_2 \sin\left(\beta\phi\right)\right] \\ &\cdot \left[A_1 J_n\left(\alpha\rho\right) + A_2 Y_n\left(\alpha\rho\right)\right] \end{aligned} \tag{4.18}$$

If one considers the solid cylinder illustrated in Figure 4.1 with a uniform density, (4.18) can be substantially simplified.

Specifically, the electric potential will be independent of ϕ due to symmetry. The solution of (4.6) takes on the form

$$V(\rho, z) = [A\cosh(\gamma z) + B\sinh(\gamma z)]\, J_0(\alpha r) \tag{4.19}$$

The associated boundary conditions involve the inward pointing surface normal $\mathbf{n}$ and the current density $\mathbf{J}$. This allows us to specify the electric flux

$$\mathbf{n} \cdot (\sigma \nabla V) = -\mathbf{n} \cdot \mathbf{J} \tag{4.20}$$

All remaining boundaries, excluding the ground connection, are set to be insulating or flux free

$$\mathbf{n} \cdot \mathbf{J} = 0 \tag{4.21}$$

The imposed boundary conditions yield a special case of the Sturm-Louisville system, with eigenfunctions of the form

$$V(\rho, z) = \sum_{n=1}^{\infty} A_n J_0(\gamma_n \rho) \sinh(\gamma_n z) \tag{4.22}$$

Here γ_n's are the positive roots of the Bessel function of the zeroth order

$$J_0(\gamma_n R) = 0, \quad n = 1,\, 2,\, 3, \ldots. \tag{4.23}$$

Now we need to determine the coefficients A_n in (4.22) in such away that $V(\rho, L) = f(\rho)$. Here $f(\rho)$ is an arbitrary function of ρ that can be expanded so as to satisfy the boundary condition.

We make use the orthogonality of Bessel functions to write a Fourier-Bessel expansion of $f(\rho)$ over the interval $(0, R)$at $z = L$.

$$f\left(\rho\right) = \sum_{n=1}^{\infty} A_n \sinh\left(\gamma_n L\right) J_0\left(\gamma_n \rho\right) \tag{4.24}$$

The coefficients A_n may readily be obtained as

$$A_n = \frac{\displaystyle\int_0^R f\left(\rho\right) J_0\left(\gamma_n \rho\right) \rho d\rho}{\displaystyle\int_0^R J_0^2\left(\gamma_n \rho\right) \rho d\rho} \tag{4.25}$$

Using the identity

$$\frac{d}{d\rho}\left[\rho J_1\left(\gamma_n \rho\right)\right] = \gamma_n \rho J_0\left(\gamma_n \rho\right) \tag{4.26}$$

Integrating both sides will result in

$$\int_0^R J_0\left(\gamma_n \rho\right) \rho d\rho = \frac{R}{\gamma_n} J_1\left(\gamma_n R\right) \tag{4.27}$$

Therefore the formulation can be simplified to

$$A_n = \frac{2}{R^2 J_1^2\left(\gamma_n R\right)} \int_0^R f\left(\rho\right) J_0\left(\gamma_n \rho\right) \rho d\rho \tag{4.28}$$

For this particular case, $f(\rho) = V_0$ is a constant. The solution becomes

$$V\left(\rho, z\right) = \frac{2V_0}{R} \sum_{n=1}^{\infty} \frac{J_0\left(\gamma_n \rho\right) \sinh\left(\gamma_n z\right)}{\gamma_n J_1\left(\gamma_n R\right) \sinh\left(\gamma_n L\right)} \tag{4.29}$$

A solution is plotted in Figure (4.2) , involving the parameters $R = 0.01m$ and L for different aspect ratios.

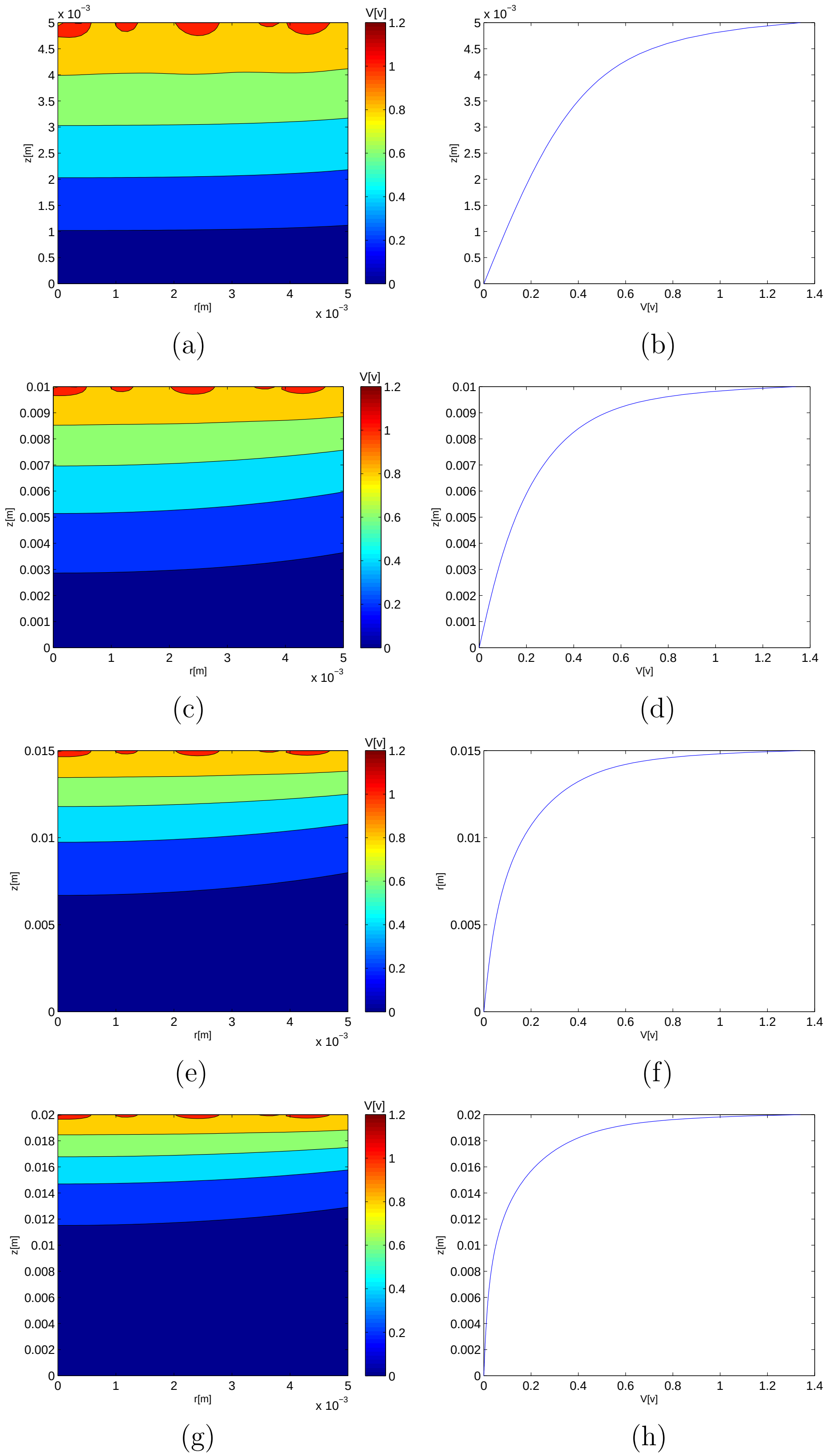

Figure 4.2: Voltage distribution in a cylindrical compact for various values of $\frac{R}{L}$ and the resulting surface voltage (a) and (b) $\frac{R}{L} = 1$, (c) and (d)$\frac{R}{L} = \frac{1}{2}$, (e) and (f) $\frac{R}{L} = \frac{1}{3}$, (g) and (h) $\frac{R}{L} = \frac{1}{4}$.

The electric current flowing through the compact will create a voltage distribution and deposit power (Joule heating) due to the finite conductivity in the sample. The power per unit volume Q is described by

$$Q = \frac{J^2}{\sigma} = \sigma E^2 = \sigma \left|\nabla V\right|^2 \tag{4.30}$$

where E is magnitude of the electric field.

The deposited electrostatic power will cause the temperature of the part to rise gradually until it reaches equilibrium (known as the Joule effect). This process is influenced by the thermal properties of the part and the atmospheric conditions (ambient temperature).

4.2.1 Electrostatic flaw representation

To provide insight into the voltage-defect interaction inside a P/M compact we can conduct a simple analytical study. To a first approximation we can represent the flaw as a sphere with different conductivity and dielectric properties $(\sigma_d, \varepsilon_d)$ from the bulk properties of the P/M compact $(\sigma_s, \varepsilon_s)$. The applied voltage excitation via the electrodes establishes an electric field $E\left(t\right)$ throughout the compact which is assumed uniform in the absence of the spherical defect, resulting in a linear voltage distribution. If a spherical defect of size R_d is embedded into the samples, both the electric field and potential distribution are perturbed [20].

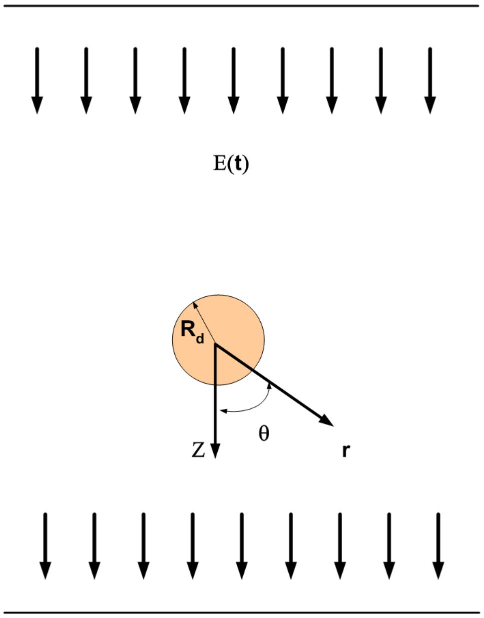

Figure 4.3: Spherical defect in a uniform time varying electric field.

According to classical potential theory, Laplace's equation in spherical coordinates outside the sphere assumes the classical dipole voltage written as

$$V = \begin{cases} -E\left(t\right)\ r\ \cos\theta + A\left(t\right)\frac{\cos\theta}{r^2} & r > R_d \\ \\ B\left(t\right)\ r\ \cos\theta & r < R_d \end{cases} \tag{4.31}$$

Here $A\left(t\right)$ and $B\left(t\right)$ are time dependent coefficients that can be determined by solving a boundary value problem under the assumption that the imposed electric field is switched on via a step function ($h(t) = 1$, if $t \geq 0$, and 0 if $t < 0$), i.e. $E\left(t\right) = E_0 h\left(t\right)$.

Continuity on the surface of the spherical defect (first continuity condition) imposes

$$-E\left(t\right)\ R_d\ \cos\theta + A\left(t\right)\frac{\cos\theta}{R_d^2} = B\left(t\right)\ R_d\ \cos\theta \tag{4.32}$$

Solving for $B(t)$

$$B\left(t\right) = -E\left(t\right) + \frac{A\left(t\right)}{R_d^3} \tag{4.33}$$

The conservation of charge (second continuity condition) is represented by Gauss's law where

$$\mathbf{n}\,\boldsymbol{.}\,(\sigma_s\mathbf{E_s} - \sigma_d\mathbf{E_d}) + \frac{\partial}{\partial t}\mathbf{n}\,\boldsymbol{.}\,(\epsilon_s\mathbf{E_s} - \epsilon_d\mathbf{E_d}) = 0 \tag{4.34}$$

Substituting in (4.31) and setting the field to the initial condition we find $A = A\,(0)$

$$A = E_0R_d^3\left[\frac{\sigma_s - \sigma_d}{2\sigma_s + \sigma_d}\left(1 - e^{-t/\tau}\right) + \frac{\varepsilon_s - \varepsilon_d}{2\varepsilon_s + \varepsilon_d}e^{-t/\tau}\right] \tag{4.35}$$

hence the final solution takes the form

$$V = -E_0R_d\,\cos\theta\begin{cases} \frac{r}{R_d} + \left[\frac{\sigma_s - \sigma_d}{2\sigma_s + \sigma_d}\left(1 - e^{-t/\tau}\right) + \frac{\varepsilon_s - \varepsilon_d}{2\varepsilon_s + \varepsilon_d}e^{-t/\tau}\right]\frac{R_d^2}{r^2} & r > R_d \\ \\ \frac{r}{R_d}\left[1 + \frac{\sigma_s - \sigma_d}{2\sigma_s + \sigma_d}\left(1 - e^{-t/\tau}\right) + \frac{\varepsilon_s - \varepsilon_d}{2\varepsilon_s + \varepsilon_d}e^{-t/\tau}\right] & r < R_d \end{cases} \tag{4.36}$$

As stated above, ε_s and σ_s are the permittivity and the conductivity of the sample and ε_d and σ_d are the permittivity and the conductivity of the spherical defect. Here the relaxation time τ in (4.36) is defined as

$$\tau = \frac{2\varepsilon_s + \varepsilon_d}{2\sigma_s + \sigma_d} \tag{4.37}$$

In general, (4.37) suggests for P/M compacts ($\varepsilon_{s,d} \approx 10^{-12}$, $\sigma_{s,d} \approx 10^3$) that the relaxation time is negligibly small ($\tau \approx 10^{-15}\,sec.$); thus the exponential term in (4.35) can be discarded. Thus, (4.31) further simplifies to

$$V = \begin{cases} -E_0r\,\cos\theta - E_0\,\frac{R_d^3}{r^2}\,\cos\theta\left[\frac{\sigma_s - \sigma_d}{2\sigma_s + \sigma_d}\right] & r > R_d \\ \\ -E_0r\,\cos\theta\left[1 + \frac{\sigma_s - \sigma_d}{2\sigma_s + \sigma_d}\right] & r < R_d \end{cases} \tag{4.38}$$

Here, $E_0 = \frac{V_0}{L}$ is based on the 1-D capacitor model with the voltage measured at the electrodes over the length of the sample L.

From (4.38) it is clear that the uniform field is represented by the term $(E_0 r \cos\theta)$.

Thus far the defect representation has been performed in the spherical coordinate system with the origin being the center of the defect. To combine (4.29) and (4.38), an origin translation is required along with a coordinate system transformation. Initially, an origin translation is performed taking into consideration the parameters shown in Figure 4.4

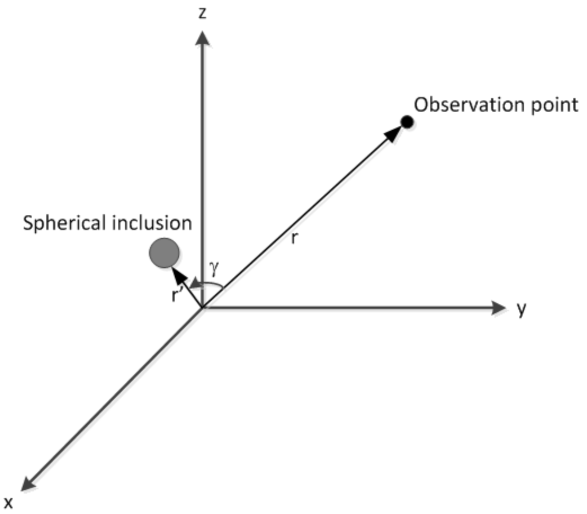

Figure 4.4: Defect located away from the coordinate system origin as observed from a distance r.

where distance between the observation point and the location of the defect ζ can be written as

$$\zeta = \sqrt{r^2 + r'^2 - 2\,r\,r'\,\cos\gamma} \tag{4.39}$$

using the spherical law of cosines we find the relationship between the azimuthal angles as follow

$$\cos\gamma = \cos\theta\,\cos\theta' + \sin\theta\,\sin\theta'\,\cos(\phi - \phi') \tag{4.40}$$

For simplicity a solution that is independent of ϕ is considered such that $\phi = \phi'$, therefore, (4.40) becomes

$$\cos\gamma = \cos(\theta - \theta') \tag{4.41}$$

Thereafter, a spherical to cylindrical coordinate system transformation is performed using the formula

$$\begin{cases} \rho = r\,\sin\theta \\ \phi = \phi \\ z = r\,\cos\theta \end{cases} \tag{4.42}$$

The final solution becomes

$$V = \begin{cases} -E_0 z\left[1 + \dfrac{\sigma_s - \sigma_d}{2\sigma_s + \sigma_d}\,\dfrac{R_d^3}{\rho_0^3}\right] & \rho_0 > R_d \\[2ex] -E_0 z\left[1 + \dfrac{\sigma_s - \sigma_d}{2\sigma_s + \sigma_d}\right] & \rho_0 < R_d \end{cases} \tag{4.43}$$

with $\rho_0 = \sqrt{\rho^2 + \rho'^2 - 2\,\rho\rho' \arctan\left[(\rho - \rho')\,/\,(z - z')\right]}$

ρ' and z' represent the location of the inclusion.

This simple 2-D solution is a first order verification tool for the voltage distribution in a P/M part. The general solution is plotted for different flaw sizes and locations in Figure 4.5.

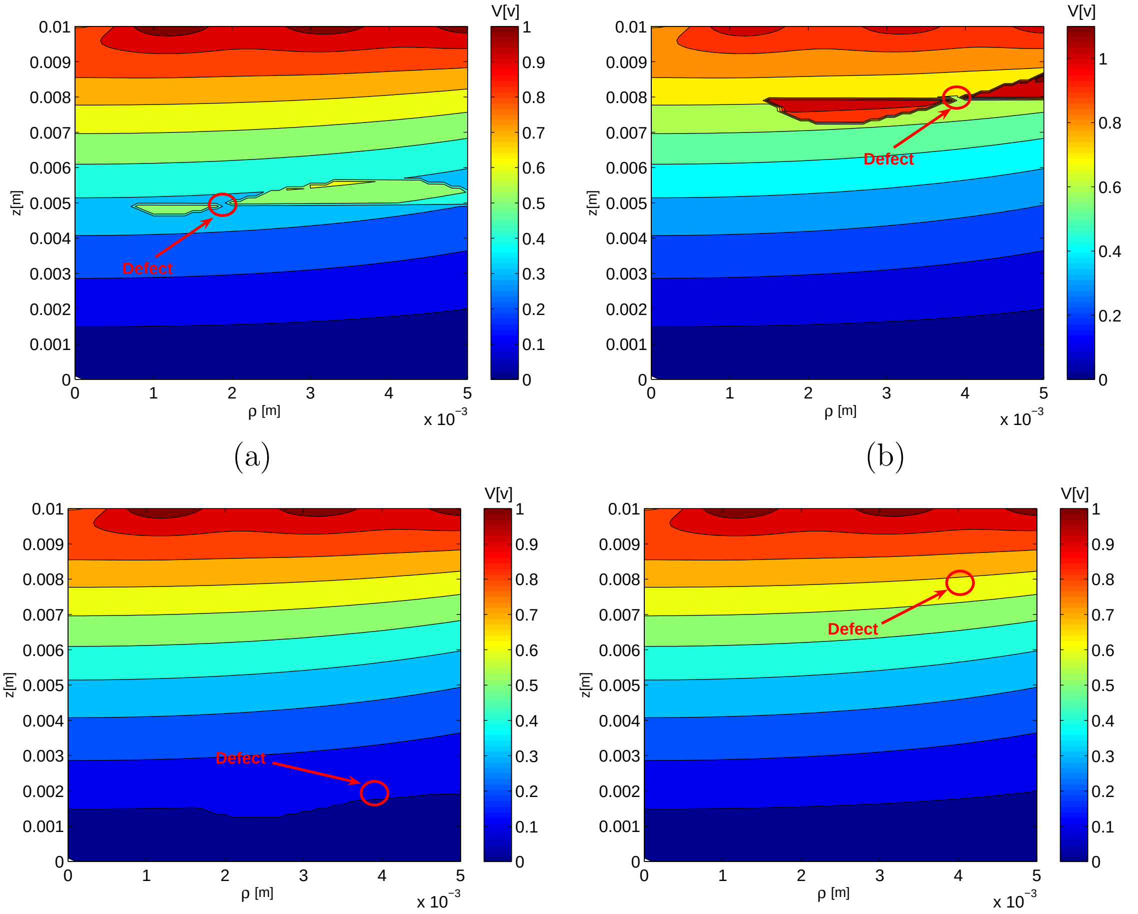

(a) (b)

(c) (d)

Figure 4.5: (a) Voltage distribution in a defective cylindrical compact with $\sigma_s = 10^3$, $\sigma_d = 1$, $R_d = 0.1mm$, $\rho' = 4mm$, and $z' = 5mm$ (b) $R_d = 0.1mm$, $\rho' = 4mm$, and $z' = 8mm$(c) $R_d = 0.1mm$, $\rho' = 4mm$, and $z' = 2mm$ (d) $R_d = 0.1mm$, $\rho' = 4mm$, $z' = 8mm$, and $\sigma_s = \sigma_d = 10^3$.

The electrostatic flaw representation highlights the fact that the voltage disturbance due to a defect in the part such as a crack or an inclusion is limited to large cracks and surface breaking defects. Moreover, due to the conductivities of the bulk material and the defect time become a very insignificant factor as described by the relaxation time which as shown is infinitesimally small.

4.3 Temperature profile

In general, the thermal behavior of a body is described by the generalized heat equation

$$\varrho c \frac{\partial T}{\partial t} - \nabla \cdot (k \nabla T) = Q - h\left(T - T_{ext}\right) - C\left(T^4 - T_{amb}^4\right) \tag{4.44}$$

Here T, T_{ext} and T_{amb} are sample, external and ambient temperatures respectively. k is the thermal conductivity in $W/m{}^\circ C$, ϱ is the density of the material in kg/m^3, c is the heat capacity in $W/kg{}^\circ C$, Q is the heating power in W/m^3, h is the average convective heat transfer coefficient in $W/m^2{}^\circ C$, and C is the radiative heat transfer coefficient in $W/m^2{}^\circ C^4$.

The dominant transfer mechanism in our proposed testing technique is heat conduction. We therefore obtain the simplified expression, illustrated in (4.46). This equation is a second order PDE that can be solved following the same steps described to solve Laplace's equation. In this formulation it is assumed that the sample surface is cooled through natural convection, implying a Neumann type boundary condition

$$\mathbf{n} \cdot (k \nabla T) = h\left(T_{ext} - T\right) \tag{4.45}$$

Therefore, in the cylindrical coordinate system we will write the axis-symmetric relation

$$\frac{k}{\rho} \frac{\partial}{\partial \rho}\left(\rho \frac{\partial T}{\partial \rho}\right) + \frac{\partial^2 T}{\partial z^2} = \varrho c \frac{\partial T}{\partial t} - Q \tag{4.46}$$

where the temperature and the power deposited are function of only ρ, z and t .

Under steady state condition (4.46) simplifies to

$$\frac{k}{\rho} \frac{\partial}{\partial \rho}\left(\rho \frac{\partial T}{\partial \rho}\right) + \frac{\partial^2 T}{\partial z^2} = -Q \tag{4.47}$$

Here is a base temperature specified as a function of radius and the boundary conditions at $\rho = R$

$$k\frac{\partial T\left(R,z\right)}{\partial \rho} + hT\left(R,z\right) = 0 \tag{4.48}$$

$$k\frac{\partial T\left(\rho,L\right)}{\partial \rho} + hT\left(\rho,L\right) = 0 \tag{4.49}$$

$$k\frac{\partial T\left(\rho,0\right)}{\partial \rho} + hT\left(\rho,0\right) = 0 \tag{4.50}$$

The axis-symmetric solution can be developed in an orthogonal series expansion of the form

$$T\left(\rho,z\right) = \frac{2QhR^3}{k}\sum_{n=1}^{\infty}\frac{1-\dfrac{\left(hR/\gamma_n\right)\cosh\left(\gamma_n z/R\right)}{\left[\tan\left(\mathrm{\gamma_n L/R}\right)+\mathrm{hR/\gamma_n}\right]+\cosh\left(\mathrm{\gamma_n L/R}\right)}}{\left[1+\left(hR/\gamma_n\right)^2\right]\gamma_n^4 J_0\left(\gamma_n\right)}J_0\left(\frac{\gamma_n\rho}{R}\right) \tag{4.51}$$

In (4.51) γ_n are the positive roots of the transcendental equation:

$$\gamma J_1\left(\gamma_n\right) = RhJ_0\left(\gamma_n\right) \tag{4.52}$$

An example solution was computed for the following numerical parameters representing a green-state P/M compact:

- Radius: $R = 0.01\,m$
- Length: $2L = 0.06\,m$
- Heating Power: $Q = 767\,kW/m^3$
- Thermal conductivity: $k = 25\,W/m\ ^\circ C$
- Convection heat transfer coefficient: $h = 10\,W/m^2\ ^\circ C$

Figure 4.6 illustrates the temperature distribution throughout the compact. As expected, the temperature is at a maximum at $r = z = 0$ and begins to decay to a minimum value at the surface due to the convective boundary.

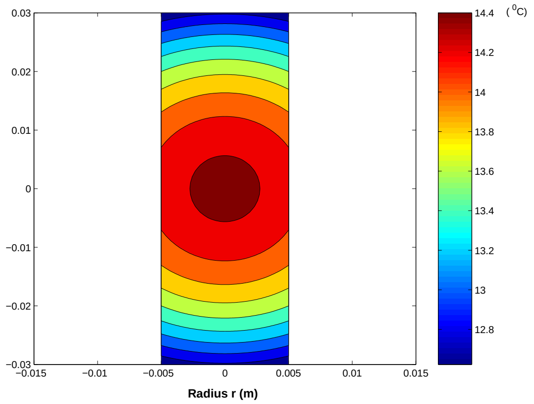

Figure 4.6: Temperature distribution for a cylindrical compact. Dimensions are recorded in m.

A time varying solution in ρ and t with the initial condition

$$T(\rho, 0) = T(\rho) - T_0 \tag{4.53}$$

can be derived as follow

$$T(\rho, t) = \frac{2QhR^2}{k}\left[\frac{1}{8}\left(1 - \frac{\rho^2}{R^2}\right) + \frac{1}{4Rh} - Rh\sum_{n=1}^{\infty}\frac{e^{-\gamma^2\tau/R^2} J_0\left(\frac{\gamma_n\rho}{R}\right)}{\left[1 + (hR/\gamma_n)^2\right]\gamma_n^4 J_0(\gamma_n)}\right] \tag{4.54}$$

where

$$\tau = \frac{kt}{\varrho c} \tag{4.55}$$

The solutions (4.51) and (4.54) can be used as benchmarks to verify both the modeling and the experimental results.

4.3.1 Flaw representation: Green's function solution

In the previous section we described the general solution and the basic approach to determine the temperature rise in a P/M sample due to electric heating. The technique we used is a straight forward expansion into eigenfunctions. This method can also be used to evaluate the effect of a source or sink such as an internal defect.

The draw back however is that the solution will be an infinite series which converges in a slow manner, hence, to capture the effects due to a small defect (source) will be computationally cumbersome. It is, therefore, preferable to find a closed form solution which can easily be achieved through the use of the so called Green's functions. The idea behind this method is to solve the problem for a point source which is represented mathematically by a delta function $\delta(\mathbf{r}-\mathbf{r_0})$, then integrate the impulse response (Green's function) over the range of the source/sink to find the total solution [21].

The diffusion equation is modified to include the impulsive point source and is satisfied by Green's function G

$$\nabla^2 G - \kappa^2 \left(\frac{\partial G}{\partial t}\right) = -4\pi\delta\left(\mathbf{r}-\mathbf{r}_0\right)\,\delta\left(t-t_0\right) \tag{4.56}$$

Here, we have introduced a point source at location $\mathbf{r}_0$ and at time t_0 with unit strength. κ is the thermal diffusivity, t is the time and $\mathbf{r}$ is the observation location.

The final solution is then obtained by integrating the Green's function solution over the range of the source, thus making the general solution of the form:

$$T\left(r,t\right) = \iint q(r_0,t_0) G\left(r,r_0,t,t_0\right) dV_0 dt_0 \tag{4.57}$$

where $q\left(r,t\right)$ is the source term.

Many methods have been devised to obtain the Green's function for a particular problem such as the method of images. This technique is well known in electrostatics where for any charge in space a fictitious image charge (a charge of equal potential but opposite sign) is introduced such that the total charge on the surface of interest is zero [21] as represented in the Figure 4.7

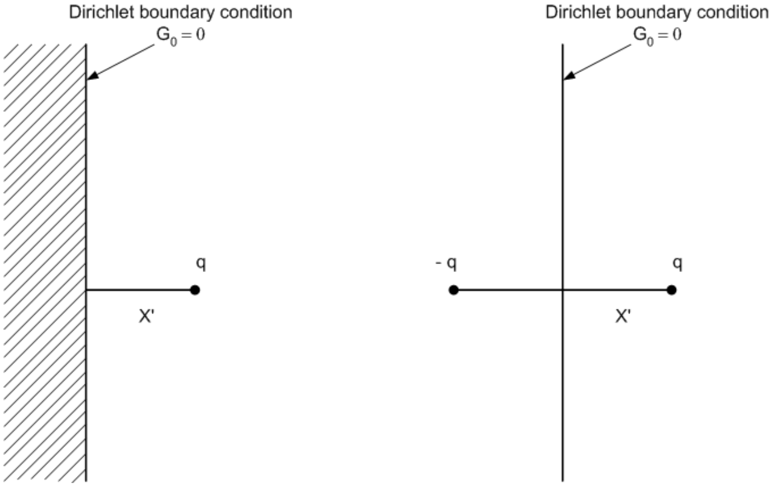

Figure 4.7: The method of images for a half-space with Dirichlet conditions.

If we consider the case of a half space with Neumann conditions shown in Figure 4.8. The source and the image are paired at the observation boundary and they are combined to maintain a flux-free condition.

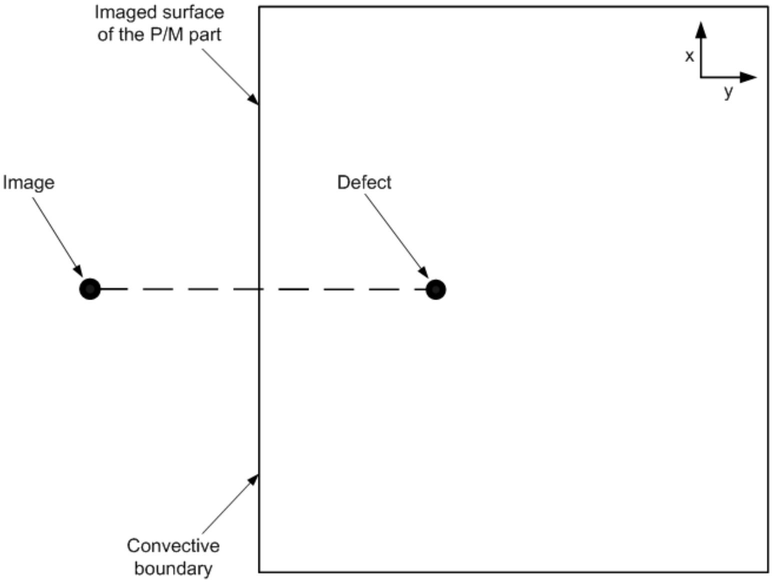

Figure 4.8: Idealized sub-surface defect representation as an embedded point source.

Since $\frac{\partial G}{\partial n} |_{x=0} = q$ with q is the constant charge at the surface (boundary) $x = 0$ the

Green's function is expressed as

$$G\left(r,r_0,t,t_0\right)=g\left(r,r_0,t,t_0\right)+g\left(r,r_1,t,t_0\right) \tag{4.58}$$

for the example depicted by Figure 4.8 where the point source located at (x_0,y_0). In the Cartesian coordinate system, (4.58) becomes

$$G\left(r,r_0,t,t_0\right)=g\left(x,y,x_0,y_0,t,t_0\right)+g\left(x,y,-x_0,y_0,t,t_0\right) \tag{4.59}$$

Equation (4.56) therefore becomes

$$\frac{\partial^2 g}{\partial x^2}+\frac{\partial^2 g}{\partial y^2}-\kappa^2\left(\frac{\partial g}{\partial t}\right)=-4\pi\delta\left(\mathbf{r}-\mathbf{r}_0\right)\delta\left(t-t_0\right) \tag{4.60}$$

By using $R=\sqrt{\left(x-x_0\right)^2+\left(y-y_0\right)^2}$ and employing the method of separation of variables described in the previous section, we obtain

$$g\left(x,y,x_0,y_0,t,t_0\right)=\frac{e^{\frac{R^2}{\sqrt{4\pi(t-t_0)}}}}{4R\sqrt{\left[\kappa\left(t-t_0\right)\right]^3}}h\left(t-t_0\right) \tag{4.61}$$

where

$$h(t-t_0)=\begin{cases}0,\ for & t<t_0\\ 1,\ for & t\geq t_0\end{cases} \tag{4.62}$$

The corresponding total thermal impulse response, or the Green's function solution for a semi-infinite space bound by flux-free boundaries at any point in space becomes

$$G\left(x,y,x_0,y_0,t,t_0\right)=\frac{h\left(t-t_0\right)}{\sqrt{\left[\kappa\left(t-t_0\right)\right]^3}}\left[\frac{e^{\frac{\left(x-x_0\right)^2+\left(y-y_0\right)^2}{\sqrt{4\pi(t-t_0)}}}}{\sqrt{\left(x-x_0\right)^2+\left(y-y_0\right)^2}}+\frac{e^{\frac{\left(x-x_0\right)^2+\left(y+y_0\right)^2}{\sqrt{4\pi(t-t_0)}}}}{\sqrt{\left(x-x_0\right)^2+\left(y+y_0\right)^2}}\right] \tag{4.63}$$

Here (x,y) indicates a point in the simulated half-space and (x_0,y_0) denote the defect coordinates. The Green's function represented in (4.63) is an approximation to the final solution which is the integration

$$T\left(x,y,t\right)=\int_{0}^{t}\int_{-\infty}^{+\infty}\int_{-\infty}^{+\infty}q(x_0,y_0,t_0)G\left(x,y,x_0,,y_0,t,t_0\right)dx_0dy_0dt_0 \qquad (4.64)$$

Depicted in Figure 4.9 is the impulsive temperature increase (G) over time and spatial (x-direction) extent as recorded over the surface of a half-space ($y = 0$) for the following parameters: surface length recording: 10cm, defect location: $(x_0, y_0) = (5cm, 5cm)$, and heating power: $Q = 8\,W$.

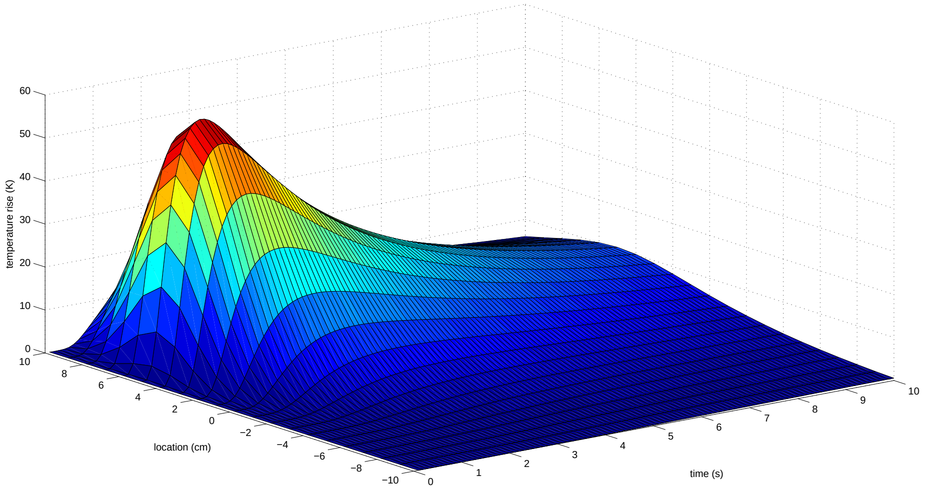

Figure 4.9: Temperature rise recorded over the compact surface due to an embedded heat source.

In this chapter we have described the basic steps that lead for the evaluation of the electrostatic and thermal behavior of a P/M part when heated through Joule heating. Furthermore, we have developed a more comprehensive model that takes into consideration the presence of a defect and its interactions with the bulk of the material. Although the technique is straightforward it requires complicated calculations and the computations that become cumbersome. Moreover, we have only considered canonical geometries such as a cylinder and a slab, in industrial applications we find complex geometries such as gears and other multilevel parts with defect geometries that are very irregular. Such practical considerations lead to the use of numerical methods which with today's computing power are fast and accurate. However, analytical methods remain important to calibrate numerical models.

Chapter 5

Numerical Formulation

5.1 Introduction

The thermo-electric problem is complex by nature as it is governed by inhomogeneous partial differential equations. Furthermore, practical considerations involve highly irregular shapes and complicated geometries with corners, sharp teeth and holes. Consequently, the only reasonable approach to predict the thermal response (therefore, the irradiance) of a part heated electrically through direct or alternative current is numerical. A review of the available methods suggests that the finite elements method is the most adequate as it does not suffer from convergence limitations.

In this chapter we describe the finite elements method and we apply it through the utilization of a commercial software package (Comsol) to solve a series of example problems for all of the embodiments of the technique listed in Chapter 1. First, a thermoelectric model is constructed to predict the thermal response of a part subjected to a DC current. Second, a more comprehensive model is presented to verify detection limits and the sensitivity of the method. Third, an induction heating model shows the possibility of utilizing a contact-less energy deposition. Last, a combined fluid flow-heat transfer model that captures the behavior of parts as they move on the belt and are cooled convectively, this encompasses aspects of on-line testing where the residual heating from the press system is the initial condition and a velocity term is added to capture motion and cooling effects.

5.2 Finite Elements Method

The finite elements method (FEM) is a numerical technique for approximating solutions to boundary-value problems in science and engineering. Typical mathematical physics areas where this technique is widely used include structural analysis, heat and mass transfer, fluid flow, and electromagnetics. The method is used as a tool for the discretization and modeling of arbitrary shaped domains and heterogeneous medium composition. It was first proposed in the 1940s in the area of structural engineering, but its use did not gain popularity until the advent of high speed computing due the fact that the resulting equations become too cumbersome to solve analytically [22].

The principle of the finite elements method is to replace a continuous domain Ω by a number of arbitrarily shaped sub-domains in which the unknown function is represented by simple interpolation functions with unknown coefficients. The following sections will discuss the basic steps in the finite elements representation. A qualitative illustration is based on solving Laplace's equation in a 2D domain.

5.2.1 Mesh Generation

The geometry is subdivided into smaller units called elements, an operation which is called discretization or meshing. Due to its importance in the FEM, mesh generation has been the focus of extensive research, and a number of algorithms have been developed [22, 23]. Thereby, allowing scientists and engineers to focus on the application at hand. With the increasing processing power came the ability to deploy a larger number of sub-domains as well as the accessibility to each element. Whereby, material properties are assigned at the element level.

As defined above, a mesh is a finite set of elements that can be segments (lines) in 1D, triangles (shown in Figure 5.1) or quadrilaterals in 2D, or tetrahedras, pentahedras or hexahedras in 3D [24].

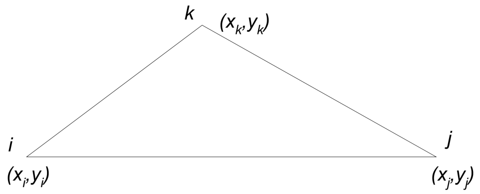

Figure 5.1: Basic triangular element and its nodal representation.

Figure 5.1 makes clear that an element is a specified by its corner points (*i*,*j*,*k*),and the associated coordinates in the (x,y) plane. Aim of a good mesh generation strategy is to deploy elements with equal aspect ratios with sufficiently small resolution to limit the errors to the pre-defined tolerances. The nature of discretizing small defects when utilizing uniform meshing requires extensive computational resources, which may not be available if the mesh is too refined. A remedy to this shortcoming is the use of adaptive meshing, as proposed by Berger and Oliger[24]. Whereby, finer grids are adaptively placed over the coarse mesh in the sub-regions that require higher resolution.

5.2.2 Interpolation Function and System of Equations

The discretization of the solution domain will allow the representation of the governing equation by approximation or basis functions. The set of interpolation functions are chosen to be computationally efficient. Usually a set of polynomials of first or second order are selected.

For the 2D element shown in Figure 5.1 the approximation or interpolation function is written

$$N_i\left(x,y\right) = \alpha_i + \beta_i x + \gamma_i y \tag{5.1}$$

where α_i, β_i and γ_i are constant coefficients that can be determined using the following property of the interpolation function

$$\begin{cases} N_i = 1, \; for \; (x,y) = (x_i, y_i) \\ N_i = 0, \qquad Otherwise \end{cases} \tag{5.2}$$

This will result in a local matrix equation for its constant coefficients

$$\begin{bmatrix} 1 & x_i & y_i \\ 1 & x_j & y_j \\ 1 & x_k & y_k \end{bmatrix} \begin{Bmatrix} \alpha_i \\ \beta_i \\ \gamma_i \end{Bmatrix} = \begin{Bmatrix} 1 \\ 0 \\ 0 \end{Bmatrix} \tag{5.3}$$

The solution to (5.3) shows that the coefficients depend on the area of the element (triangle in this case) and the coordinates of its nodes. Figure 5.2 depicts the interpolation function in a triangular element.

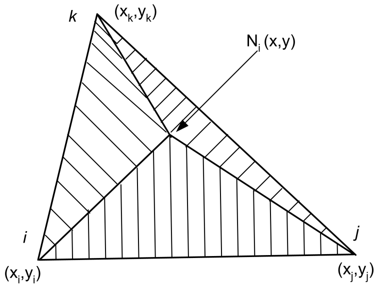

Figure 5.2: Interpolation function in the 2D FEM

We can now list the fundamental steps for solving Laplace's equation

$$\nabla^2 V = 0 \tag{5.4}$$

The basic idea is to first approximate the independent variable with a trial function

$$V \approx \hat{V} = \sum_{j=1}^{L} V_j N_j \tag{5.5}$$

Where j is the node number, L is the total number of nodes, V_j are constant coefficients for the set of equations representing the solution, and N_j are the basis functions.

The substitution of V by the trial function will result in a residual term

$$\nabla^2 \hat{V} = R \tag{5.6}$$

The best approximation for V is the one that minimizes the residual in the domain Ω. This is accomplished through forcing the residual to zero. Multiplying by a weight function as described by the weighted residual method results in

$$\int_{\Omega} WR = 0 \tag{5.7}$$

Here W is a chosen weighting function, over the domain Ω such that

$$W = \sum_{i=1}^{L} W_i \tag{5.8}$$

Index i refers to the node number and L is again the total number of nodes in the domain.

Similarly the residual is defined as

$$R = \sum_{j=1}^{L} R_j \tag{5.9}$$

The integral in (5.7) is an inner product and suggests that W is orthogonal to R. Hence

$$\langle R, W\rangle_\Omega = 0 \tag{5.10}$$

Here $\langle R, W\rangle$ is the inner product between the functions R and W over the domain Ω.

Multiplying (5.6) by the weight W yields

$$\sum_{i=1}^{3}\sum_{j=1}^{3} V_j \nabla^2 N_j W_i = \sum_{i=1}^{3}\sum_{j=1}^{3} R_j W_i \tag{5.11}$$

Where 3 is the total number of nodes in the triangular element.

To force the residual to zero we integrate over the domain

$$\sum_{i=1}^{3}\sum_{j=1}^{3} V_j \left\langle \nabla N_j W_i\right\rangle_\Omega = 0 \tag{5.12}$$

When the domain Ω is discretized into elements e (5.12) becomes

$$\sum_{e=1}^{n}\sum_{i=1}^{3}\sum_{j=1}^{3} V_j \left\langle \nabla N_j W_i\right\rangle_e = 0 \tag{5.13}$$

Where n is the total number of elements deployed in the solution domain Ω.

To apply the boundary conditions we integrate by parts

$$\sum_{e=1}^{n}\sum_{i=1}^{3}\sum_{j=1}^{3} \left[-\left\langle \nabla N_j \cdot \nabla W_i\right\rangle_e\right]\{V_j\} = \left\{-\oint_e \left(\nabla N_j \cdot \mathbf{n}\right) W dS_e\right\} \tag{5.14}$$

Where S_e is the area of the sub-domain e.

We can easily construct the system of equations from (5.14) where the local matrix elements are

$$a_{ij} = -\left\langle \nabla N_j \cdot \nabla W_i\right\rangle_e \tag{5.15}$$

This expression underlines the importance of selecting a computationally efficient weighing function. A number of formulations have been developed based on specific choices for this function, most notably Galerkin's. Here W_i is chosen to be equal to the trial function

$$W_i = N_i \tag{5.16}$$

The final step involves solving the system of equations while including the boundary conditions. The general expression is

$$[A]\{V_j\} = \left\{ - \oint_e (\nabla N_j \cdot \mathbf{n})\, W dS_e \right\}$$

5.3 Thermo-electric model for DC excitation

5.3.1 Static model

An electrostatic model of a 3D cylinder was created with uniform conductivity. The thermoelectric heating model includes the voltage solution obtained from the electrostatic model used to compute the heat sources. The source is the deposited power and the dominant heat transfer mechanism is conduction while the boundaries are convective. It is assumed that the part is cooled through natural convection.

As can be seen in Figure 5.3, the deployed mesh is coarse as we do not expect major changes in the field solution between adjacent elements.

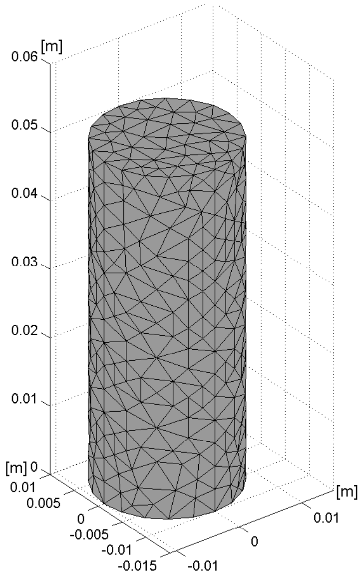

Figure 5.3: A meshed structure of a 3D cylindrical sample free of defects.

In addition to the dimensional parameters listed above, we define the thermo-physical properties of the part as follow :

- Length of cylinder: $L = 0.05\,m$.
- Radius of cylinder: $R = 0.01\,m$.
- Electrical conductivity: $\sigma = 5 \times 10^4\,S/m$.
- Material Density : $\varrho = 7250\,kg/m^3$.
- Heat capacity: $c = 440\,W/kg\ ^\circ C$.
- Thermal conductivity: $k = 40\,W/m\ ^\circ C$.
- Convection heat transfer coefficient: $h = 10\,W/m^2\ ^\circ C$.

For the boundary conditions, we specify the inward normal component of the current density as in (4.20) with

$$\mathbf{n} \cdot (\sigma \bigtriangledown V) = -\mathbf{n} \cdot \mathbf{J} = 32000\,A/m^2 \tag{5.17}$$

This is equivalent to a total input current of 10A. For the remaining boundaries, we adopt the conditions specified in (4.21).

With the parameters specified above, we predict the voltage drop from the top of the part to the bottom to be:

$$V = I\frac{L}{\sigma A} = \frac{L}{\sigma}J = 0.482\,V \tag{5.18}$$

where A is the cross-sectional area of the cylinder.

The solution is presented in Figure 5.4 as a slice view displaying the voltage distribution throughout the volume of the part.

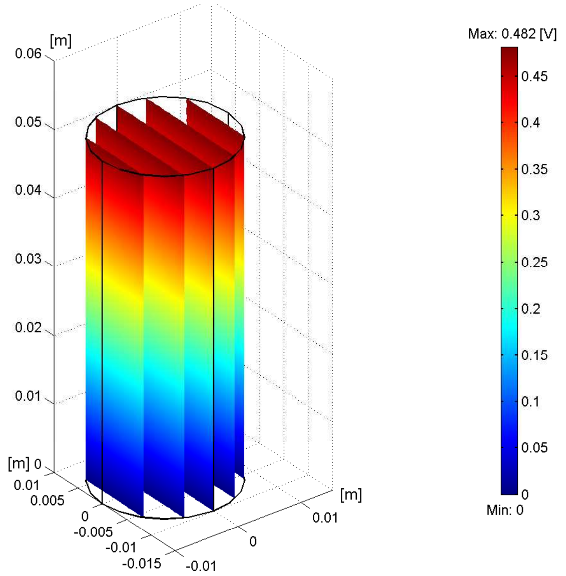

Figure 5.4: Voltage distribution for a cylindrical compact of constant conductivity driven by a current of 10A.

The electric potential V results in a heating power Q proportional to its magnitude as illustrated in (4.30), where the constant of proportionality is the conductivity σ.

The boundary conditions as in (4.48) and (4.49) are set to be of flux or Neumann type. These conditions will result in a temperature distribution presented in Figure 5.5.

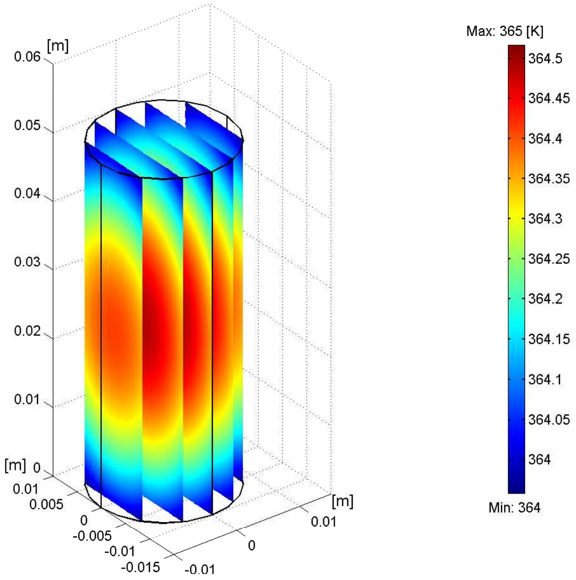

Figure 5.5: Temperature distribution in an unflawed cylindrical compact.

Similar to the temperature distribution obtained through the analytic solution, the temperature is at its maximum at $z = r = 0$ and decays until it reaches a minimum at the surface.

5.3.2 Transient analysis

To validate the applicability of the IR imaging technique for the detection of surface cracks and subsurface defects, it is necessary to first evaluate the temperature changes and ensure that they fall within the detection limits of our imager with reasonable margins. The theoretical defect sizes we are considering are on the order of $20\mu m$, which can be computationally cumbersome. However, a 2D representation of surface and near-surface defects appears sufficiently adequate to investigate the sensitivity of our method.

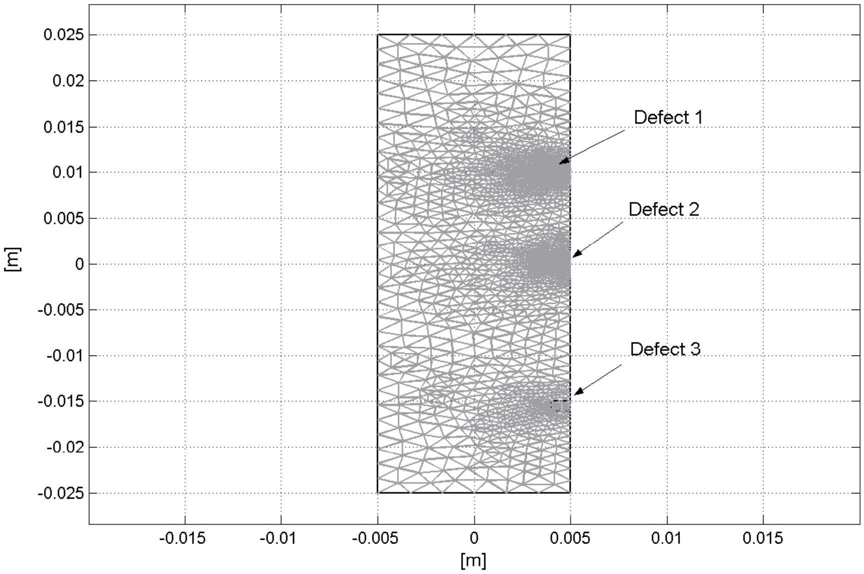

Figure 5.6: Dimensional and mesh parameters of the transient thermo-electrical model.

For the 2D geometry with flaws the resolution had to be adjusted to capture the hairline defects. The defects seen in Figure 5.6 have the spatial characteristics illustrated in Table 5.1.

Table 5.1: Defect sizes and locations.

	Length [μm]	Width [μm]	x-coordinate [m]	y-coordinate[m]
Defect 1	20	100	4.7×10^{-3}	1×10^{-2}
Defect 2	100	20	4.9×10^{-3}	0
Defect 3	500	1000	4.5×10^{-3}	-1.5×10^{-2}

This analysis is subdivided into two sections. The first focuses on the steady state condition, i.e., no time component is included. Second, we extend the previous model to include transient effects and consequently estimate the response time of the technique.

The defects we consider are voids with spatial parameters listed in Table 5.1 and the following thermo-physical properties:

- Material Density : $\varrho = 1.18\, kg/m^3$.

- Electrical conductivity: $\sigma = 35 \times 10^{-15}\, S/m$.
- Heat capacity: $c = 1005.7\, W/kg\ ^{\circ}C$.
- Thermal conductivity: $k = 0.026\, W/m\ ^{\circ}C$.

Voids or inclusions posses thermo-physical properties that are very different from those of the actual material. Consequently, the heating rate will be different. Furthermore, a transient excitation will cause a diffusion process to take place in the part, with a thermal gradient observable on its surface. Dynamic thermography, where a thermal image is taken in real time, offers the possibility to capture this time dependent process and subsequently allows the detection of subsurface defects and small surface breaks.

The following set of figures shows the transient thermal response to a step current excitation of 10A.

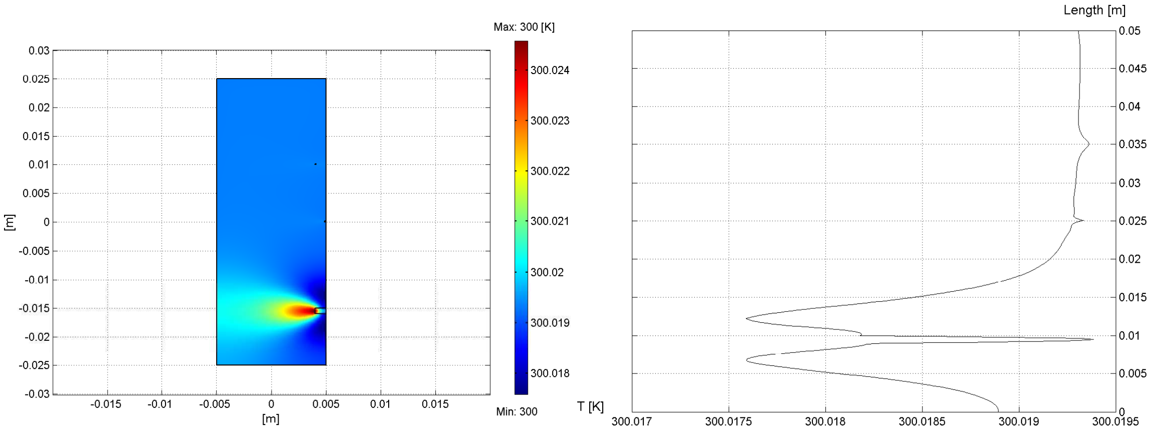

(a) (b)

Figure 5.7: (a) Surface temperature after 0.2 sec, and (b) profile along the z-axis.

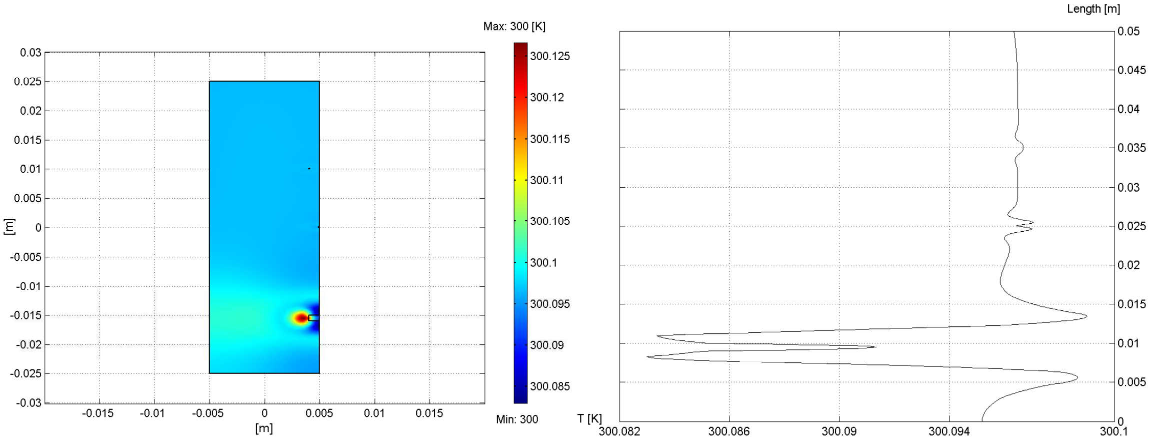

(a) (b)

Figure 5.8: (a) Surface temperature after 1 sec, and (b) profile along the z-axis.

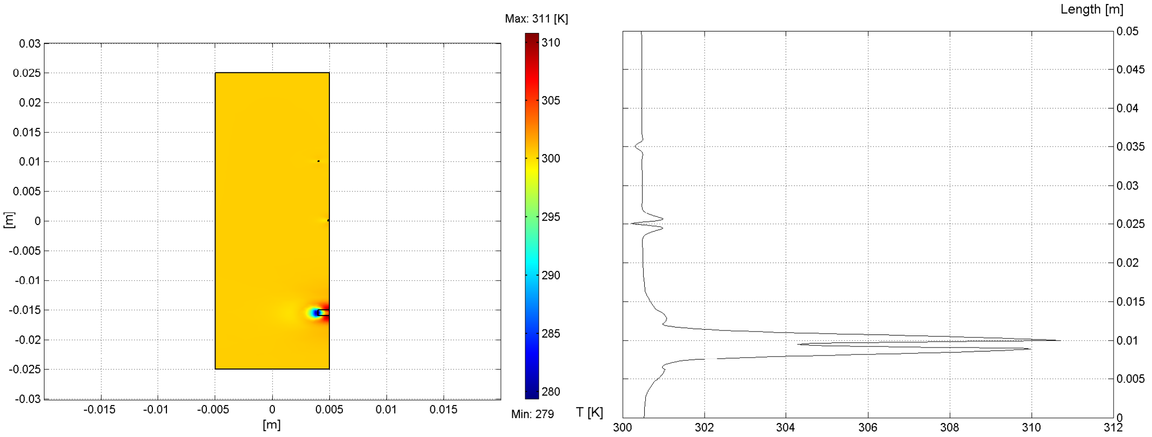

(a) (b)

Figure 5.9: (a) Surface temperature after 5 sec, and (b) profile along the z-axis.

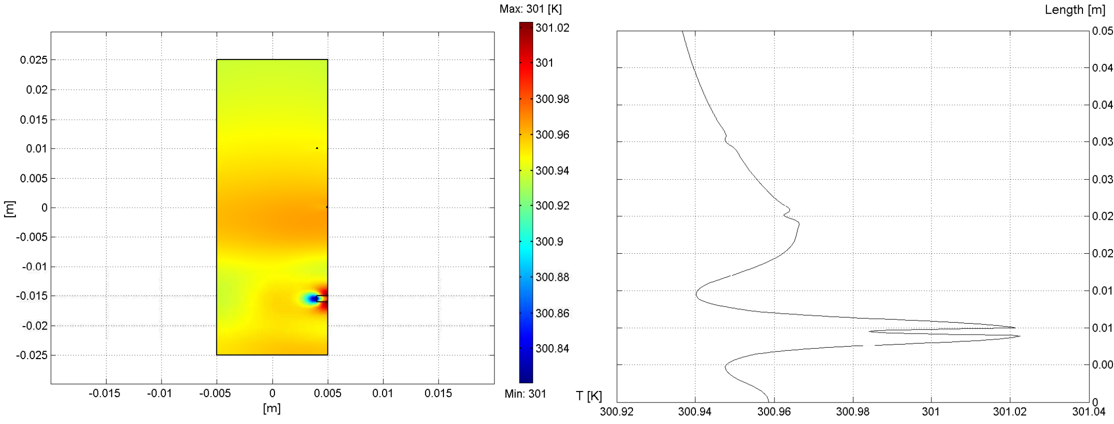

(a) (b)

Figure 5.10: (a) Surface temperature after 10 sec, and (b) profile along the z-axis.

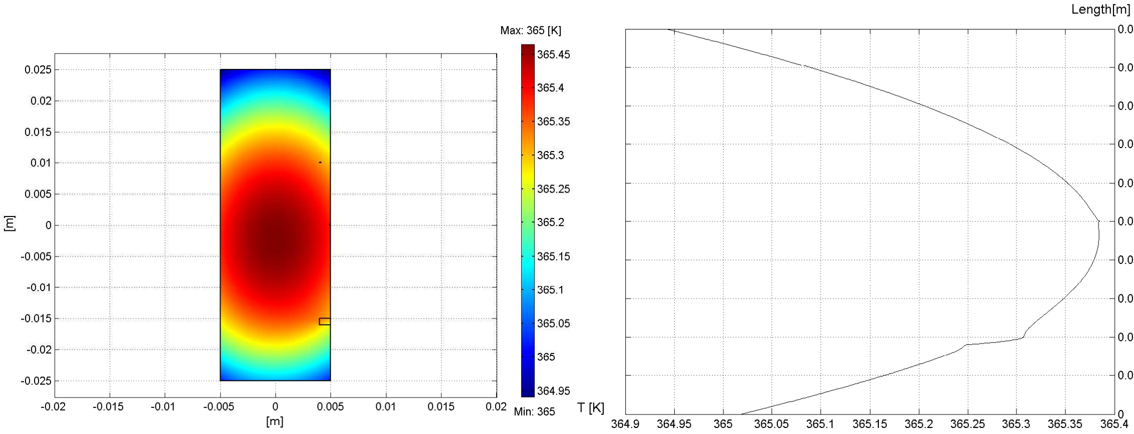

(a) (b)

Figure 5.11: (a) Surface temperature at equilibrium, and (b) profile along the z-axis.

From these figures we conclude that dynamic thermography offers significant advantages, including the possibility to detect subsurface defects and very small surface-breaking flaws. The results summarized in Figure 5.12 show a distinguishable signature from a small surface crack. A noticeable temperature change indicates the presence of a subsurface defect.

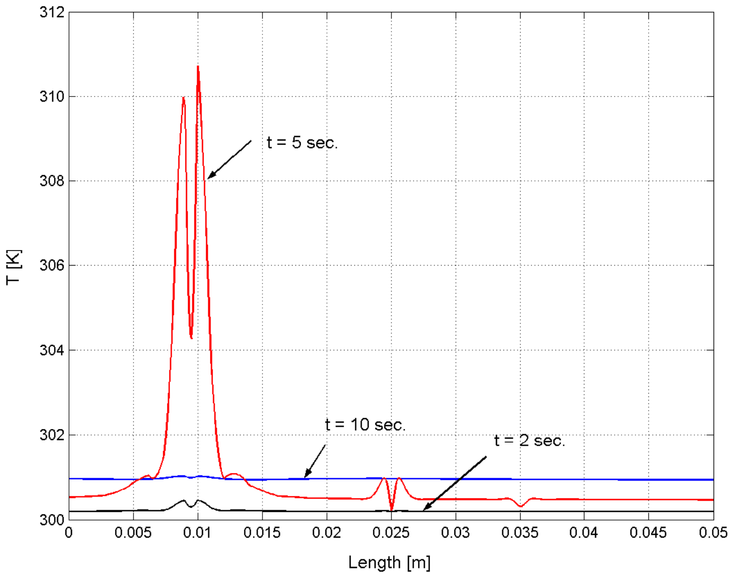

Figure 5.12: Temperature profile along the z-axis at various time steps increments.

The data plotted in Figure 5.12, reveal the detection limits for the simulated flaws. This also sets the performance requirements of the IR imager and allows the establishment of test conditions. Table 5.2 lists the preliminary requirements for a suitable IR camera.

Table 5.2: IR camera requirements

Requirement	min.	commercial camera
Frequency	$2\,Hz$	$30\,Hz$
Thermal sensitivity	$0.2\,°C$	$0.08\,°C$
Spectral range	$8 \sim 10\,\mu m$	$7 \sim 13.5\,\mu m$

After estimating the sensitivity of the method and establishing the equipment requirements, we then proceed to the experimental measurements. The camera, whose parameters are listed in Table 5.2, provides sufficiently large margins for realistic measurements that include environmental effects and possible camera-to-camera variations.

5.4 Induction heating model

The electro-thermal problem where the heating mechanism is induction such that current is inductively coupled onto the part to cause an increase in temperature. Here the phenomenon is described with a system of equations that includes the well known and previously described heat equation and the following:

$$\sigma \frac{\partial \mathbf{A}}{\partial t} + \nabla \times \left(\frac{1}{\mu} \cdot \nabla \times \mathbf{A} \right) = \mathbf{0} \tag{5.19}$$

where σ is the conductivity, $\mathbf{A}$ is the magnetic vector potential, and μ is the permeability.

To obtain a numerical solution an axis-symmetric model was constructed. Furthermore, defects with parameters that are comparable to those observed in the industry were included. Table 5.3 lists the defect locations and size.

Table 5.3: Defect sizes and locations.

	radius $[mm]$	r-coordinate $[mm]$	z-coordinate$[mm]$
Defect 1	0.5	18.5	10
Defect 2	0.5	19.5	30

The model also includes the induction coil which is selected to be made of copper and is water cooled to a fixed temperature ($293°K$). Surface current on the coil is 50A and the frequency was selected to $50\,KHz$ to guarantee a skin depth of at least $1mm$. For the heat transfer model all sides but the bottom are set for free convection similar to the DC heating model.

The following plots depict the solution at different time steps.

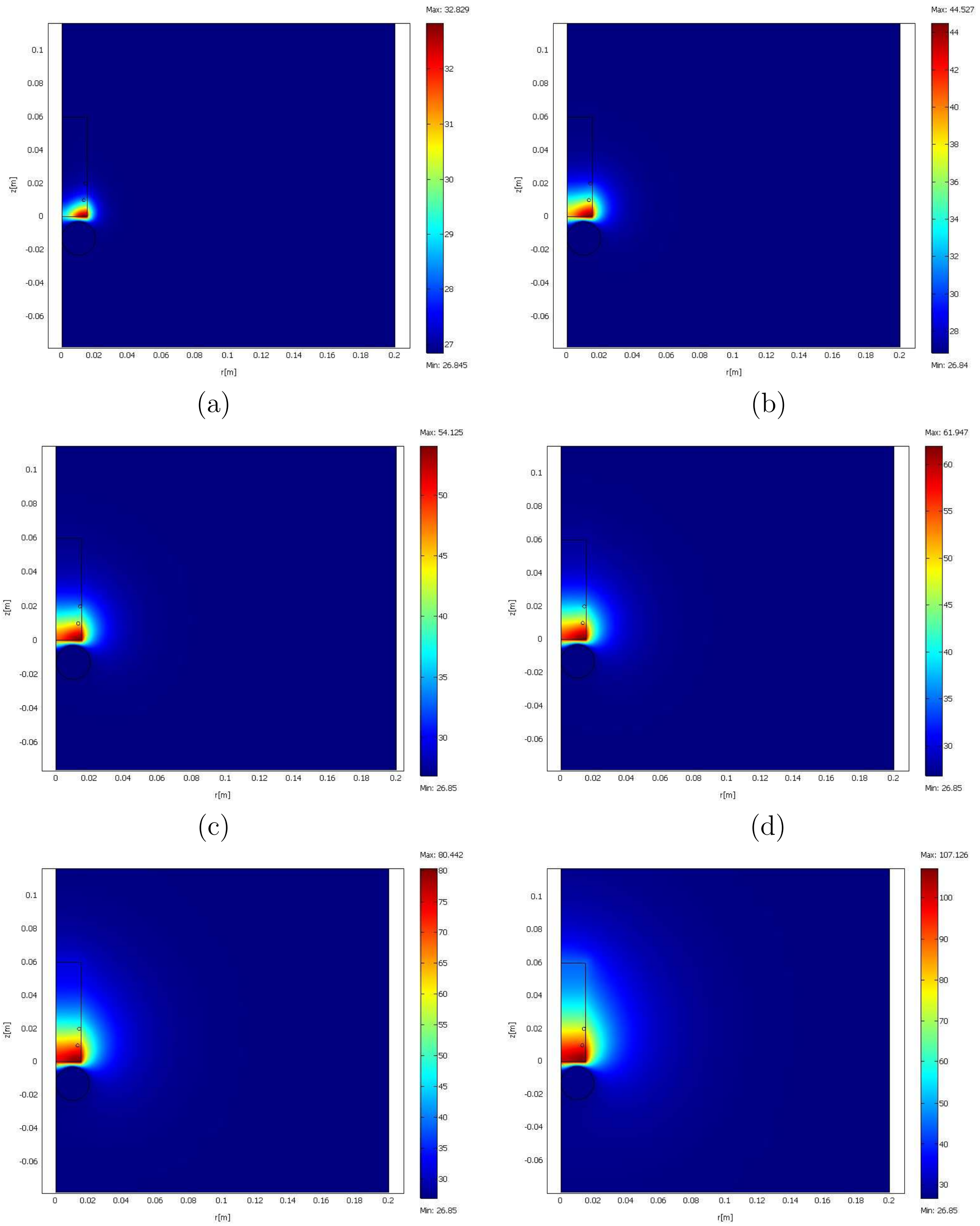

(a) (b) (c) (d) (e) (f)

Figure 5.13: (a) Surface temperature at 2 sec, (b) 10 sec, (c) 20 sec, (d) 30 sec, (e) 60 sec, and (f) at 120 sec.

A thermal line profile of the surface to be imaged is generated to capture in detail the temperature gradient at various time steps as shown in Figure 5.14.

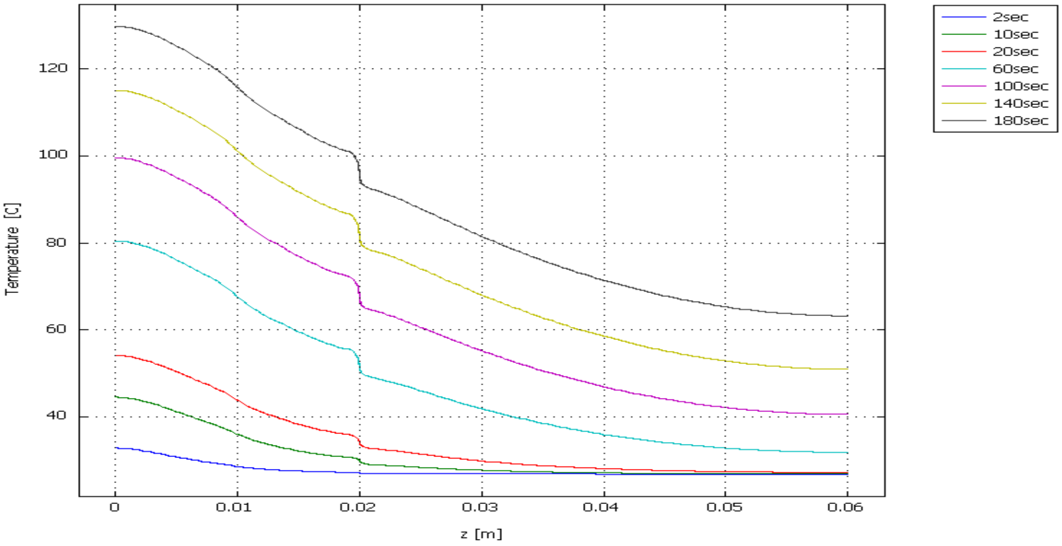

Figure 5.14: Surface temperature at various time steps.

It is clear that the surface crack is easily detectable with the camera whose parameters are listed in Table 5.3. However, the subsurface flaw has no distinguishable thermal signature. Figure 5.15 plots the heat flux within the part at the surface of interest. This shows that there is a heat concentration defined by the defect as expected. Unfortunately, the temperature is too low for it to cause a distinguishable signature.

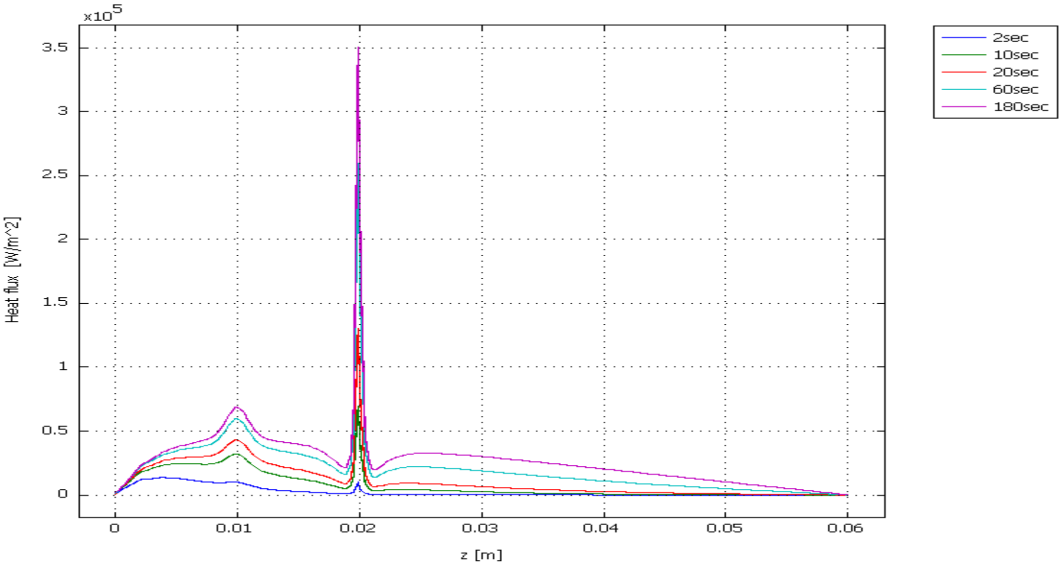

Figure 5.15: Heat flux at various time steps.

For the application of defect detection in green state powder-metallic compacts there is A temperature limit after which the quality of the part maybe compromised. This will present the main limitation of this technique for the detection of subsurface defects.

5.5 Convection Model

Similar to the electro-thermal problem, modeling the thermal behavior of the part as it exits the compaction press and travels down the conveyor belt to the sintering station is complex and involves a system of equations that represent fluid flow and heat transfer in the fluid. This system includes the incompressible Navier-Stokes equations; the momentum balance and the conservation condition [23]:

$$\begin{cases} \varrho\frac{\partial\mathbf{u}}{\partial t} + \varrho\left(\mathbf{u}\cdot\nabla\right)\mathbf{u} = -\nabla p + \eta\nabla^2\mathbf{u} + \mathbf{F} \\ \nabla\cdot\mathbf{u} = 0 \end{cases} \tag{5.20}$$

Here $\mathbf{u}$ is the velocity field, p is the pressure, $\mathbf{F}$ is the volume force, ϱ is the density of the fluid, and η is the viscosity of the fluid.

Due to the underlying complexity it was reasoned that a simpler model can be implemented to present a reasonable approximation of the fluid flow-heat transfer model. The model that was constructed is a pure heat transfer model with an "adaptive" convection coefficient to capture the effect of fluid velocity. The mesh was chosen fine enough to capture convection effects on the surface. Table 5.4 lists the defect locations and Figure 5.16 shows mesh parameters and part dimensions.

Table 5.4: Defect sizes and locations.

	radius $[mm]$	x-coordinate $[mm]$	y-coordinate$[mm]$	z-coordinate$[mm]$
Defect 1	0.5	19.5	0	20
Defect 2	0.5	18	0	30
Defect 3	0.5	18.5	0	40

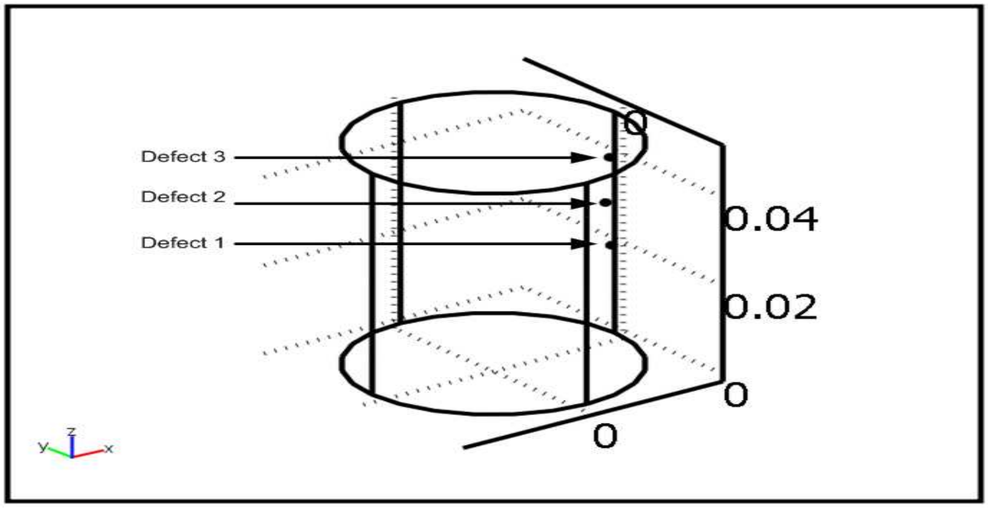

Figure 5.16: Drawing for 3D model.

The following figures depict the temperature throughout the volume of the part at different time steps.

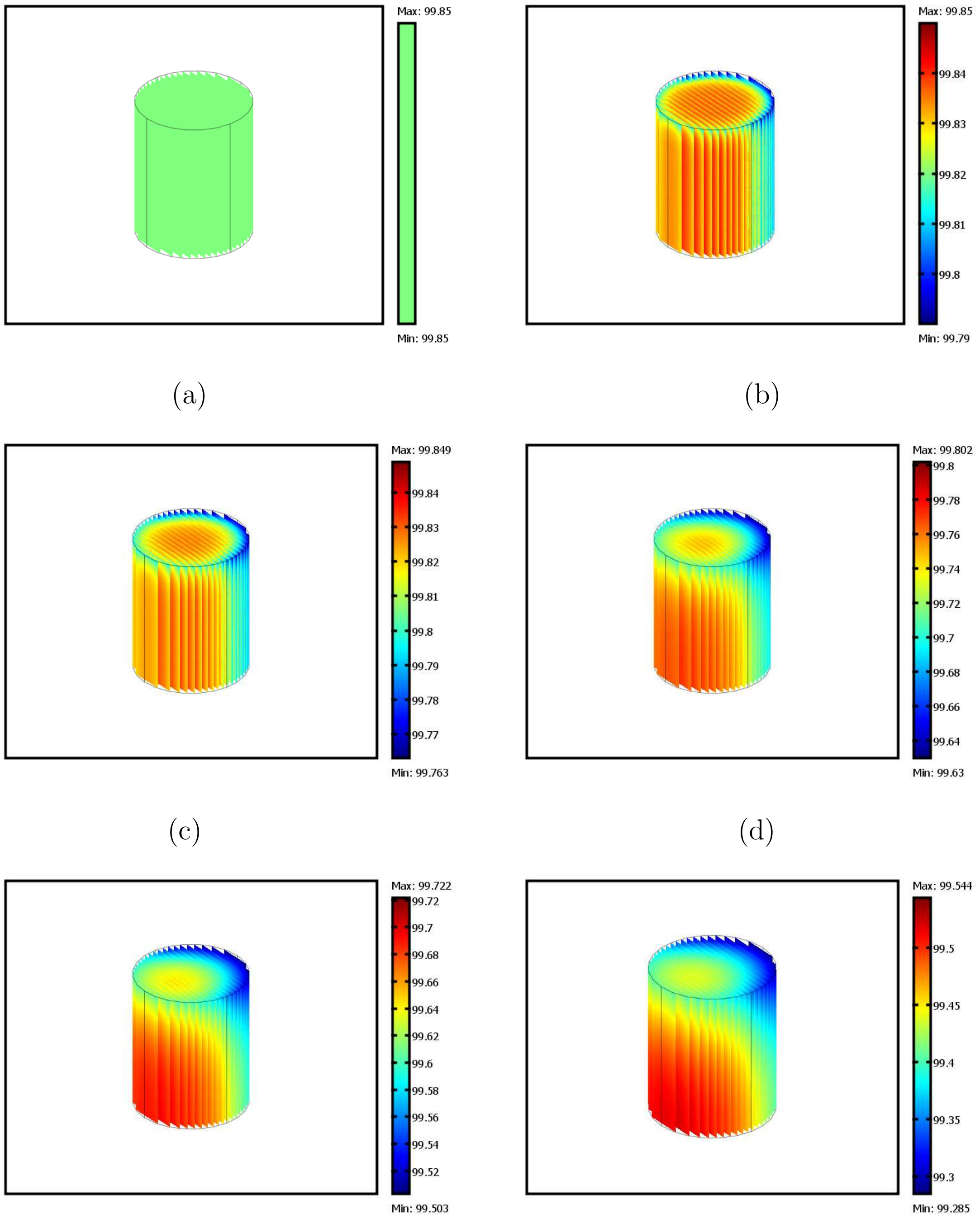

(a) (b)

(c) (d)

(e) (f)

Figure 5.17: (a) Temperature distribution in the part at 0 sec, (b) 0.5 sec, (c) 1 sec, (d) 5 sec, (e) 10 sec, and (f) at 20 sec

Figure 5.18 lists the thermal profiles on the plane that contains the defects.

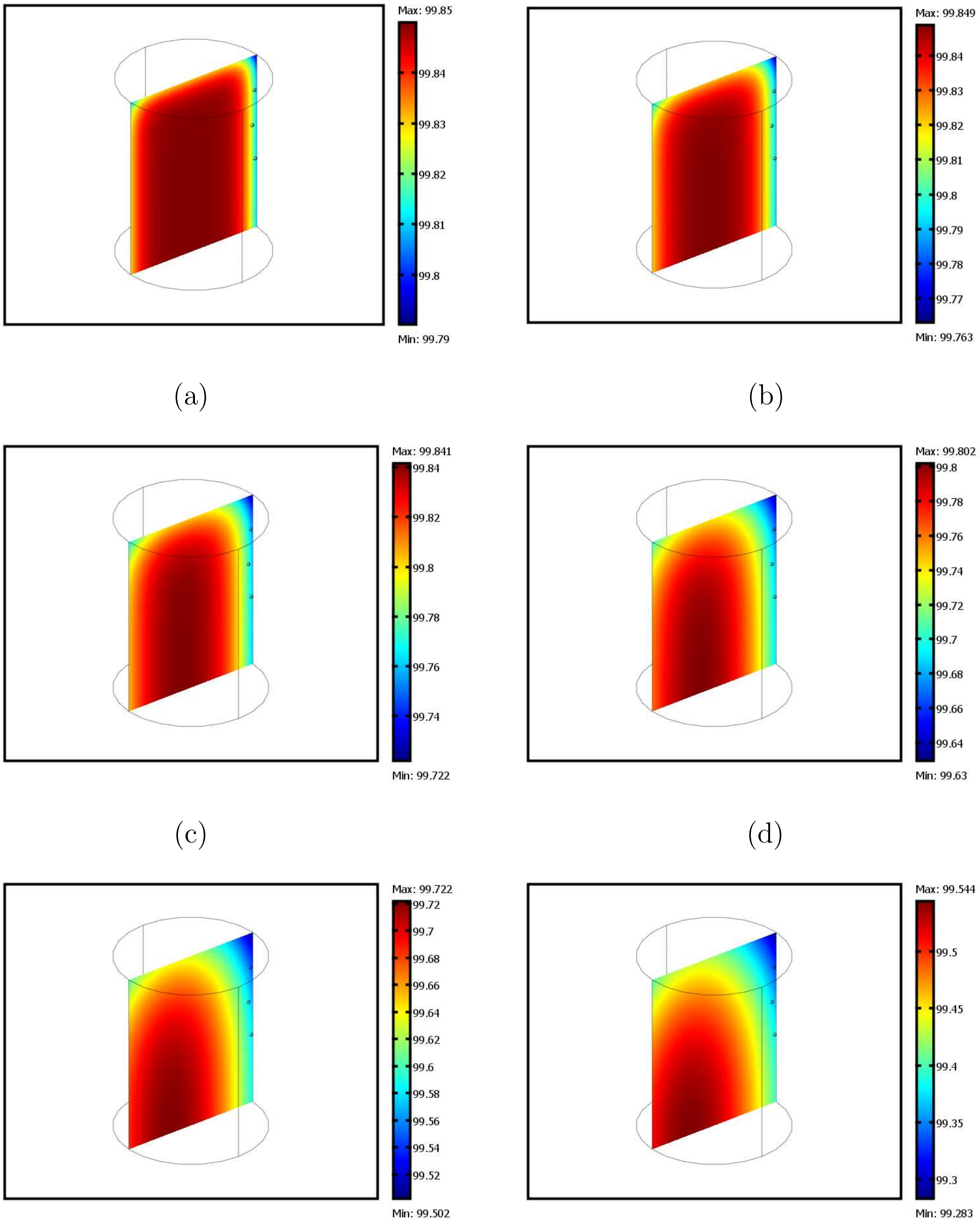

(a) (b)

(c) (d)

(e) (f)

Figure 5.18: (a) Slice view of the temperature distribution in ^oC in the plane that contains the defects at 0 sec, (b) 0.5 sec, (c) 1 sec, (d) 5 sec, (e) 10 sec, and (f) at 20 sec

It is unclear from these plots whether the defects presented any observable signature; this requires a more thorough view into the temperature distribution. For this reason we capture a thermal profile along the surface as shown in Figure 5.19

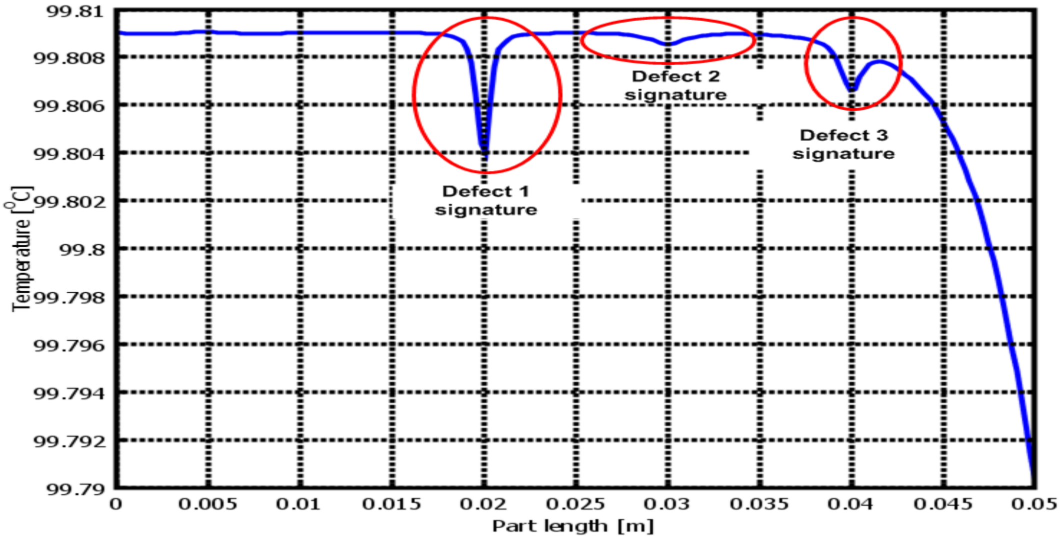

Figure 5.19: Line profile along the surface at 0.5sec.

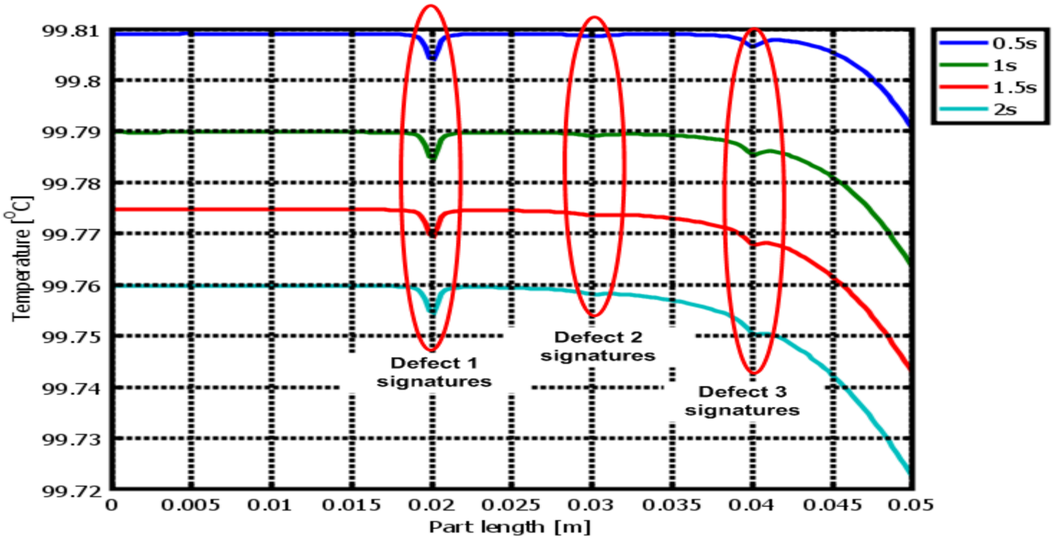

Figure 5.20: Line profile along various time steps.

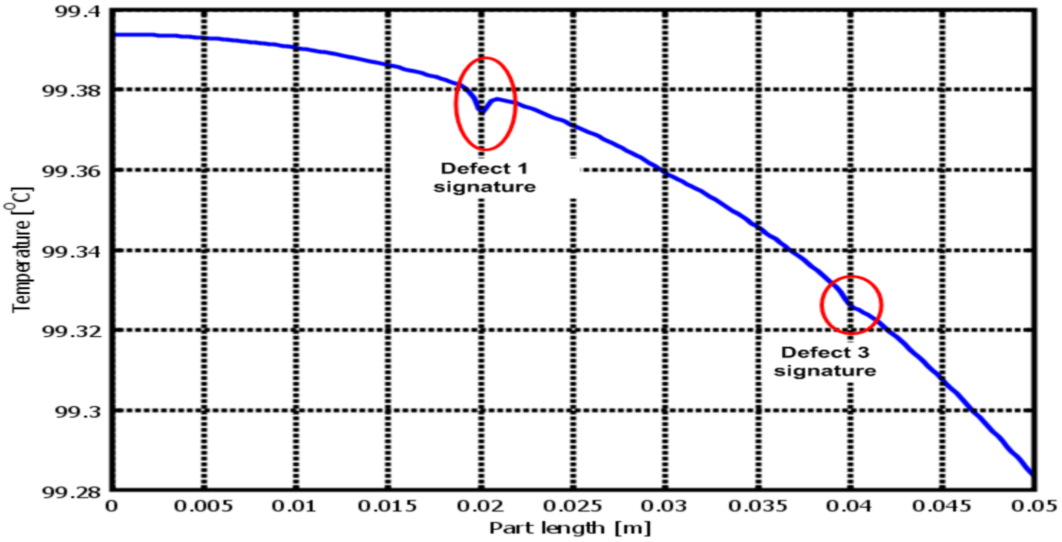

Figure 5.21: Line profile 20 seconds (after reaching the observation point)

It is also clear from this final model that surface cracks will be easily detectable with a camera that meets the requirements listed in Table 5.2. Subsurface defects present a challenge since only parts with a minimum size present distinct signatures at specific time steps.

All four models described in this chapter agree in principal and confirm the predictions from the analytical model. These models highlight the importance of employing an external pulsed heat source and the required synchronization between heating and detection. Even in the convection model where heat is generated by the process that only captures the residual heat within the part, the camera system has to be placed in a well-defined location relative to the time where the defect signature is at its peak. From this analysis it became clear that for this application (defect detection in powder metallic compacts) many commercial camera systems will be suitable and provide adequate sensitivity, resolution and speed.

Chapter 6

Experimental Study

6.1 Introduction

To complement to the analytical studies and numerical modeling, tests were carried out in an effort to confirm the applicability of infrared detection of defects in the P/M components. The feasibility study is extended to realize practical test systems that can be deployed in manufacturing. Thereafter, investigations were completed to define the limits of each approach. Initially, the direct current heat source approach is revisited then extended to include pulsing of DC current and generalized for when any heat source is used (such as a hot plate).Then, in an effort to establish a fully contactless solution, a pulsed inductive set-up is devised. Such a system will be comprised of an inductive heating sub-system, an infrared imaging unit and a synchronization circuit. Lastly, on-line testing that relies on capturing radiation that emanates from pre-heated parts and initial heating is a result of friction losses in the compaction step.

In addition to the experimental study, this chapter also includes the software development effort. First, most processing was completed off-line using various tools such as Matlab, custom software from camera manufacturers, and Microsoft Visual C++

to manipulate the data for display and processing. Thereafter, custom software was designed to allow fast data processing. The software package was designed specifically for the P/M industry, hence it was optimized mainly to accomplish two functions: 1) provide a go, no-go feedback for press operators with various alarms such as press speed error and part boundary images, and 2) provide a more comprehensive user interface and access to processing parameters and raw data for engineers to allow them to do more extensive data analysis.

6.2 Off-line testing

6.2.1 Steady-state DC heating arrangement

We have configured a basic IR imaging arrangement (see. Figure 6.1) which includes an IR camera with the following performance specifications:

- Field of view (FOV) $24° \times 18°/0.3m$.
- Spatial resolution $1.3\,mrad$.
- Thermal sensitivity $0.08°C$.
- Detector $320 \times 240\,pixels$.
- Frame rate $30\,frames/sec$.
- Spectral range $7.5\,to\,13\mu m$.

In addition to the camera, equipment is configured such as a DC power supply, a data collection and analysis computer, and electric contacts to allow the injection of DC current.

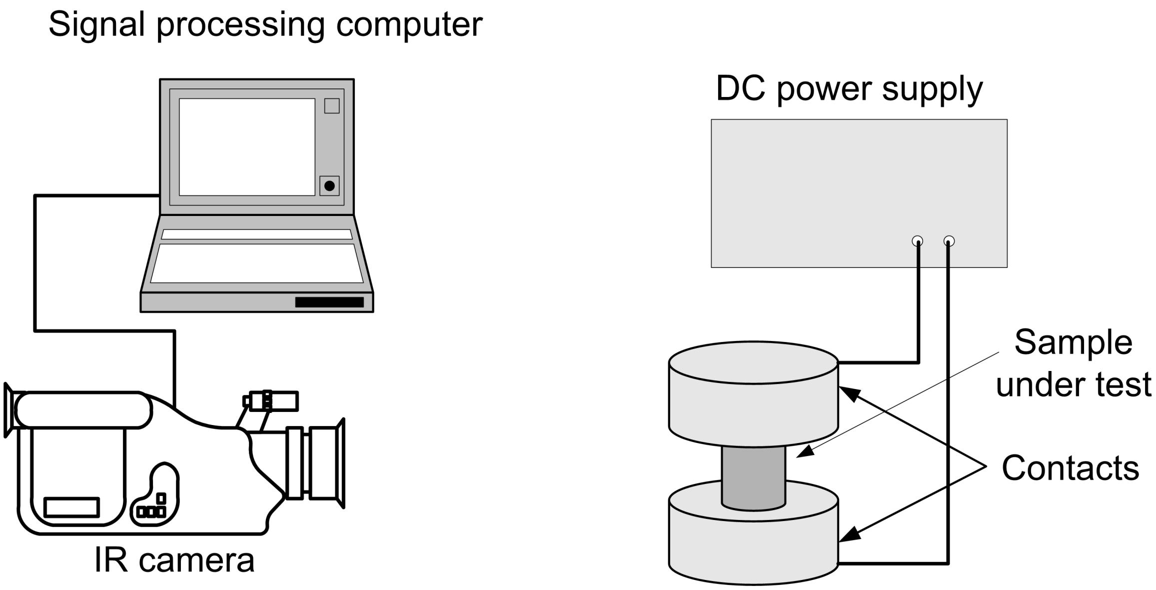

Figure 6.1: Experimental test arrangement.

The current injection scheme utilizes a setup with two large aluminum block contacts to maintain uniform current flow into the part and low contact resistance.

Figure 6.2: Generic test arrangement showing the electrode contacts.

Figure 6.2 details the test arrangement where the camera is located at a distance of approximately $0.3\,m$ away from the area of interest.

6.2.2 Steady-state measurement of flaws

In an effort to evaluate the effects of flaw size, shape, and orientation, a number of defects were artificially created. In particular, using a simple exacto knife we have created surface defects whose dimensions are listed in Table 6.1.

Table 6.1: Flaw parameters in a green-state cylindrical part.

Flaw #	Length [mm]	Width[μm]	Depth [μm]	Orientation [μm]	Location [cm]
1	10	< 20	< 20	Horizontal	1
2	1	20	20	Horizontal	2
3	2	20	20	Vertical	3
4	10	< 20	< 20	Vertical	5

These defects were created in a cylindrical part of 1000B powder without lubrication; the compaction was carried out in a dual-punch press. This part was subjected to a DC current flow of 20A. The next step involves the IR image acquisition, storage to a PC, and Matlab post-processing using the thresholding technique. Figure 6.3 illustrates the IR image taken from the part described in this section prior to any processing. The image obtained is an index image format which is transformed in the camera to a gray-scale. It takes the form of an intensity matrix where the intensity of each pixel is in the range from 0 , to 255. The elements in the intensity matrix represent gray levels with 255 representing full intensity [17]. This image is later paletted for viewing using a simple coloring scheme (using Matlab) where the base temperature is encoded in green, cooler areas are represented in blue and hot spots are in red.

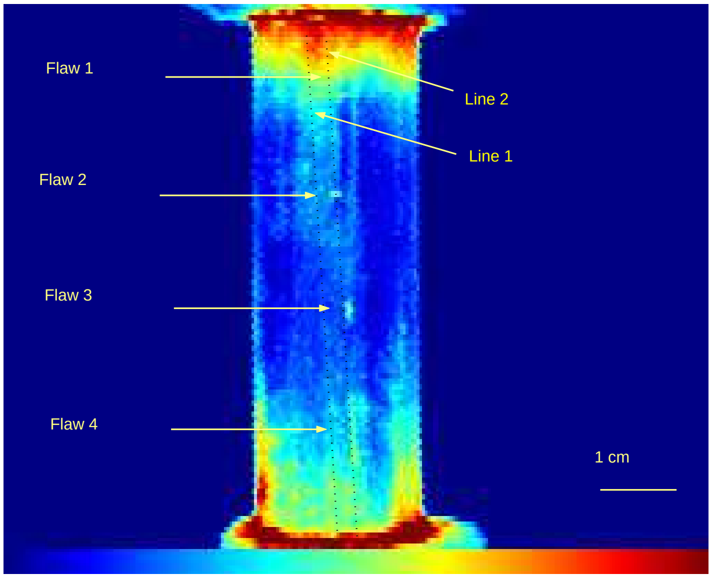

Figure 6.3: Generic IR image recording from a cylindrical part.

To quantify the temperature gradient caused by the presence of a defect we generate a line profile along the part, precisely intersecting the area of interest. Figure 6.4 depicts the image profile along a line that traverses across all defects and a second line parallel to it crosses a flawless area.

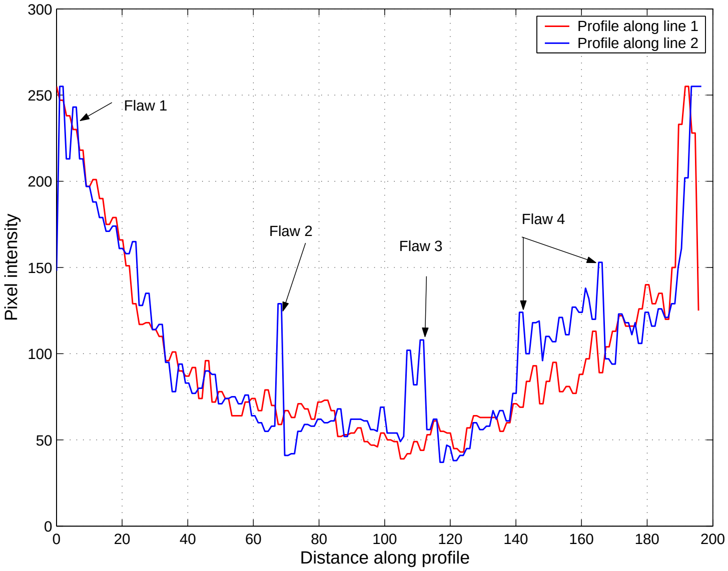

Figure 6.4: Profile along the two dotted lines in Figure 6.3 , with a spatial pixel to pixel distance of $300\mu m$.

6.2.3 Image processing enhancement

Applying simple image processing techniques, it is shown that qualitative flaw information can be gained. The thresholding concept is based on the idea of selectively eliminating areas with temperatures below a preset value. Many algorithms have been proposed to automate this operation. A simple scheme utilizes the histogram (the representation of the number of pixels at each level), while the more elaborate algorithms use contextual and statistical information including information from adjacent pixels [17].

A Matlab program was written to set an intensity threshold and convert the image into a “binary” representation. In other words, a two level representation where all pixels whose values reach or exceed the threshold value are assigned to a “bright” category. Pixels with values below the preset value are assigned to a “dark” category.

Figure 6.5 represents the previous IR image after thresholding.

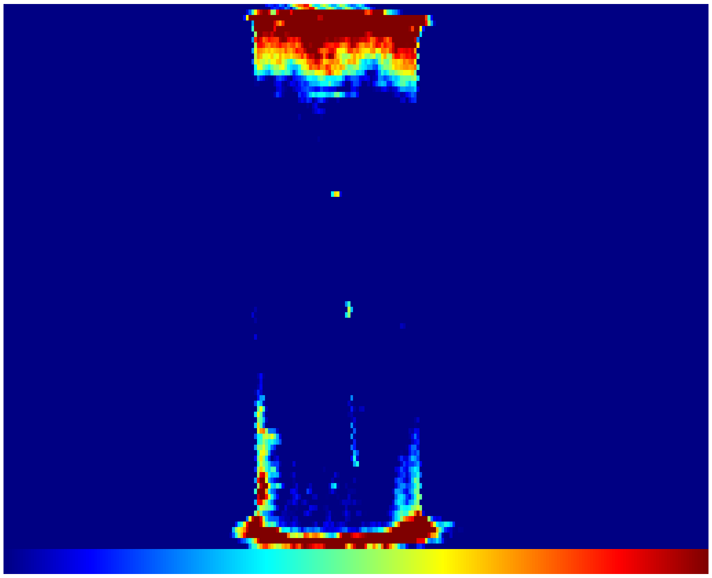

Figure 6.5: IR image of Figure 6.3 part after thresholding.

Here, the defects signatures are more visible making a go, no-go type of evaluation possible.

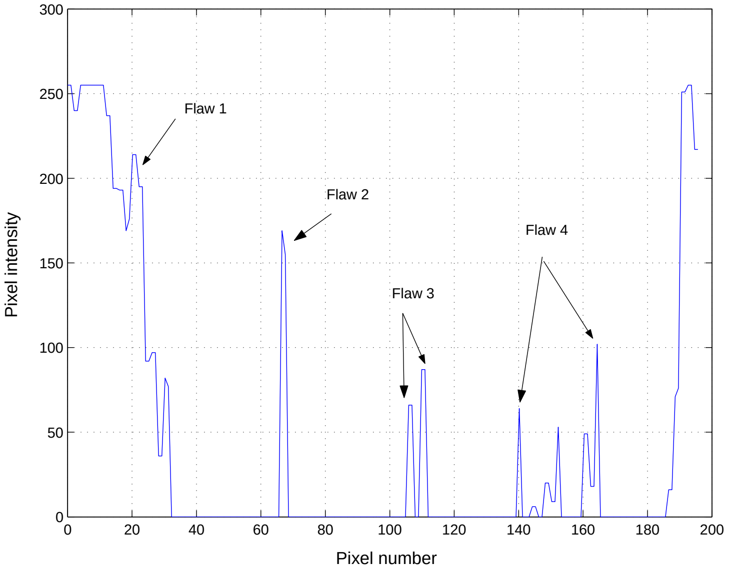

Figure 6.6: Temperature profile along the center line of the image after thresholding with a spatial pixel to pixel distance of $300\mu m$.

The results presented in this section show that sizable flaws can easily be detected through a steady state test arrangement. However, as was demonstrated in the theoretical modeling, very small surface cracks and subsurface defects cannot be detected; they require a dynamic test arrangement.

We tested a number of simple green-state parts with different material and lubrication constituents and varied densities. We also tested complex and multilevel parts with surface defects. The complex samples include surface breaks located between levels and in other areas that constitute a challenge for the part manufacturers.

6.2.4 Pulsed DC heating arrangement

As confirmed in the analysis and in the initial testing, a static imaging system is limited and can only detect surface discontinuities in simple geometries. For complex parts, corner cracks or subsurface defects a pulsed system is required. This system is devised using a simple set-up (shown in Figures 6.7 and 6.8). This set-up utilizes a DC power supply (preferably a programmable), a switching device (a MOSFET), the camera and computer systems and a synchronization unit which can be a pulse or a function generator. This latter device is crucial as it allows or precise timing of the energy deposition (power supply) with the imaging (the camera). This timing requirement is the critical parameter required to estimate the depth and location of a subsurface defect.

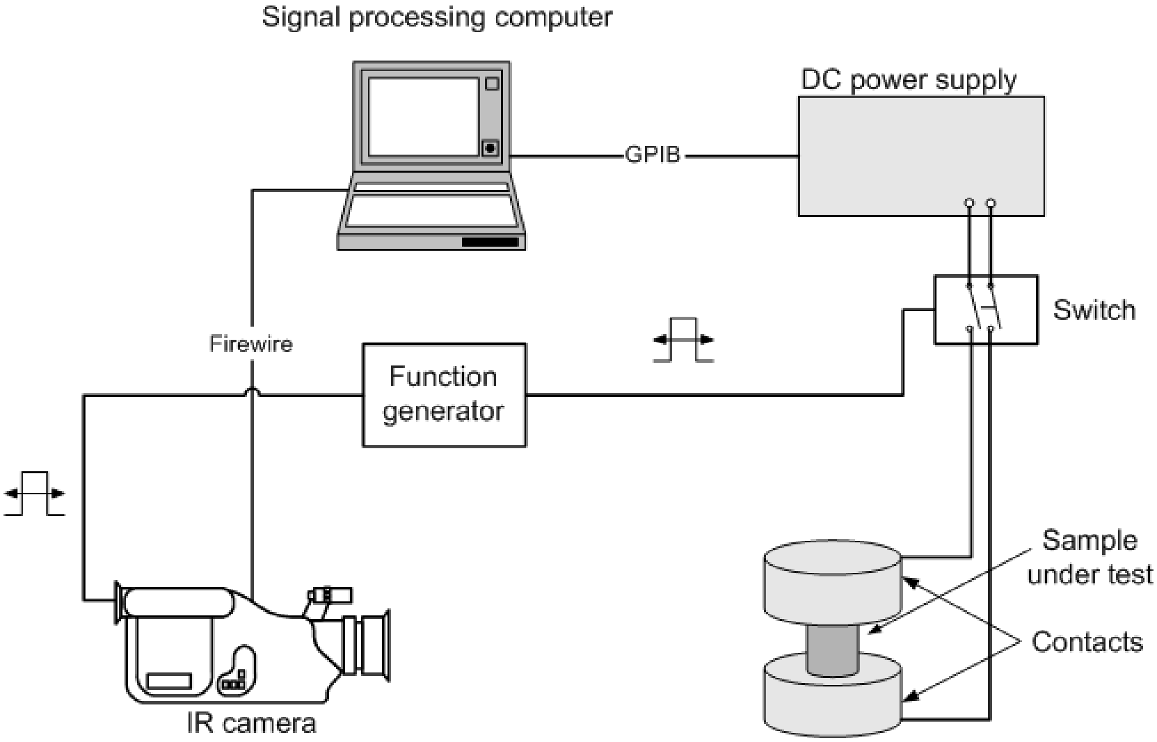

Figure 6.7: Arrangement for the pulsed DC test system.

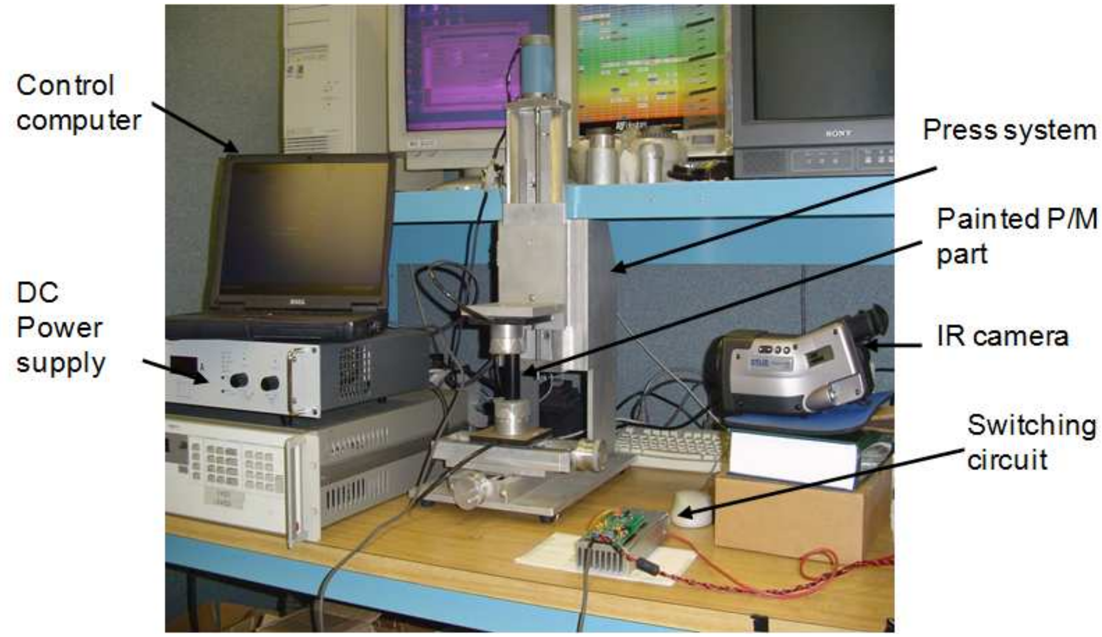

Figure 6.8: Picture of the pulsed DC setup.

6.2.5 Pulsed DC heating measurements

Dynamic testing was performed on parts that were coated to increase the emissivity to a level that reaches approximately the emissivity of a black body. To accomplish this task black paint is evenly sprayed over the surface in an effort to reduce the reflectivity, especially in cylindrical parts. In addition to the applied coating, the part was drilled from the opposite side to simulate a subsurface defect of 1mm diameter at a distance of approximately 2 mm below the surface. Figures 6.9-6.11 depict the thermal part images along with associated line profiles.

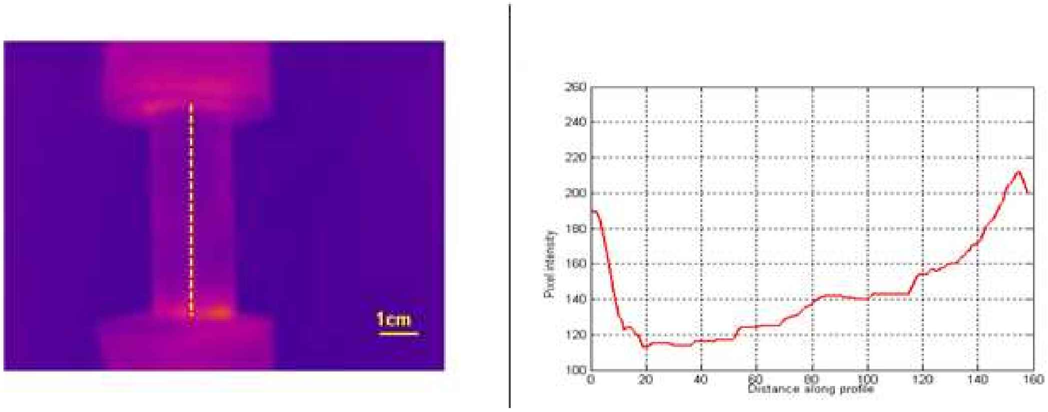

(a) (b)

Figure 6.9: (a) IR recording of the cylindrical part shown in Figure 6.8 at t=1sec., and (b) Profile along the dotted line.

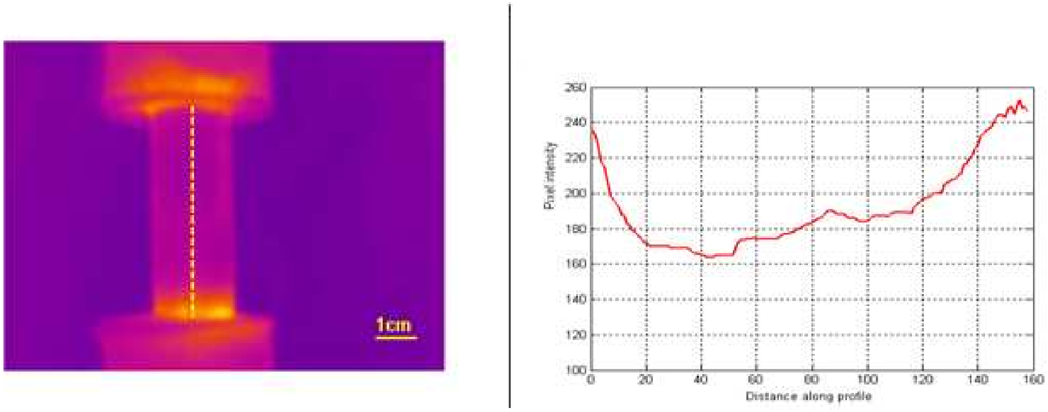

(a) (b)

Figure 6.10: (a) IR recording of the cylindrical part shown in Figure 6.8 at t=10sec., and (b) Profile along the dotted line.

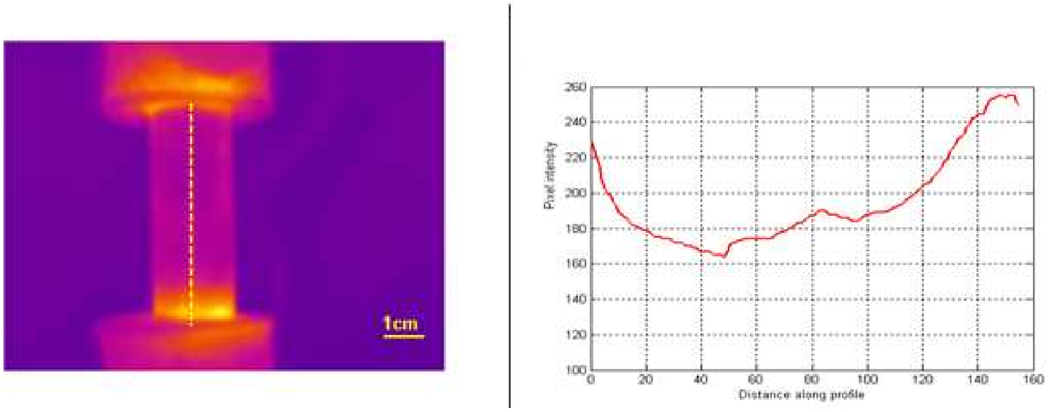

(a) (b)

Figure 6.11: (a) IR recording of the cylindrical part shown in Figure 6.8 at t=15sec., and (b) Profile along the dotted line.

After a 40A DC current is applied as a step function, the temperature begins to increase from 302.1K to 363.2K over a time period of 15s. One can observe that after 12s a characteristic thermal signature arises that is indicative of the subsurface flaw. However, as the temperature reaches equilibrium, after 15s - 20s, this transient signature disappears. This is true for simple parts; however more complex parts show a series of new challenges. The gears shown in Figure 6.12 present two typical difficulties encountered owing to their geometric arrangement. First, the gear teeth cause non-uniformity in the part, which in turn causes reflections. Second, the multilevel nature of the part makes it prone to corner cracks. Corner cracks cannot easily be detected due to complicated heat transfer mechanisms at the level interface.

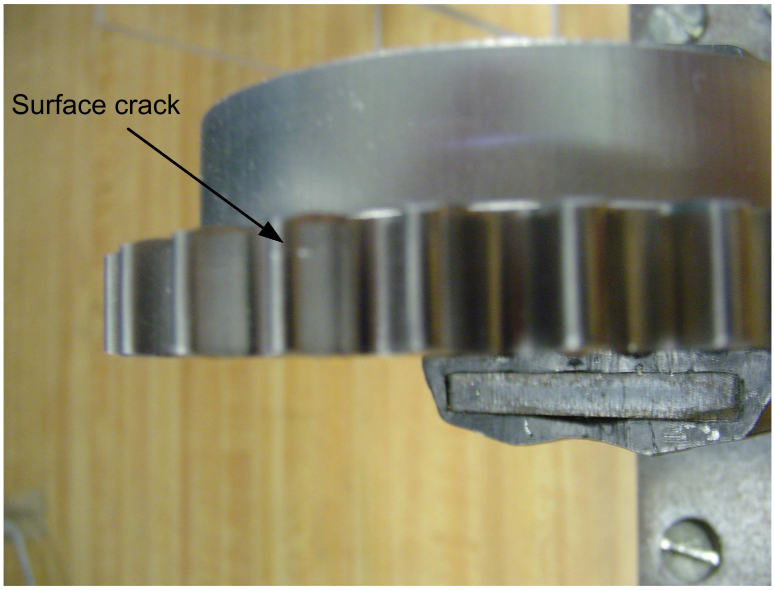

Figure 6.12: Surface crack on a tooth of a complex multilevel part (parts courtesy of Plansee AG).

The parts are two-level gears and where the first level includes a ring of teeth. The first level has the dimensions of 9 mm (height) by 75 mm (outer diameter). The dimensions for the second level are 11 mm (height) and 59 mm (outer diameter).

Here the cracks are typically less than $20\mu m$ in size. These steel powder compacts are constructed with 1.0% Cu, 0.2% C and lubricated with 0.8% wax. The density ranges from 6.8 g/cm3 to 7.1 g/cm. These defects are not easily detectable if the source of heating is direct current (DC) because it requires high current density and additional electrode contacts to insure uniform current flow throughout the part.

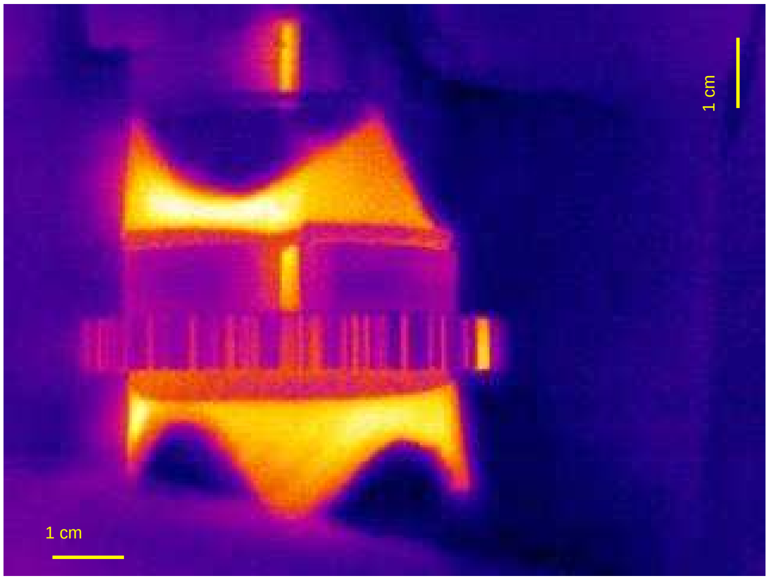

Figure 6.13: IR image of a gear with a surface crack on a tooth (shown in Figure 6.12) subject to a pulse of current.

These thermal measurements on complex gears show that the heat source is of extreme importance. It is concluded that the injection of a DC current is not appropriate unless multiple probes are used to maintain uniform current density throughout the volume of the part including its surface. Furthermore, this requirement adds complexity to the measurement instrument and makes its operation difficult to use, thereby limiting its versatility.

6.2.6 Pulsed hot plate heating measurements

Active imaging using electric current as the heating mechanism is very repeatable and controllable. However, there are other methods and heat sources that can be utilized successfully for the detection of larger cracks. This was investigated and tested with surface defects and even subsurface anomalies with parts made of various materials.

The basic setup shown in Figure 6.14 uses a hot-plate to cause a temperature increase in the samples while an infrared (IR) camera captures thermal sequences. The images are processed with our own software to show the heat flow from the bottom of the parts to the top reach thermal equilibrium. The resulting time dependent thermal signatures are directly influenced by the material parameters and the integrity of the parts. The imaging system is shown in Figure 6.14.

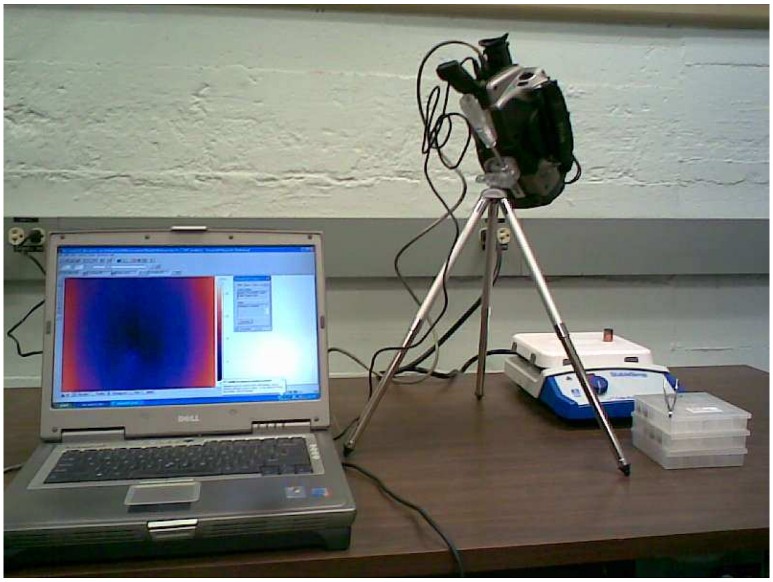

Figure 6.14: Test arrangement that utilizes a hot plate.

This plate was externally controlled to provide a heat source of 200C for a duration of 20 sec. Testing was conducted at a fixed temperature and we observed the temperature rise on the top surface of the parts. Thereafter, the infrared image sequences were processed to display the images at various time steps. A snapshot after 16 seconds is shown in Figures 6.15, 6.16, and 6.17 along with the contour plot which proved to be very useful in highlighting the fines. In total, testing was conducted on 50 parts in batches, some of which include fines. One of the purposes of this protocol is to evaluate the detection scheme for finding fines in these parts.

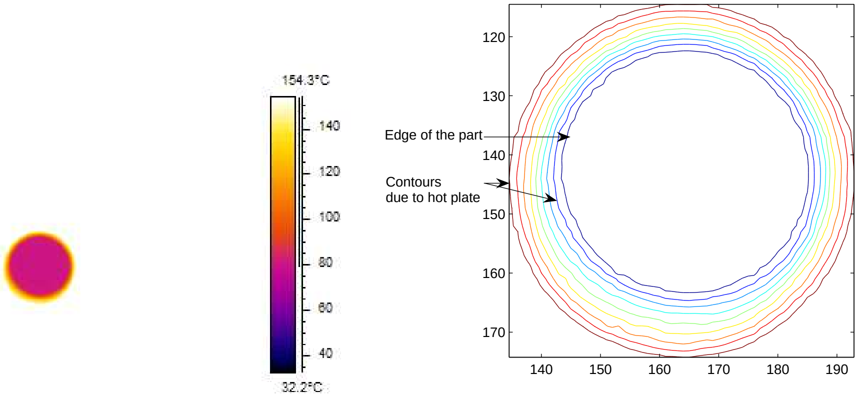

(a) (b)

Figure 6.15: (a) Thermal image captured from the top of the part shown in Figure 6.14 with no fines, and (b) contour plot of the same part.

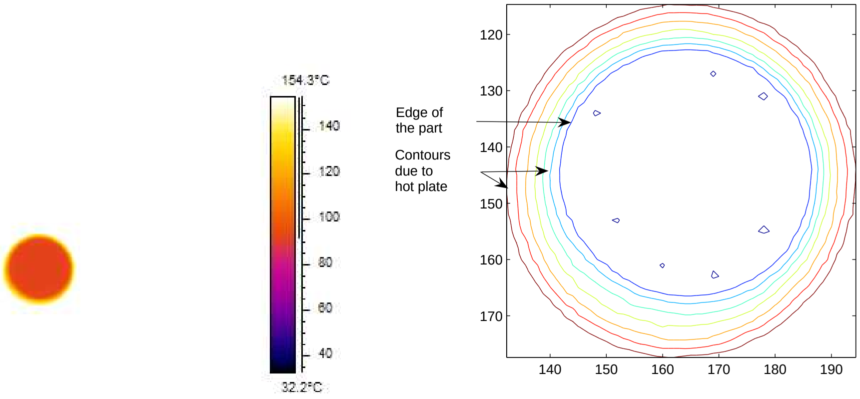

(a) (b)

Figure 6.16: (a) Thermal image captured from the top of the part shown in Figure 6.14 with small fines, and (b) contour plot of the same part.

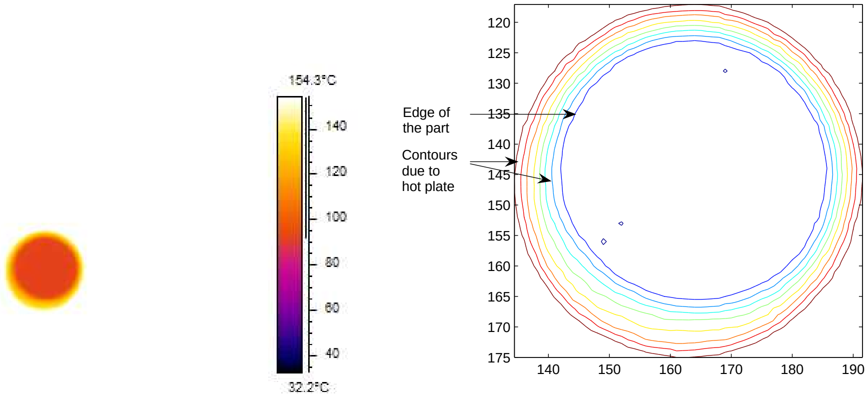

(a) (b)

Figure 6.17: (a) Thermal image captured from the top of the part shown in Figure 6.14 with large fines, and (b) contour plot of the same part.

From the extensive testing performed on 50 parts it became clear that several details are observable with this technique. Fines were easily highlighted from the contour plots which and the rate of rise of the temperature encodes the thermo-physical properties of the material. The results of our testing were consistent with the description where we see fines in the parts within the correct batches.

Although we were able to see several important details in the sample,s our test apparatus requires modifications to be custom tailored for this application. Among the improvements would include a different set of lenses to increase the resolution. Moreover, the heat deposition can be modified to be more suitable for this application and processing can include a step where the contours are free of the additional circles caused by the temperature of the hot-plate which is observable from the top.

6.2.7 Pulsed inductive heating arrangement

The preliminary thermal measurements on complex gears show that the heat source is of extreme importance. We have concluded that the DC current is not appropriate unless multiple probes are used to maintain uniform current density throughout the volume of the part including its surface. Furthermore, this requirement adds complexity to the instrument thereby limiting the versatility of the technique. To remedy this limitation we devised a system that relies on induction heating to generate the thermal gradient that is later recorded through the IR camera. The method takes advantage of the skin depth which is a measure of the thickness where electrical conduction takes place in a conductor. This is caused by electromagnetic induction within the conductor which opposes current flow. Equation (6.1) describes the skin depth

$$\delta = \frac{1}{\sqrt{\pi f \mu \sigma}} \tag{6.1}$$

where δ is the skin depth in m, f is the frequency in Hz, μ the permeability of the material, and σ the conductivity of the material in S/m. Testing was performed at a frequency of 50 KHz for two part types with conductivities of $\sim 10^3\, S/m$ and $\sim 10^6\, S/m$ respectively. The predicted skin depth for these parts at the nominal frequency of 50 KHz was $70\, mm$ and $2.25\, mm$.

The improved inspection approach utilizes an AC current excitation where we control the depth of electromagnetic penetration into the part by controlling the frequency of the source. Figures 6.18 and 6.19 depict the test arrangement; it utilizes an induction-heating unit consisting of a power supply and an induction coil suspended below the compact which renders the technique contact-less. Furthermore, a timing and synchronization unit is utilized to provide the control and sequencing of the power supply with the imaging system and data storage. For example, for the part represented by the thermal behavior shown in Figure 5.12 the timing unit may trigger the imager to take an IR image exactly after $5\, sec$ from the time the power supply was enabled to maximize the likelihood of detecting the defects.

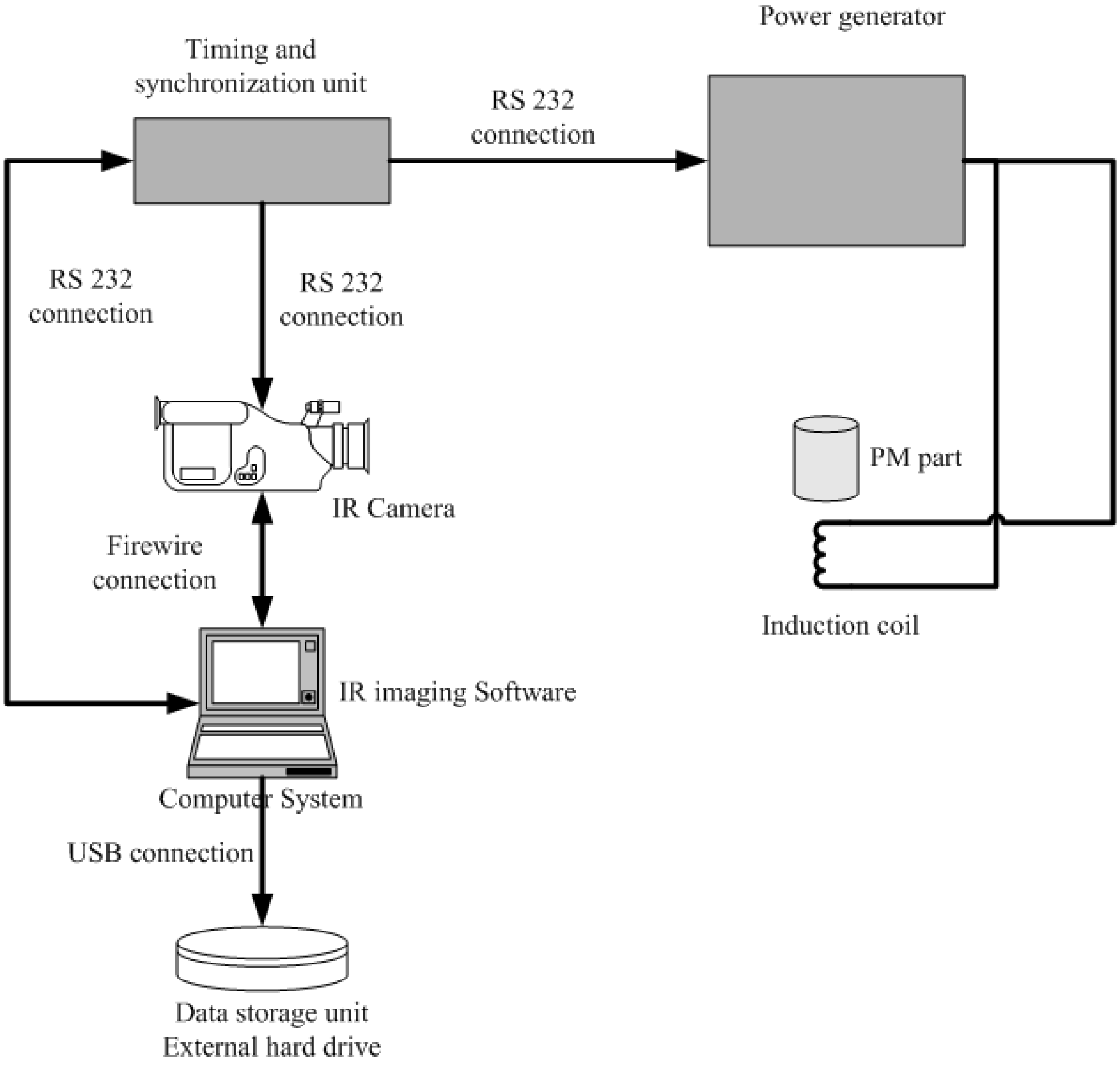

Figure 6.18: Test arrangement for the pulsed induction system.

Figure 6.19: Picture of the pulsed induction system.

6.2.8 Pulsed inductive heating measurements

Figures 6.20 and 6.21 depict IR images for 2D surface and line profiles (along the dotted line). The data is collected with an IR camera positioned 50 cm away (viewed from the side) and operated at a frame rate of 30 Hz. The field of view of the 240 by 320 pixel picture is 15 cm by 15 cm. The total line length of 10 cm is subdivided into 180 points (i.e. with a point-to-point resolution of 0.5 mm) whereas the thermal pixel intensity is displayed in discrete increments up to a maximum discrete level of 260 (or 460K).

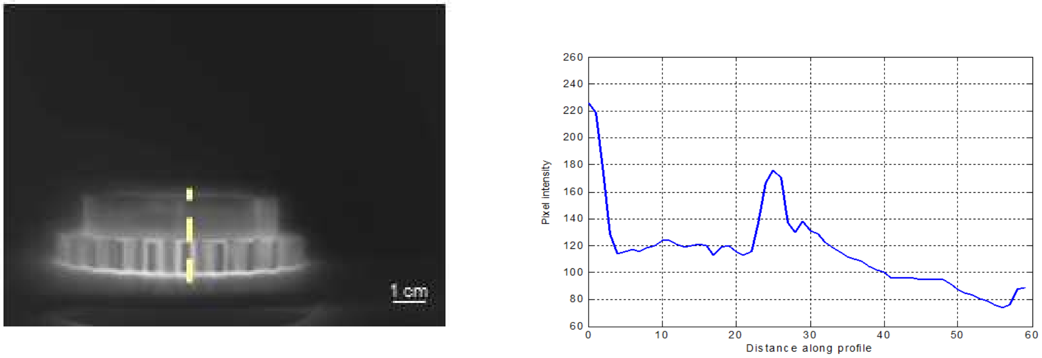

(a) (b)

Figure 6.20: (a) Initial image from the IR recording of the gear part shown in Figure 6.12 and subjected to an AC current, (b) thermal profile along the dotted line.

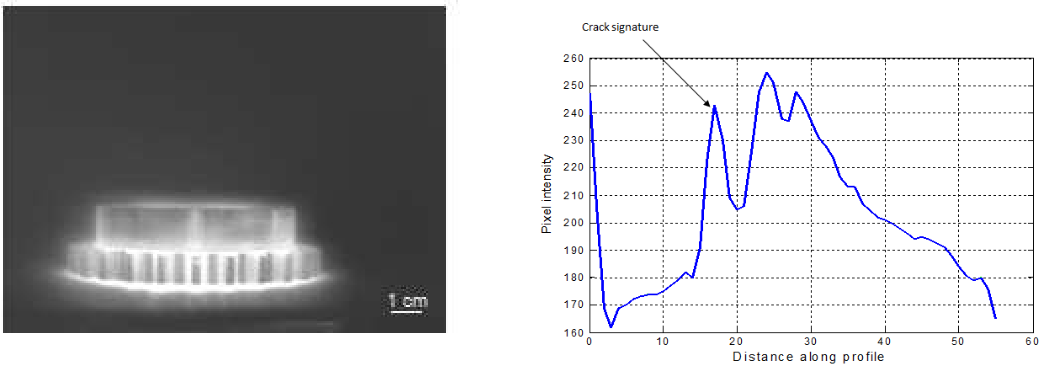

(a) (b)

Figure 6.21: (a) Image after 15 sec from the IR recording of the defective gear part shown in Figure 6.12 (a), (b) thermal profile along the dotted line.

Another component of our testing system involves signal processing. We apply several mathematical tools to extract defect information from the image. Specifically, we analyze the derivative of the thermal profiles of several pre-selected spots on the surface of the compact. Later, we extended this method to include a so-called Laplacian operator to search for surface cracks.

6.3 On-line testing

Tests at various manufacturing facilities allowed us to establish the stability of our inspection system and its immunity from temperature fluctuations in the plant arising from production equipment such as presses, motors, and sinter furnaces. It became necessary to validate the IR system for the detection of real and commonly observed defects in the process line. Furthermore, our plan to extend the usability of this method to detect defects regardless of material composition requires careful analysis. Aluminum powder presents a unique challenge: it is a highly reflective material with very low emissivity (0.1 to 0.2) when compared to steel parts with high graphite content where the emissivity is on the order of 0.6.

Initial evaluations were conducted at the Portland facility of Nichols, Portland, ME. Here more complex parts (gears) shown in Figure 6.22 were observed at different production lines and from different viewing angles. The press rate of 900 parts/h resulted in an approximate speed of 0.2 m/s over the attached conveyor belt.

Figure 6.22: Green state P/M compact (part courtesy of Nichols, Portland, ME).

The following IR images in Figures 6.23, 6.24, and 6.25 represent 2D surface and line profiles (recorded along the dotted line) of parts that are expected to be defect-free. The images are recorded with an IR camera positioned 50 cm away (viewed from the side) and operated at a frame rate of 30 Hz. The field of view of the 240 by 320 pixel viewing is 15 cm by 15 cm. The total line length of 10 cm is subdivided into 180 points (i.e. with a point-to-point resolution of 0.5 mm) whereas the thermal pixel intensity is displayed in discrete increments from a baseline of 0 (or 200K) to 260 (or 460K).

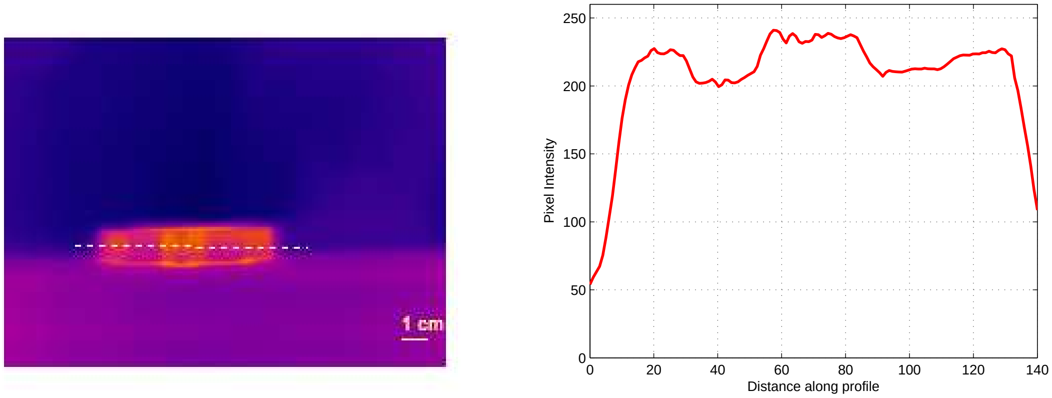

(a) (b)

Figure 6.23: (a) First image from the on-line IR recording of the gear part shown in Figure 6.22 at a speed of 0.2m/s, and (b) thermal profile along the dotted line.

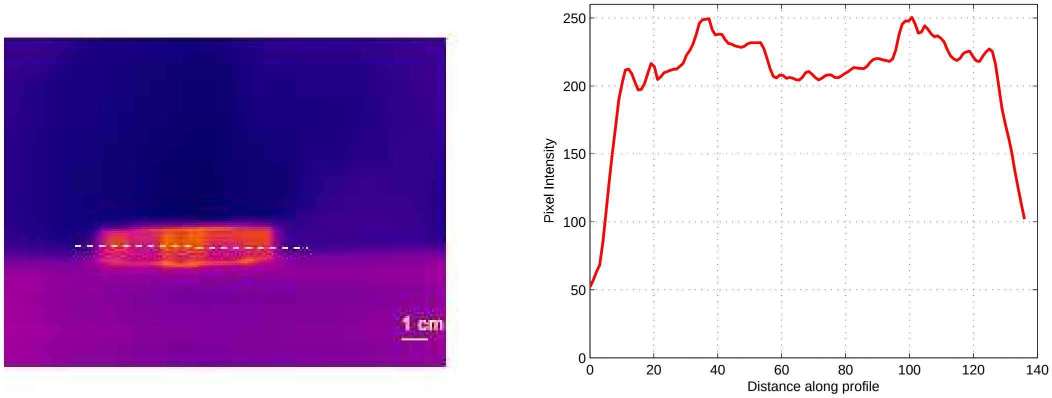

(a) (b)

Figure 6.24: (a) Image from the on-line IR recording of the gear similar to the part shown in Figure 6.22 at a speed of 0.2m/s, and (b) thermal profile along the dotted line.

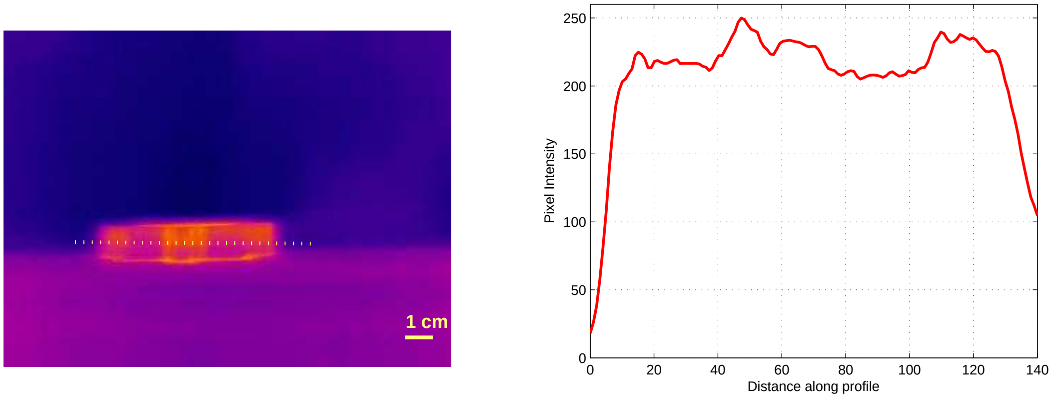

(a) (b)

Figure 6.25: (a) Image from the on-line IR recording of the gear part shown in Figure 6.22 at a speed of 0.2m/s, and (b) thermal profile along the dotted line.

A more extensive on-line testing protocol allows us to conduct a statistical study over hundreds, even thousands of samples. This determines the repeatability of the testing methodology and provides qualitative information about the stability of the background. A long IR image sequence of more than one minute (74 seconds) provides 2266 recorded temperature points with an intensity profile presented in Figure 6.26. As expected, whenever a part moves past the fixed spatial location, the temperature increases.

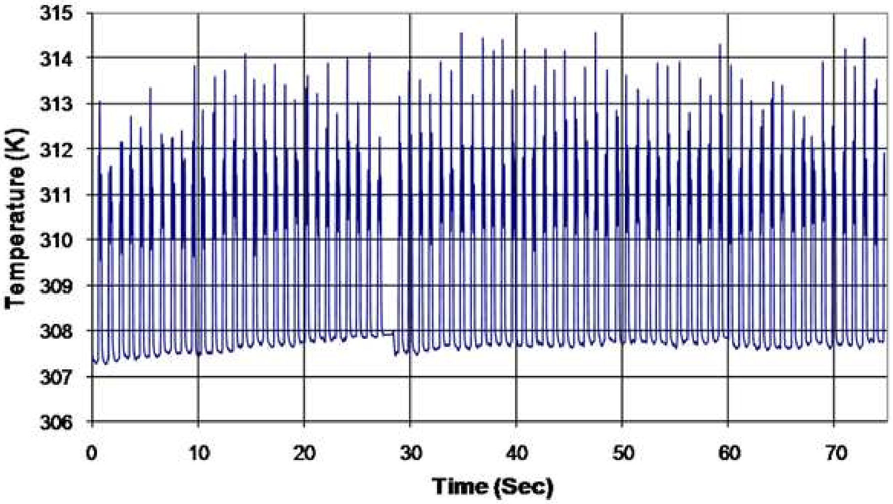

Figure 6.26: : Temperature (in K) recorded at a fixed spatial location (one spot) over time.

A qualitative analysis of the data sequence reported in Figure 6.26 is shown in Figure 6.27. Here every temperature "spike" is equivalent to a gear tooth.

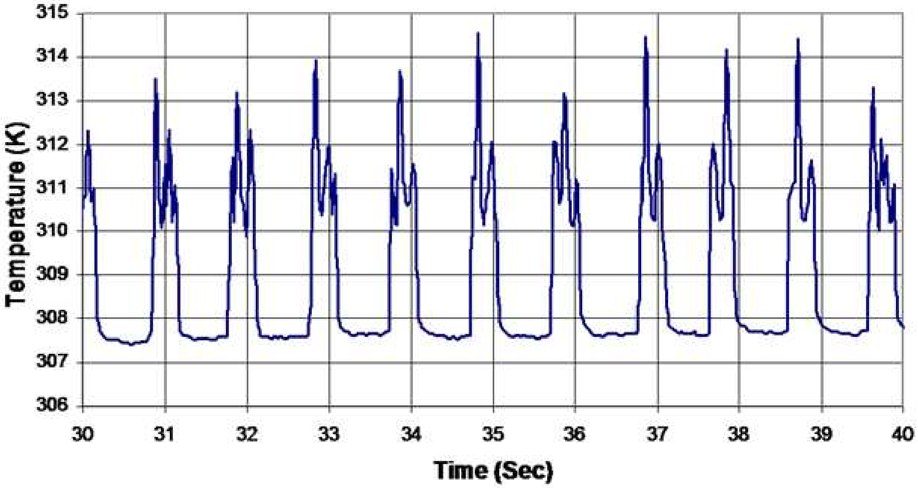

Figure 6.27: : Zoomed-in temperature (K) recorded at a fixed spot location.

Recording data from a different viewing angle is easily conducted such that it covers more surface area and captures regions of interest to the manufacturer. The following images represent 2D surface and line profiles (recorded along the dotted line) captured with an IR camera positioned 50cm away (and viewed from the top) with similar settings as the recordings presented above. This testing resulted in the data listed in Figures 6.28, 6.29, and 6.30

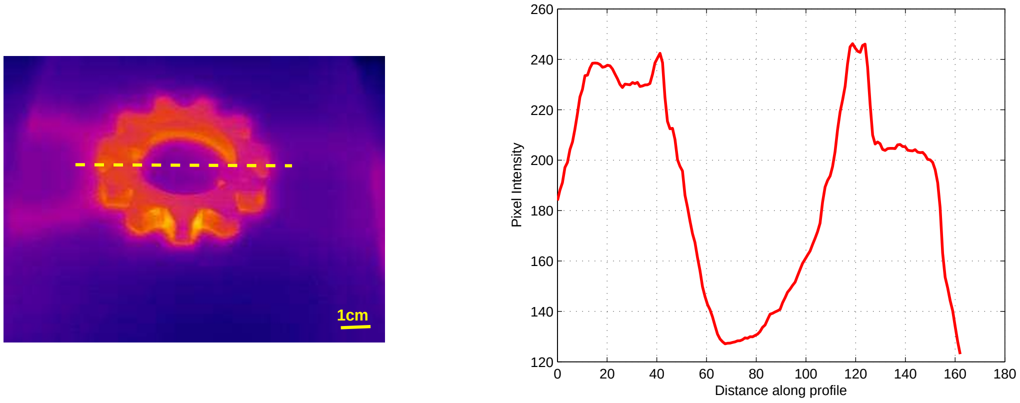

(a) (b)

Figure 6.28: (a) First image from the on-line IR recording of the gear part shown in Figure 6.22 at a speed of 0.2 m/s, and (b) thermal profile along the dotted line.

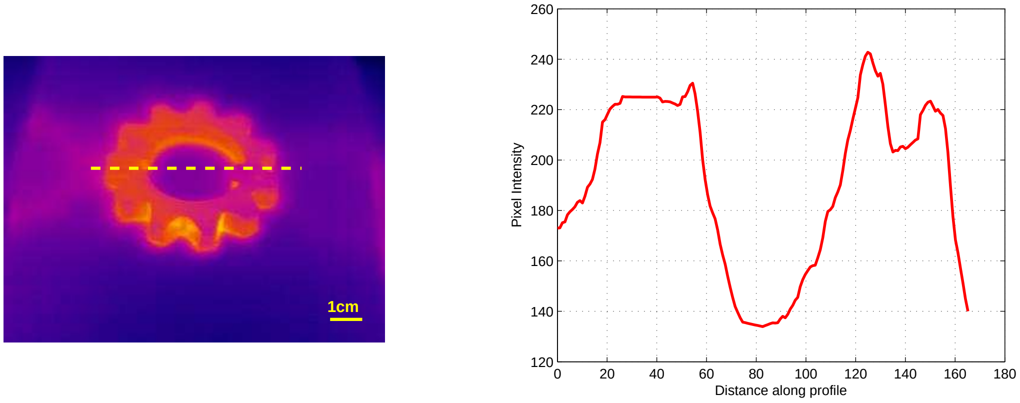

(a) (b)

Figure 6.29: (a) Image from the on-line IR recording of the gear similar to the part shown in Figure 6.22 at a speed of 0.2 m/s, and (b) thermal profile along the dotted line.

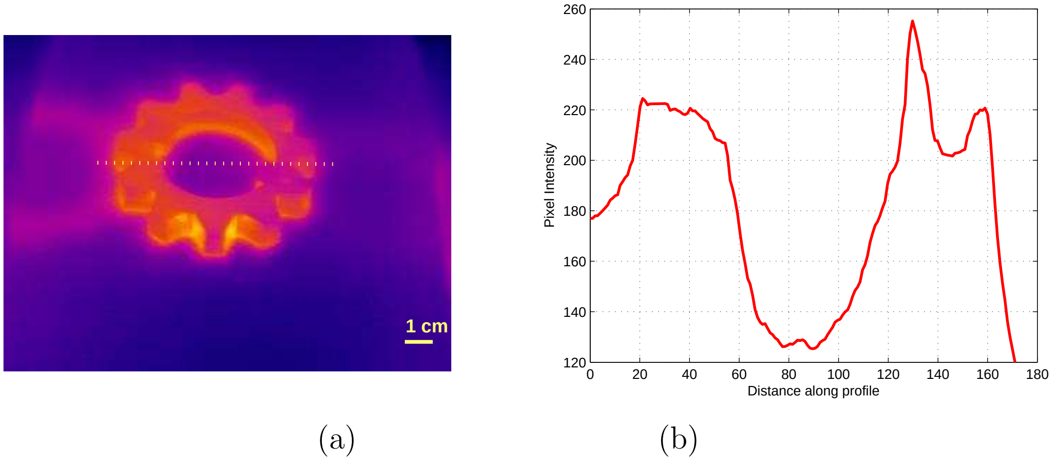

Figure 6.30: (a) Image from the on-line IR recording of the gear part shown in Figure 6.22 at a speed of 0.2 m/s, and (b) thermal profile along the dotted line.

The statistical analysis starts with a long-term data collection shown in Figure 6.31; they present a more detailed view of the thermal profile over time.

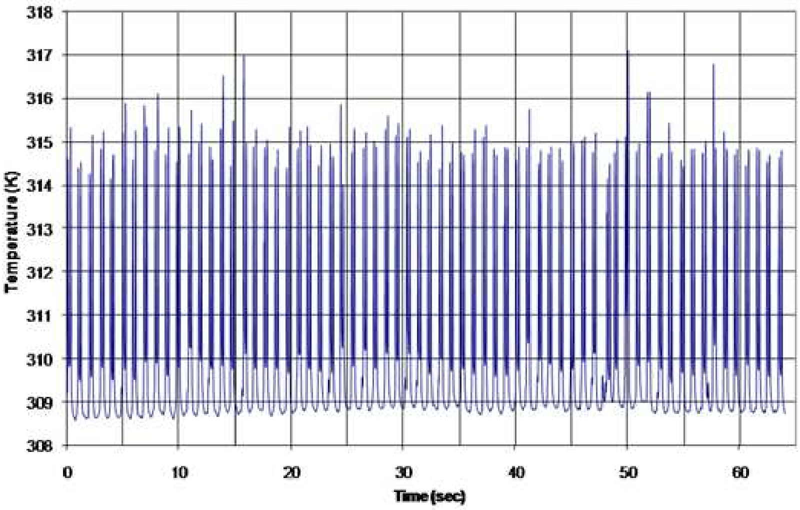

Figure 6.31: : Temperature (in K) recorded at a fixed spatial location (one spot) as a function of time.

while closer look at the data shown in Figure 6.32 revealed that there is an area that may contain defects, this suggested that more analysis is required to verify the claim of a possibility for a crack in the area.

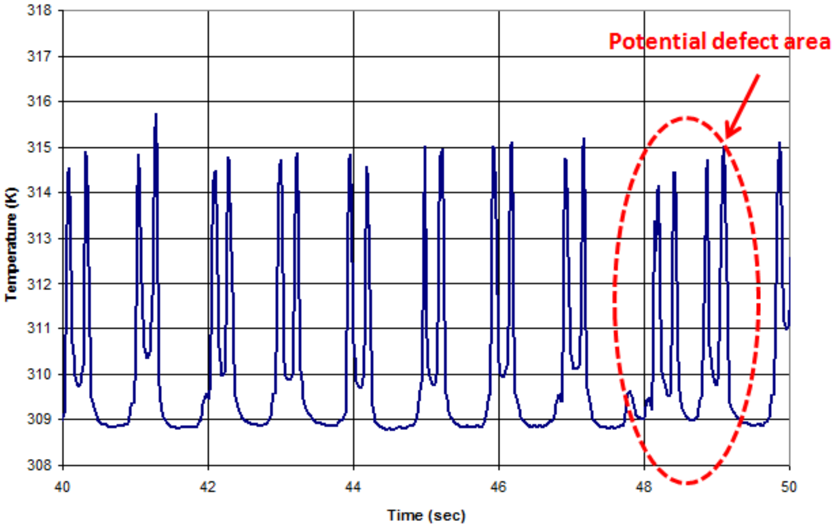

Figure 6.32: Temperature (in K) recorded at a fixed spatial location (one spot) over time.

To accomplish this task of verifying the findings we apply several mathematical tools to extract defect information from the image. Specifically, we analyze the derivative of the thermal profiles of several pre-selected spots on the surface of the compact. Later, we extended this method to include a so-called Laplacian operator to search for surface cracks. It is clear that to capture discontinuities or fast thermal transitions one can compute the derivative of the curve as shown in Figure 6.33

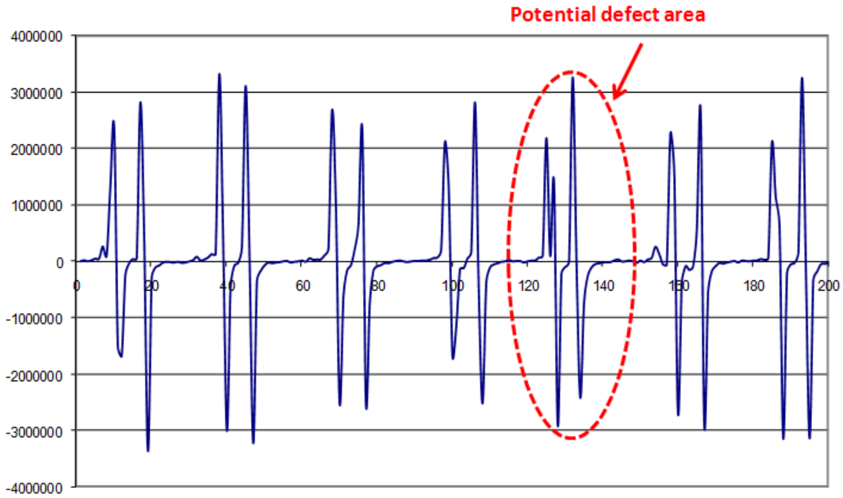

Figure 6.33: First derivative of the temperature recorded at a fixed spatial location (one spot) over time.

The profile obtained from performing the computation of the first derivative shows a distinct pattern that can be attributed to a defect. In practice however, it is difficult to automatically detect the defect unless complex pattern recognition algorithms are employed. A simplified approach is devised where the second derivative is computed which result in a more distinct signatures for discontinuities. Then a simple thresholding and subtraction can be performed to automatically flag a defect. Figure 6.34 shows the second derivative of the spot temperature recording highlighted in Figure 6.32.

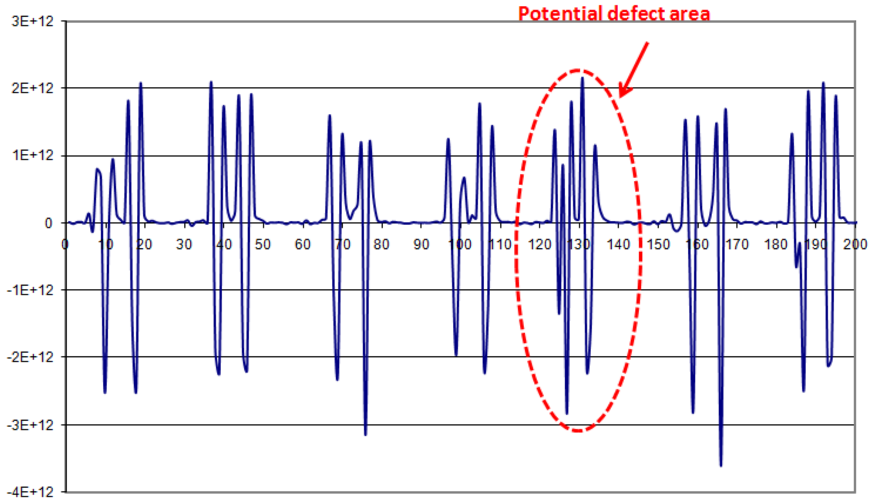

Figure 6.34: Second derivative applied to the temperature recorded at a fixed spatial location (one spot) over time.

Additional testing was conducted at a second manufacturer's facility; at Metal Powder Products (MPP), Corp. in Saint Mary's, PA. At MPP parts of different compositions were tested, then changes to the process were introduced to cause defects. Figure 6.35 shows a standard green-state steel P/M sample. The compact is a two level gear with 13 mm in height by 60 mm in diameter and are typically manufactured at a rate of approximately 600 parts per hour.

Figure 6.35: Green state P/M compact (part courtesy of MPP Corp., Saint Mary's, PA).

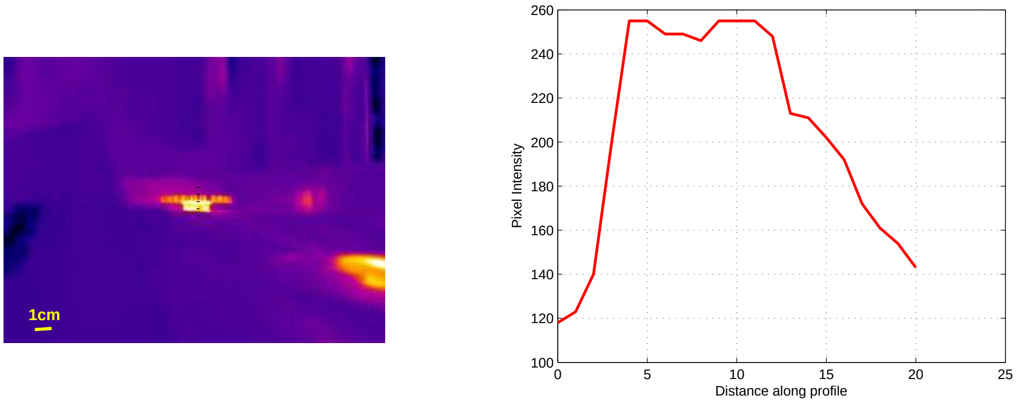

(a) (b)

Figure 6.36: (a) First image from the IR recording of the gear shown in Figure 6.35 at a speed of 0.13m/s, and (b) thermal profile along the dotted line.

A long IR image sequence of 45 seconds generates 1350 recorded temperature points with an intensity profile depicted in Figure 6.38. As expected, as soon as a compact moves past the fixed spatial sensing location, the temperature increases. Then, process monitoring was established by tracking temperature at a single point in space. Figure 6.37 shows the location of the temperature tracking point.

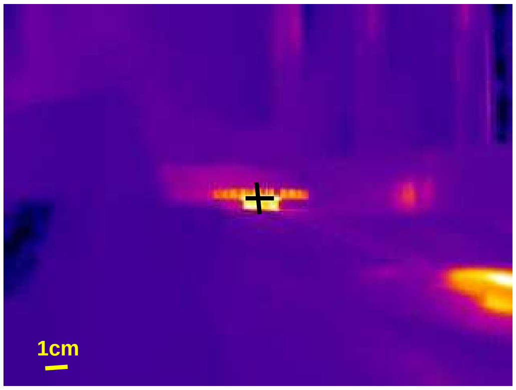

Figure 6.37: : Temperature monitored at the point shown.

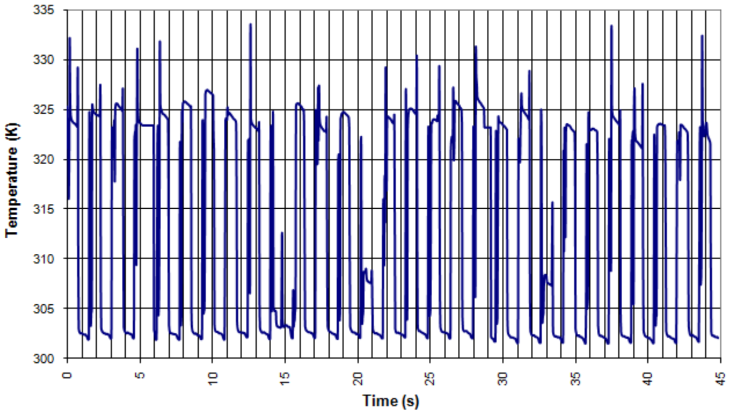

Figure 6.38: : Temperature (in K) recorded at a fixed spatial location (one spot) shown in Figure 6.37 over time.

Zooming into the data sequence reported in Figure 6.38 allows us to conduct a more detailed analysis, as depicted in Figure 6.39.

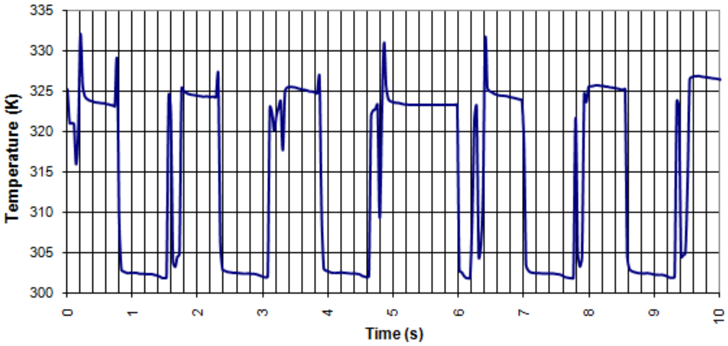

Figure 6.39: Zoomed-in temperature (K) recorded at the fixed spot location shown in Figure 6.37.

Apart from some small variations, the temperature profiles are remarkably reproducible. This is consistent with the fact that the parts are defect-free, an observation that was verified off-line. Therefore, we attribute the thermal fluctuations to instabilities in the process.

The IR images in Figure 6.40 are taken at the same line as shown in the image of Figure 6.36. However, during the first 20 sec we see defective parts and later, after the process adjustment, the response of defect-free parts. Figure 6.40 shows an IR image of a defective gear and the associated profile along the dotted line.

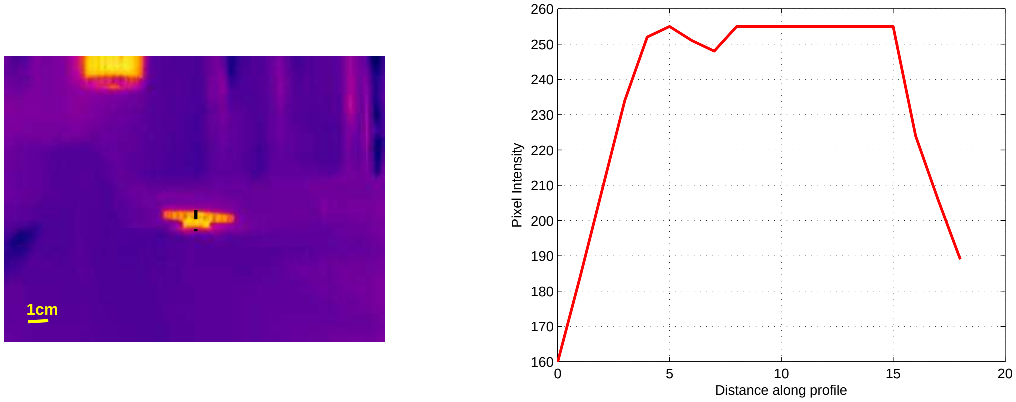

(a) (b)

Figure 6.40: (a) Image from the IR recording of the gear shown in Figure 6.35, at a speed of 0.13m/s, and (b) thermal profile along the dotted line.

It is apparent that the profile shown in Figure 6.40(b) differs from the profile shown in Figure 6.36(b); this is a key indication for the presence of a defect. For identifying significant defects similar to what is presented, a simple image subtraction would be sufficient to flag defective compacts. The statistical analysis that shows an entire 45 sec inspection duration, or 1350 frames, is shown in Figure 6.41. Defects were introduced by changing press settings during press operation. Figure 6.41 depicts the points were the process was modified.

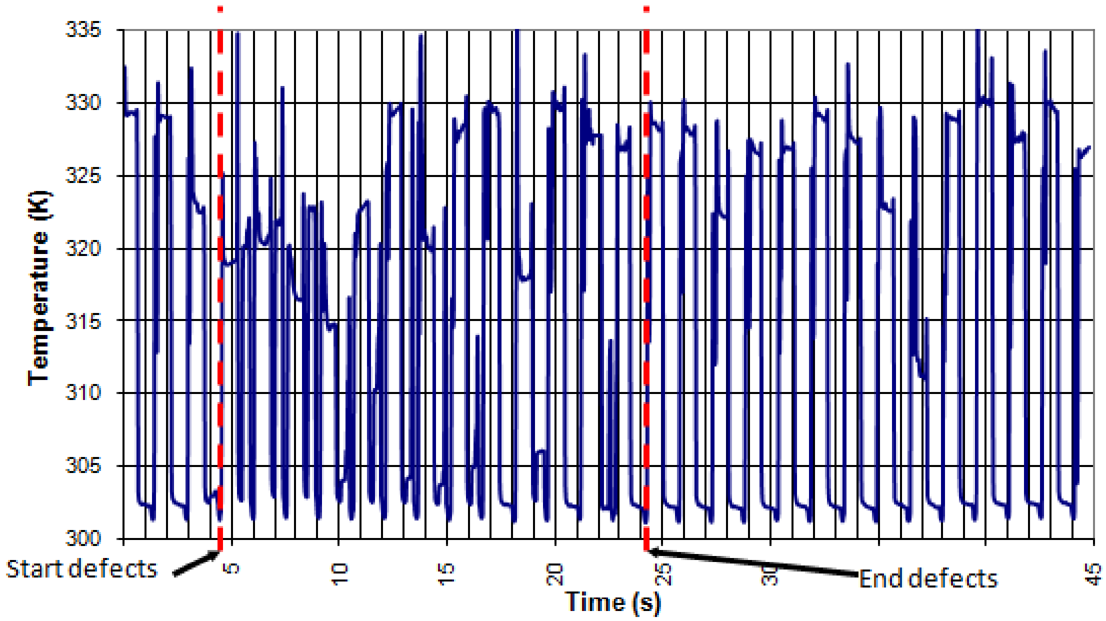

Figure 6.41: Temperature (in K) recorded at a fixed spatial location (one spot) as a function of time.

A detailed investigation of the data sequence reported in Figure 6.41 allows us to conduct a more thorough analysis, as depicted in Figure 6.42.

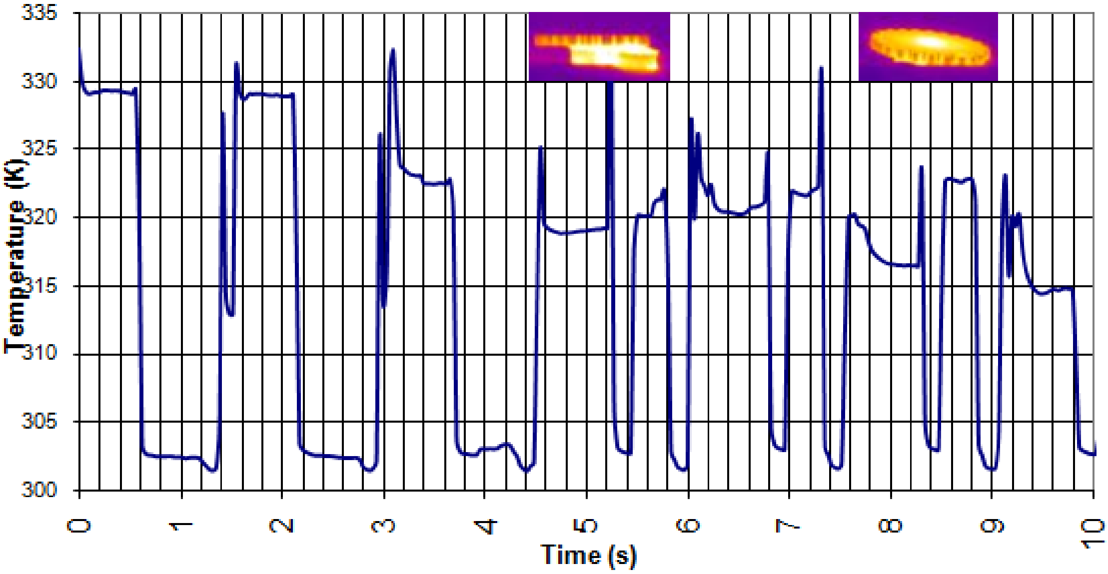

Figure 6.42: Zoomed-in temperature (in K) recorded at a fixed spot location.

Additional tests that involve aluminum parts are discussed below. Figure 6.43 depicts the green-state aluminum powder part. The compact is 20mm in height by 50mm in length and 15mm in width, and compacted at a high density (part parameters and material composition are proprietary to the manufacturer); it is manufactured at a rate of approximately 900 parts per hour. Aluminum compacts provide unique challenges due to high emissivity and high cooling rate. They consequently require special attention with regard to viewing angles and monitoring must be conducted at a close proximity to the press. It is also important to ensure temperature equilibrium during the testing phase.

Figure 6.43: Aluminum powder green-state compact (courtesy of MPP Corp., Saint Mary's, PA).

Due to access restrictions we were unable to image the green-state compacts directly as they exited the press. This unfortunately precluded our ability to inspect the parts while they are at a high temperature setting. For the testing, we use the same procedure as discussed above: a fixed sensing point is selected in the process line as shown in Figure 6.44. We can then monitor its temperature behavior over time.

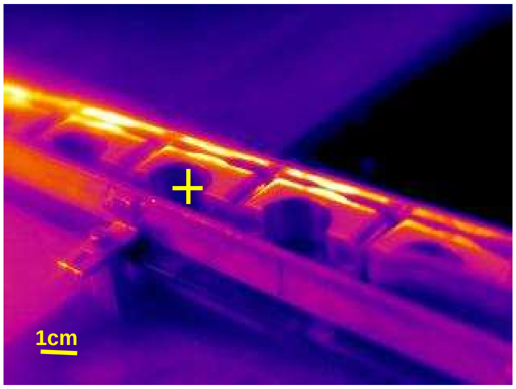

Figure 6.44: Identifying a point (cross) in the process line for thermal recording.

As discussed before, we can now examine defect-free and defective parts with artificially induced hairline cracks across the curved section of the compact. First, we report the statistical data for the defect-free parts in Figure 6.45.

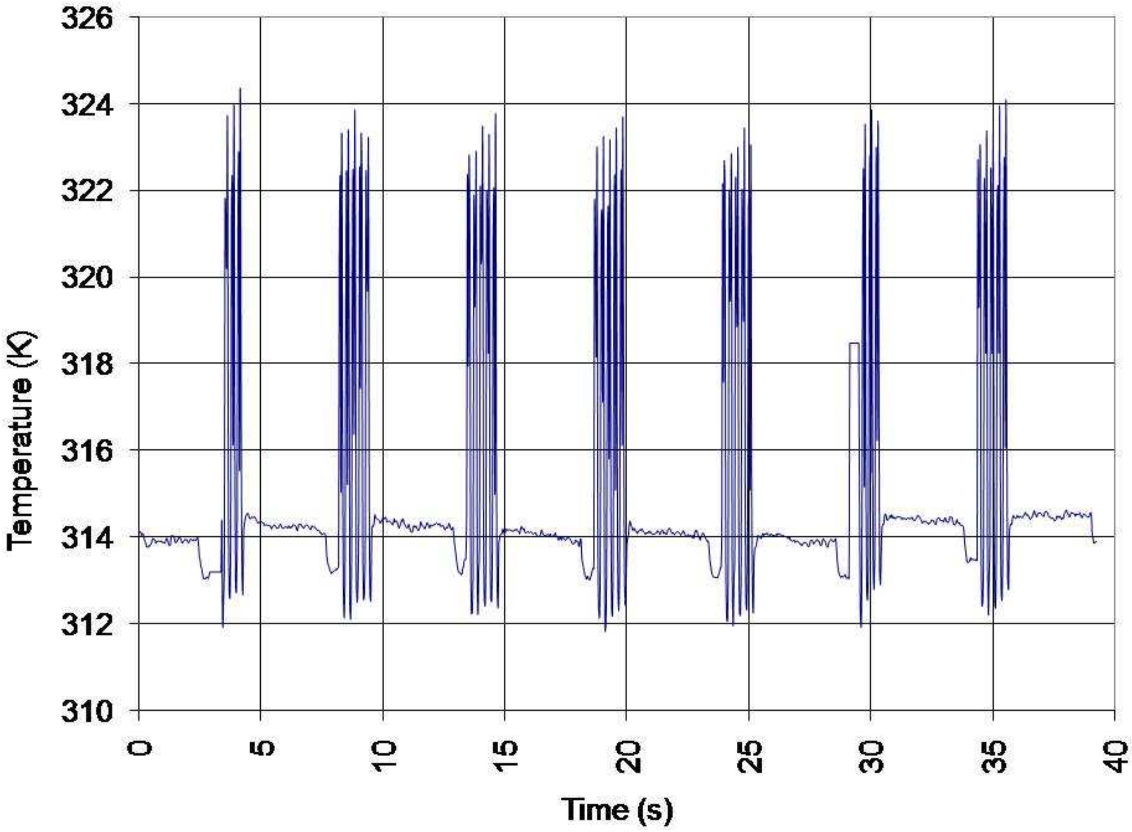

Figure 6.45: Temperature (in K) recorded at a fixed spatial location (one spot) over time.

Besides fabrication immunity, the IR testing methodology appears sufficiently robust to handle different material compositions. In particular, we were able to test aluminum parts that have the special characteristics of high reflectivity and high cooling rate.

Thus far, all of our signal processing and data analysis is performed off-line. For a fully manufacturing-compliant system it is important to combine these steps into a rapid data collection and processing environment to provide real-time feedback.

6.4 Software development

In addition to the remote electromagnetic power deposition scheme, we have developed a custom software package that directly interfaces with the IR camera system. It is application-specific in the sense that the thermal data can be used to provide the user with feedback relative to the integrity of the samples under test. Furthermore, valuable information regarding process stability can be obtained by monitoring the speed of the compaction press. To extend the usability of the IR detection instrument to enable quality control, we have constructed two basic software modules:

- A real-time IR imaging system with a simple and friendly graphical user interface (GUI) that can be used by the press operators and quality engineers (it is intended to be deployed in the manufacturing line with pass/ fail feedback).
- A comprehensive data visualization and analysis system for a more in-depth failure analysis.

Functionally our software package offers a number of unique features; they include in particular

- Full control of the camera system (on/off, zoom, focus, recording for local or remote storage) as well as functions common to computer vision systems,
- Real time data collection and processing,
- Image display (real time IR scene and processed image), and
- Automatic defect detection

The diagram depicted in Figure 6.46 details the steps taken to perform the on-line IR testing. Two major functions are completed here. First, the defect detection is conducted by comparing a sequence of images to a reference frame or image to permit efficient, automatic detection. Second, a simple speed measurement will provide the press operators with feedback on the compaction process stability. To maximize efficiency, the user can set the desired frame rate by either reducing the amount of data to be processed and stored, or by increasing the amount of data processing and storage for detailed analysis. The default setting for the test system is not to record data unless prompted by the user, or if a defect is flagged.

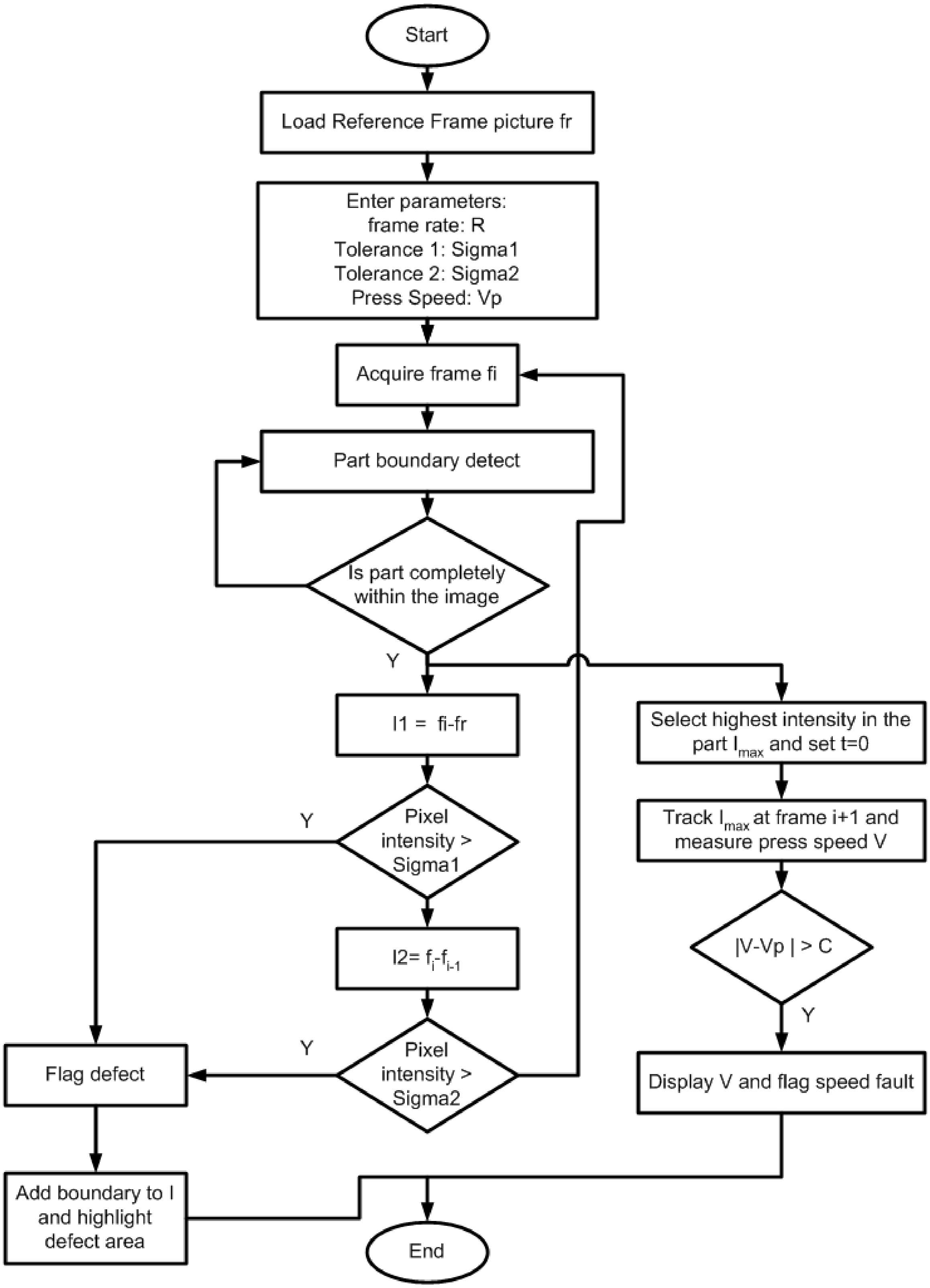

Figure 6.46: Software block diagram.

Figure 6.48 shows the user interface that targets a detailed data analysis which enables the quality engineer to gain full access to the thermal data; it provides basic analysis tools including spot temperature recording, averaging, and alarms. In addition to this comprehensive GUI, the software package has a built-in interface for the press operators and technicians on the manufacturing floor. This interface is limited to alarms and basic display of thermographic images.

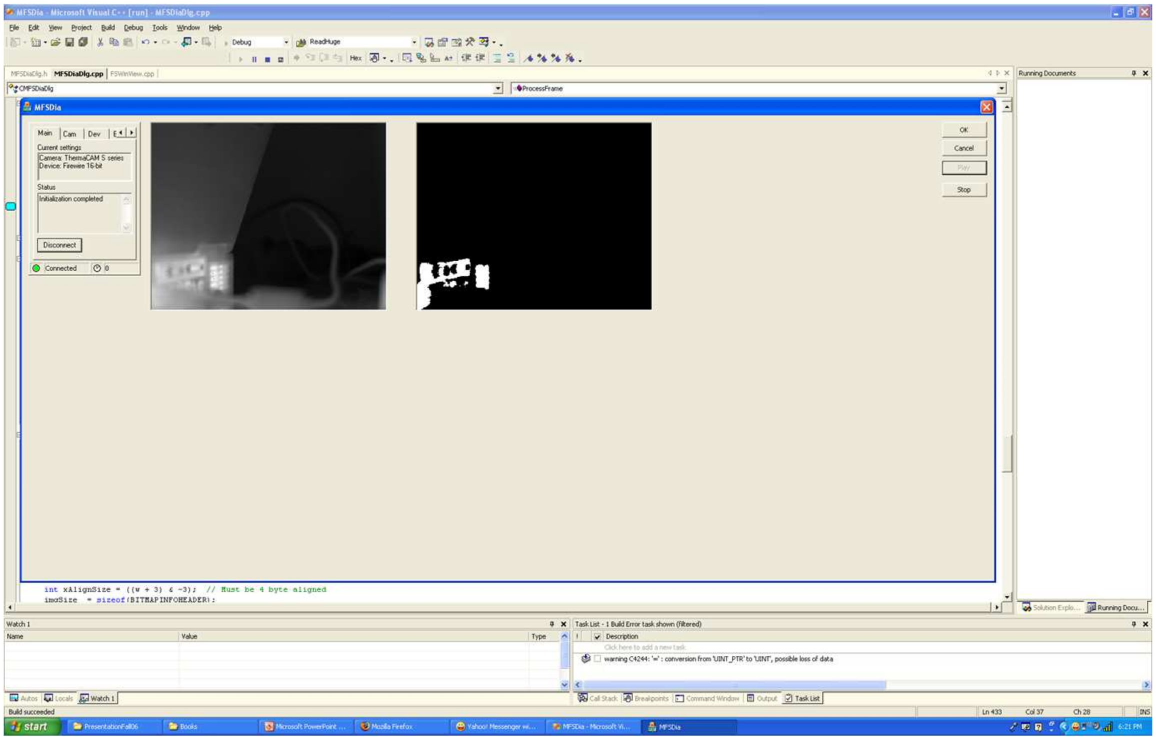

Current settings
Camera: ThermaCAM S series
Device: Firewire 16-bit

Status
Initialization completed

● Connected 0

```
int xAlignSize = ((w + 3) & ~3);  // Must be 4 byte aligned
imgSize  = sizeof(BITMAPINFOHEADER);
```

Task List - 1 Build Error task shown (filtered)

☑ Description

Click here to add a new task

☐ warning C4244: '=' : conversion from 'UINT_PTR' to 'UINT', possible loss of data

Build succeeded

Ln 433 Col 37 Ch 28 INS

Figure 6.47: Snap shot of the simple user interface window.

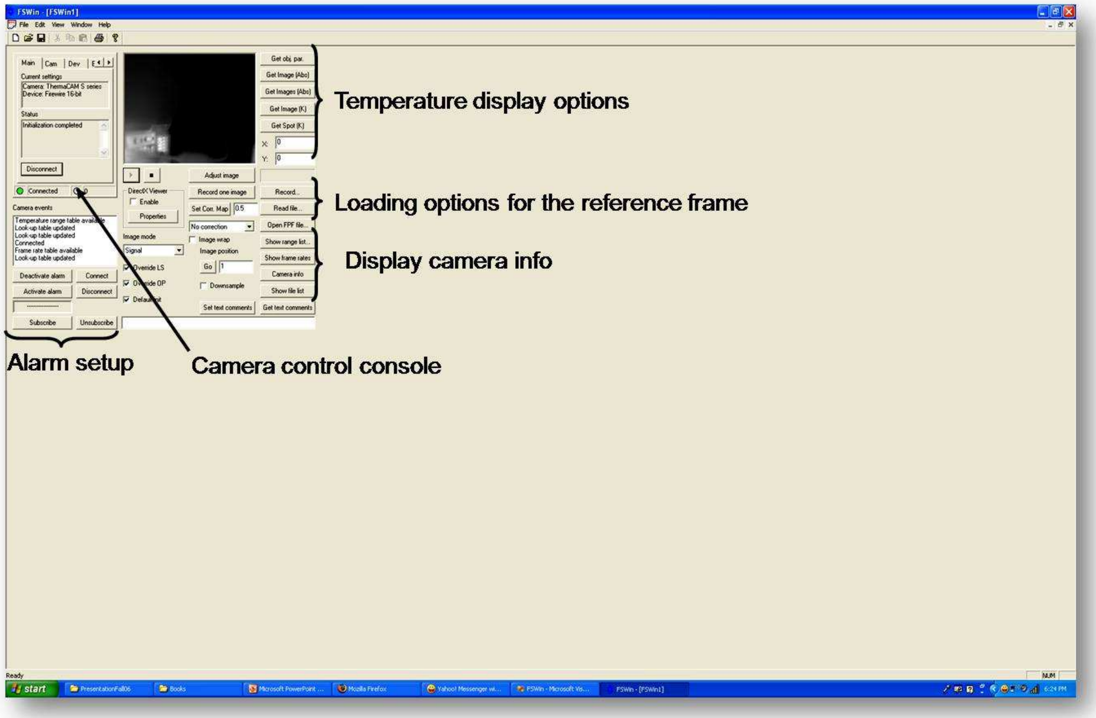

FSWin - [FSWin1]

Current settings
Camera: ThermaCAM S series
Device: Firewire 16-bit

Status
Initialization completed

Connected

Camera events
Temperature range table available
Look-up table updated
Look-up table updated
Connected
Frame rate table available
Look-up table updated

Image mode: Signal
☑ Override LS
☑ Override OP
☑ Default init
☐ Enable
Set Corr. Map: 0.5
No correction
☐ Image wrap
Image position: 1
☐ Downsample
X: 0
Y: 0

Figure 6.48: Snap shot of the user interface window.

The off-line testing topology incorporates an automatic defect detection technique based on a "region-growing algorithm". This method results not only in defect detection, but also in displaying two dimensional spatial characteristics of the defect. Although not included in this current setup, one can infer defect depth information from the contrast setting, as the two terms are inversely proportional. The region-growing algorithm is summarized as follow [25, 26, 27]:

1. Compute the mean and standard deviation of the pixel intensities to reduce the amount of data processing.

2. Detect the pixels with the highest contrasts ("hottest") in every region: they constitute seeds.

3. Start the defect shape extraction by growing a region around the seed.

4. Each seed is processed individually and assigned its own threshold.
5. Neighbors are computed using a recursive procedure and assuming an eight connectivity (i.e. all pixels surrounding the seeds).
6. Stop the region growing once the background pixels or border pixels are met.

This algorithm was implemented and complex gears with corner defects were tested. Figure 6.49 presents the results of our test; the software was able to detect the defect in real time.

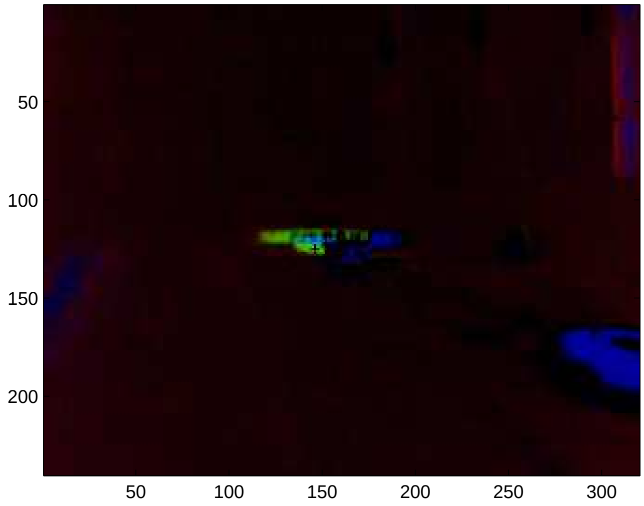

Figure 6.49: Real time defect detection.

We have been able to reliably detect defective part in the manufacturing line described above. These defects were introduced through modifying press parameters which limits our ability to control the size and the shape of the cracks and there is only limited prediction of the location.

The experimental study was extensive in scope as hundreds of parts were tested and multiple test setups were constructed to accomplish the various methods described. On-line testing however, was limited to defect free parts due to the limited access to production lines and when available, it is not practical to introduce known defects onto the parts.

In this chapter, many test beds were introduced and the merits and drawbacks of each were listed. It is apparent that infrared imaging is applicable to defect detection in green-state P/M compacts. The only modifications required are related to the energy deposition scheme which varies depending on the material parameters and the type of defects (surface, subsurface, corner, etc.) the user is interested in detecting.

Chapter 7

Conclusions

Key objective of this dissertation is to describe an approach suitable for the high reliability testing of P/M compacts early in the manufacturing process. Specifically, our research focused on the evaluation of green-state P/M compacts both online and offline. The online approach combines a passive thermography measurement with an image processing technique that allows for a rapid pass/fail feedback. This approach was extended to provide information related to process parameters including press speed which has been proven useful to manufacturers. The offline test system is based on an active thermography scheme to detect minute surface cracks and subsurface defects. This involves contactless energy deposition where current is injected inductively and powerful analysis software is synchronized to the current source to yield fast and comprehensive evaluation data.

A mathematical model was developed as a testbed to establish the fundamental design parameters of the inspection technique. These parameters are subsequently used to calibrate the numerical model. The theoretical approach involves the solution of Laplace's equation for a canonical part geometry (cylinder) with no defect. Then, the solution was extended to include an internal discontinuity. The solution to this first set of equations is related to the source term in the heat equation. The electro-thermal problem with an embedded source is addressed through the method of images and Green's functions. These initial solutions describe the expected behavior of the P/M compacts when subject to electric current. It became clear that a voltage distribution is established instantly with a relaxation time on the order of pico-seconds. The solution to the heat equation, however, shows that temperature on the surface of the compact increases gradually until it reaches equilibrium. Moreover, internal sources that represent defects display a distinct thermal signature that decays over time. This led us to focus our research and analysis on pulsed heating in an effort to establish minimum requirements for the frame rate of the camera to 1Hz.

A set of numerical models were presented to cover the possible applications of the system and helped estimate the detection limit for each approach. A combined electrostatic and heat transfer model were first verified under steady-state conditions and then the transient behavior was studied. For the steady state analysis, the electrothermal model agrees with analytical solutions where surface cracks are apparent while subsurface defects have no obvious effect on surface temperature. The inclusion of transient effects, where current is applied as a step function, results in a distinguishable effect on the surface. This effect diminishes over time until thermal equilibrium is reached and the effect disappears. Similar to the analytical solution, this model further confirms the minimum camera requirements such that a frame rate of $2Hz$ is largely sufficient in capturing transient effects and based on a thermal resolution of $0.2°C$. The camera system utilized in the subsequent experimental study has a frame rate of 30 frames/ second and a temperature resolution of 0.08C with a spatial resolution of 320 X 240 pixels. In addition to the active system, a passive system that includes initial conditions as the residual heat in the part due to compaction was devised. This complex solution involves an adaptive heat transfer coefficient which takes into account fluid velocity and fluid flow. Typical manufacturing rates were used in the model and results show a maximum response at a time stamp of 1 second from the initial moment when the part exits the compaction press. These results further support the analytical analysis and led to an adequate camera positioning in the manufacturing line at 2 feet from the compaction press system.

The culmination of our work was the software development and the extensive testing performed in the laboratory and on the factory floor. Initially, in a laboratory setting detection limits were evaluated as a function of material constituents, part shape, size, density, and emissivity. Unflawed cylindrical iron-based parts were tested with hairline (20 micron in width) surface cracks with different lengths up to $5mm$ and random orientations, parallel to the current flow and normal to it. Results show that all defects are detectable regardless of orientation; this represents a major advantage of the technique over other test methods. However, DC current excitation leads to major drawbacks due to the need to contact the part. Among the limitations is the effect of contact resistance which as shown in the results may overshadow defects close to the ends of the part. The next step in our experimental study is the evaluation of pulsed heating. First, a generic heat source such as a hot plate was used. The hot plate was synchronized with the camera system to attempt to detect fines in smaller cylindrical parts. Then, an induction heating arrangement was constructed and tested with complex multilevel gears with hairline cracks on the surface of their teeth. These defects occur regularly during manufacturing and are typically hard to detect.

Testing controlled samples in a known environment allowed us to develop our detection algorithm and establish a base calibration for the system. Thereafter, testing was conducted at various manufacturing facilities that specialize in specific materials such as iron or aluminum. Test rates were also evaluated where we evaluated compacts from a throughput of 100 parts per hour to over 1000 parts per hour. All testing confirmed the applicability of the proposed technique with a high degree of success. Test results were positive in a sense that when defects were detected, the method remained insensitive to background noise. Our data analysis was also capable of detecting changes in the speed of the press that was later thought of as the potential source of the defects observed. A custom software package captures this added value to provide the following features:

- Automatic defect detection
- Compaction rate measurement
- Potential to extract the outline of the defect thought the region growing algorithm

In summary, the thesis laid the foundation for a fully manufacturing compliant inspection system. Analytical formulations, numerical modeling, and testing show that thermography is a suitable technique to detect defects in green-state P/M compacts where most other nondestructive testing methods fail.

Further Work

Full manufacturing compliance can be attained by packaging our test apparatus into a stand-alone system that can easily be deployed, accessed, and monitored. However, this requires additional software features and connection ports to be integrated with process controllers and monitoring equipment. This could also involve the integration of multiple cameras into a single system and a software package capable of reconstructing an image from multiple sources simultaneously and include the time factor to develop a three dimensional profile of the part, hence becoming a true online 100% testing scheme. Due to its sensitive laboratory setting, the final apparatus is required to undergo rigorous design of experiments for detection reliability testing on the factory floor. Here we would need to estimate accuracy and repeatability in a manufacturing setting. False positives can lead to lengthy and costly disruption of manufacturing while failure to detect a defect leads to a compromised product.

Another area of improvement involves the integration of the heat source into the manufacturing line. This will require for instance the design of a special induction coil that can efficiently deposit thermal power into the part during the time window when the part is traveling on the conveyor belt between the compaction press and the sintering furnace. For this arrangement to work appropriately we would have to take into account the distance from the coil to the bottom of the part which is largely dependent on the type of conveyor system and the quality of the belt. The inspection task is further complicated by the high rate of compaction that greatly limit the exposure time of the part to the heating power. One idea would involve modifying the manufacturing line to add an evaluation step. This step may include a platform to house the coil such that the part accesses the platform and heat is induced and a measurement is taken within 0.5 seconds. This concept will eliminate the need to control the conveyor system and allow enough time for the part to be tested without significantly impacting the overall throughput.

An active area of research in the P/M industry involves the capture of density distribution as a major quality metric. Currently a crude weight measurement at the exit of the compaction press and an online statistical measurement of volume provide a value for density. In reality, it is more desirable to measure density distribution throughout the compact to evaluate defects and predict future cracks. With this aim in mind, we see the opportunity to map the thermal signal into a density profile. This will require first an analytical analysis of the resolution, since typically manufacturers are interested in minute density variations. Density mapping will require a different image processing scheme to measure subtle intensity gradients instead of the sharp transients observed in defect detection. More features can also be built-in to capture density variability from part-to-part. Because of the very small variations, the system needs to be appropriately constructed with fine control of power deposition and elaborate image processing algorithms.

Real time density measurements may provide a key control parameter in the manufacturing cycle such that compaction pressure can be modified to achieve a specific density profile. In this manner, repeatability is guaranteed and the potential for future cracking of the green state compacts is reduced.

Bibliography

[1] German, R.M. “Powder Metallurgy Science” Metal Powder Industries Federation, Princeton, New Jersey, 1984.

[2] “Cost-efficient, Net-shape Manufacturing with Powder Metals...a Primer” GKN Sinter Metals P/M University 2003.

[3] Clark, F. “Advanced Techniques in Powder Metallurgy” Rowmann and Littlefield Inc. New York, NY 1963.

[4] Leuenberger, G. “Electrostatic Density Measurement in Green-State P/M Parts” PhD thesis, ECE Department, Worcester Polytechnic Institute 2003.

[5] Leuenberger, G. Ludwig, R. “Electrostatic Density Measurement in Green-State P/M parts” Final Report, Morris Boorky Powder Metallurgy Research Center, Consortium Meeting, April 9-10,2003, Metal Processing Institute, Worcester Polytechnic Institute.

[6] Bogdanov, G. “Theoretical Basis and practical implementation of Electrical Impedance Material Inspection of powder Metallurgy Compacts” Master Thesis, ECE Department, Worcester Polytechnic Institute, 2000.

[7] Leuenberger, G., Ludwig, R., Apelian, D. “Electrostatic Detection of Density Variations in Green-State Powder Metallurgy Compacts” Proceedings of QNDE 2001.

[8] Maldag, X.P.V. “Theory and Practice of Infrared Technology for Nondestructive Testing” John Wiley & Sons Inc. 2001.

[9] Burnay, S. G., Williams, T. L., Jones C. H. “Applications of Thermal Imaging “ 10.P Publishing 1988.

[10] Ringermacher, H.I., Howard, D.R. and Gilmore, R.S., "Discriminating Porosity in Composites Using Thermal Depth Imaging" CP 615, Review of Quantitative Nondestructive Evaluation, Vol. 21, ed. by Thompson and D.E Chimenti. American Institute of Physics. 2002

[11] Sun, I.G "Analysis of Quantitative Measurements of Defects by Pulsed Thermography Imaging" CP 615, Review of Quantitative Nondestructive Evaluation, Vol. 21, ed. by Thompson and D.E Chimenti. American Institute of Physics. 2002.

[12] Mendioroz, A., Epinaniz, A., Salazar, A., Venegas, P., and Saez-Ocariz, I. "Quantitative Study of Buried Heat Sources by Lock-in Vibrothermography: An Approach to Crack Characterization" Journal of Physics D: Applied Physics. IOP Publishing 2009.

[13] Han, X., Favro L.D., and Thomas, R.L., "Recent Developments in Thermosonic Crack Detection" CP 615, Review of Quantitative Nondestructive Evaluation, Vol. 21, ed. by Thompson and D.E Chimenti. American Institute of Physics. 2002.

[14] Renshaw, J., Holland, D. "Full-Field Vibration Measurement for Vibrothermography" Review of Quantitative Nondestructive Evaluation, Vol. 21, ed. by Thompson and D.E Chimenti. American Institute of Physics. 2008.

[15] Siegel, R. and Howell, J. "Thermal Radiation Heat Transfer" Fourth Edition, Taylor & Francis 2002.

[16] Incropera, F.P., DeWitt, D.P. "Fundamentals of Heat and Mass Transfer" 4th edition, John Wiley & Sons, New York 1996.

[17] Fei, M. "Electromagnetic Inspection, Infrared Visualization and Image Processing Techniques for Non Metallic inclusions in Molten Aluminum" Master Thesis, ECE Department, Worcester Polytechnic Institute 2002.

[18] Kraus, J.,D. "Electromagnetics" McGraw-Hill Book Company, Inc. 1953.

[19] Bruhat,G. "Cours De Physique General: ELECTRICITE" Septieme Edition, Masson & C^{ie}. 1959.

[20] Zahn, M. "Electromagnetic Field Theory: A problem solving approach" John Wiley & Sons, Inc. 1979.

[21] Morse, P.M. and Feshbach, H. "Methods of Theoretical Physics" Parts I & II, McGraw-Hill Book Company, Inc. 1953.

[22] Logan, D A "First Course in Finite Elements Method" PWS Publishing Company 1993.

[23] " FEMLAB User's Guide and Introduction" COMSOL Inc. version 2.2. 2001.

[24] Sullivan, J. Jr "Computational Methods For PDEs in Science and Engineering" ME 515 Course Notes. Worcester Polytechnic Institute, Fall 2003.

[25] Mat-Isa, N.A., Mashor, M.Y., and Othman, N.H. "Seeded Region Growing Feature Extraction Algorithm: Its Potential Use in Improving Screening for Cervical Cancer" International Journal of the Computer and Management, Vol. 13#1. 2005

[26] Gao, J., Zhou, M., and Wang, H. " A Threshold and Region Growing Combined Method for Filament Disappearance Area Detection in Solar Images" Conference on Information Sciences and Systems, The John Hopkins University, 2001

[27] Chen, C.H. "Signal Processing and pattern Recognition in Non-destructive Evaluation of Materials" NATO ASI Series, Series F: Computer and Systems Sciences, Vol. 44. Springer-Verlag Berlin Heidelberg 1988.

[28] Gailius, A. and Zukauskas, D. "Determination of Concrete Structural Defects By Infrared Spectrum Analysis" ISSN 1392-1320 Materials Science (Medziagotyra). Vol. 9, No. 1. 2003.Gochenbach, M., S. "Partial Differential Equations: Analytical and Numerical Methods" Society for Industrial and Applied Mathematics, 2002.

[29] Scott, R.J., "Nichols Portland: Parker Hannifin Corp." 2400 Congress Street, Portland, ME 04102.

[30] Traxler, H. "PLANSEE Aktiengesellschaft" A-6600 Reutte/ Tirol, Austria.

[31] Carslaw, H., Jaeger, J. "Conduction of Heat in Solids" Second Edition, Oxford University Press 1959.

[32] Keith, F., Bohn, M.S. "Principals of Heat Transfer" Fifth Edition, PWS Publishing Company 1997.

[33] Arpaci, V.S. "Conduction Heat Transfer" Addison-Wesley Publishing Company 1966.

[34] Sommerfeld, A. "Partial Differential Equations in Physics" Academic Press Inc. 1949.

[35] Lee Dong-Ho "Thermal Analysis of Integrated-Circuit Chips Using Thermographic Imaging Techniques", IEEE Transactions on Instrumentation and Measurement, Vol. 43, No. 6, December 1994.